Extension of the High Load Limit in the Homogenous Charge Compression Ignition Engine

by

Robert J. Scaringe

B.S. Mechanical Engineering
Rensselaer Polytechnic Institute, 2005

M.S. Mechanical Engineering
Massachusetts Institute of Technology, 2007

SUBMITTED TO THE DEPARTMENT OF MECHANICAL ENGINEERING IN PARTIAL FULFILLMENT OF THE REQUIREMENTS FOR THE DEGREE OF

DOCTOR OF PHILOSOPHY

IN MECHANICAL ENGINEERING
AT THE
MASSACHUSETTS INSTITUTE OF TECHNOLOGY

JUNE 2009

Signature of Author:_____
Department of Mechanical Engineering
May 26, 2009

Certified by:_____
Wai K. Cheng
Professor of Mechanical Engineering
Thesis Supervisor

Accepted by:_____
David Hardt
Chairman, Departmental Graduate Committee

(this page was left intentionally blank)

Extension of the High Load Limit in the Homogenous Charge Compression Ignition Engine

by

Robert J. Scaringe

Submitted to the Department of Mechanical Engineering on May 26, 2009 in Partial Fulfillment of the Requirements for the Degree of Doctor of Philosophy in Mechanical Engineering

Abstract

The Homogeneous Charge Compression Ignition (HCCI) engine offers diesel-like efficiency with very low soot and NO_x emissions. In a HCCI engine, a premixed charge of air, fuel and burned gas is compressed to achieve autoigntion. Combustion occurs throughout the chamber volume resulting in short overall burn duration. This short burn duration can cause excessively high pressure rise rates which lead to unacceptable engine noise and potentially reduced engine life. To combat this high pressure rise rate the engine must be operating with significant diluent, either excess air or burned exhaust gas. However this high level of dilution limits the specific output of the HCCI engine to levels far below spark ignition or diesel engines. The high load limit is a major challenge for the HCCI engine. This study utilized a single cylinder research to examine the high load limit and possible methods to extend it.

The details of the high load limit were first explored across a range of intake temperatures, boost pressures, trapped residual fractions, equivalence ratios and external EGR ratios for a gasoline fueled HCCI engine. A significant finding was that the high load limit always occurs at the misfire limit and that for a given pressure rise rate constraint, the high load limit occurs at lowest possible intake pressure and trapped residual fraction needed to prevent misfire.

A possible means to allow operation at higher boost pressures is to utilize cooled external EGR or to reduce the intake temperature. For a given burn fraction, increasing the EGR rate or reducing the intake temperature provided reduced MPRR. However with these changes, the misfire limit also shifted such that the value of the maximum load does not materially change. Thus boosting coupled with EGR or intake temperature reduction can not be used to significantly extend the high load limit.

A correlation was developed for the burn duration. Multi-zone combustion simulations were used to confirm the form of this correlation. The multi-zone based correlations were then used to quantitatively examine the potential of thermal stratification as a means to extend the high load limit. It was shown that for a doubling of the width of the in-cylinder temperature distribution, a 30% increase in the high load limit is possible.

Thesis Supervisor: Wai K. Cheng
Title: Professor of Mechanical Engineering

Acknowledgements

This work could not have been accomplished without the help of many people. I would like to start by thanking Professor Cheng for his support throughout this project. His guidance and input were critical in both getting the test system running and developing the project strategy. I greatly appreciate his willingness to help solve any problems encountered. His immense technical knowledge, patience, and eagerness to assist make him a great advisor.

I want to thank the other members of my committee, Professor Green and Professor Heywood. Professor Green was always available to explore ideas and discuss our research strategy. His knowledge of combustion chemistry was very valuable in developing our understanding of the HCCI high load limit. Professor Heywood provided great advice on the project direction and his knowledge of internal combustion engines was valuable in understanding and interpreting the data. Additionally Professor Heywood helped keep the big picture and the implications of our work in focus.

I want to thank Craig Wildman who was my research partner for this project. We worked many long days debugging our complicated test system and tracing down problems. Getting the engine running would have been far more difficult without his strong problem solving skills. I also enjoyed working with Craig to explore the data and draw conclusions from it.

The Sloan Laboratory Staff is fabulous and is always available to support the students. During my many visits to the water cooler, Janet Maslow always kept my spirits high. I don't think I have ever seen Janet in bad mood. Karla Stryker was always quick to respond to any problem and I appreciate her patience with my last minute nature. Thane DeWitt's knowledge was critical in getting our test system running. Thane is also a great conversationalist and I very much enjoyed our many discussions. Raymond Phan worked tirelessly to build much of our test system hardware.

I want to thank my friends and family who have been there for me during my time at MIT. From the lab, Simon Watson, Vince Constanzo, Emmanuel Kasseris, Jeff McAulay, Alex Sappok, and Eric Senzer provided both technical and non-technical support. Additionally Tony Ferrer, Erik Thomas and Jon Addison are great friends and always keep me positive. I am also extremely grateful to have my family and their never-ending support.

Lastly I want to thank the Department of Energy who supported this work.

Table of Contents

List of Figures

List of Tables

Nomenclature

ABC	After Bottom Center
ATC	After Top Center
BBC	Before Bottom Center
BMEP	Brake Mean Effective Pressure
CA	Crank Angle
CA10	Crank Angle location of 10% mass fraction burned
CA50	Crank Angle location of 50% mass fraction burned
CA90	Crank Angle location of 90% mass fraction burned
COV	Coefficient of Variation of NIMEP
EGR	Exhaust Gas Recirculation
EVA	Electromagnetic Valve Actuation
EVC	Exhaust Valve Closing
EVO	Exhaust Valve Opening
FTP	Federal Test Procedure
HCCI	Homogeneous Charge Compression Ignition
IVC	Intake Valve Closing
IVO	Intake Valve Opening
MAP	Manifold Absolute Pressure
MON	Motor octane number
MPRR	Maximum Pressure Rise Rate
NIMEP	Net Indicated Mean Effective Pressure
NVH	Noise, Vibration, and Harshness
NVO	Negative Valve Overlap
PFI	Port Fuel Injection
$\tau_{reaction}$	Overall combustion reaction time
UTG	Unleaded Test Gasoline

1 Introduction

The Homogeneous Charge Compression Ignition (HCCI) engine has generated a great deal of interest because it has the potential to provide diesel-like efficiency with very low soot and NO_x emissions. In the HCCI engine, a premixed charge of air, fuel and burned gas is compressed to achieve autoigntion. HCCI combustion begins with ignition at a number of locations within the chamber where the local temperature and/or fuel mixture provide favorable conditions for reaction. If these ignition sites are well distributed, a resulting well distributed decay of fuel concentration throughout the combustion chamber occurs. Section 7 provides a more detailed description of the HCCI combustion process.

The ignition timing is controlled by the local chemistry and temperature; there is no direct means to control the combustion process as there is in a spark ignition or diesel engine. A number of different methods to control combustion timing have been demonstrated. These include: direct intake charge heating [1], use of variable compression ratio to control the charge temperature/pressure [2], use of dual fuels with very different autoignition behaviors [3], and use of variable valve timing to control the amount of hot residual trapped within the cylinder. In this work, a fully variable valve system is used to trap hot residual with a negative valve overlap strategy. With this timing strategy the exhaust valve is closed early during the exhaust stroke and hot burned gases are trapped in-cylinder. The intake valve opening is then retarded to allow most of the work used in compressing the trapped burned gas to be recovered.

The volumetric combustion results in a short overall burn duration. This short burn duration can cause excessively high pressure rise rates which lead to unacceptable engine noise and potentially reduced engine life. To combat this high pressure rise rate the engine must be operated with significant diluent, in the form of either excess air or burned exhaust gas. This high level of dilution limits the specific output of the HCCI engine to levels far below spark ignition or diesel engines. Also note that this high level of dilution reduces the burned gas temperatures thus providing the reduced NO_x emissions.

In addition to its limited high load capabilities, the HCCI engine does not operate at low load and idle conditions because the mixture temperature and pressure are to low for autoignition. The limited operating range of the HCCI engine is demonstrated in Figure 1. Figure 1 shows the second-by-second operating points for a mid-size vehicle (3 liter engine) over the Federal Test

Procedure (FTP) Urban Fuel Economy Drive Cycle [4]. Only 40% of the operating points are within the typical HCCI operating domain.

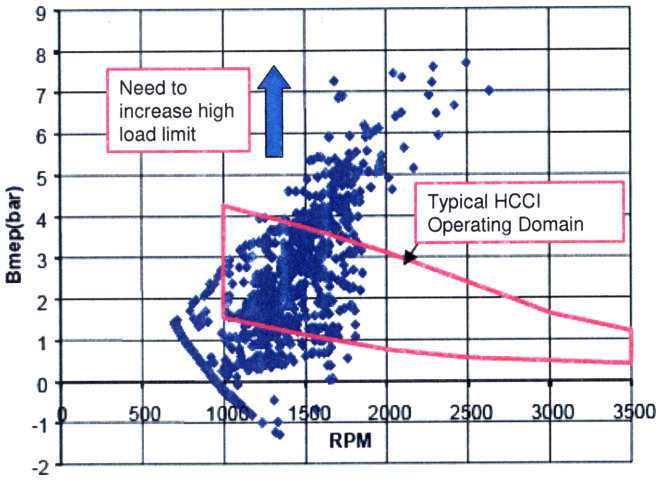

Figure 1.1: HCCI domain over the FTP drive cycle [20]

An approach to dealing with the limited load range of HCCI is to switch to a conventional combustion mode when needed. This switching between modes has been successfully demonstrated by [4,5]. While mode switching will enable commercial HCCI application, expansion of the load range is needed to allow a greater percentage of the operating points to be in HCCI mode. Furthermore expansion of the HCCI load range will reduce the number of mode switches required over a given drive cycle.

It is also important to understand that Figure 1 plots the BMEP, which is proportional to the torque divided by the displaced volume. There is currently a strong push to downsize spark ignition engines. These downsized engines utilize turbo-charging and direct injection to allow very high MEP values. Thus the need to extend the high load limit is even more important if HCCI is to be applied in a duel-mode application with a modern downsized spark ignition engine.

One possible approach to extend the high load limit is to use intake air boosting. Numerous researchers have demonstrated boosting as a means to increase the high load limit [6,7]. However in these studies, the Maximum Pressure Rise Rate (MPRR) was allowed to reach unacceptable levels. Before boosting can be applied to improve the high load limit, a complete understanding of the effect of boosting on the MPRR is needed. Additionally a more complete understanding of the MPRR constrained high load limit is needed.

This work utilized a gasoline fueled single cylinder research engine to develop a full understanding of the MPRR constrained high load limit. The specific objectives of this work are:

1. Understand and characterize the MPRR constrained high load limit
2. Compare the affect of dilution with excess air and cooled EGR on the MPRR
3. Develop correlations to describe the MPRR
4. Use combustion simulations to confirm the form of the MPRR correlation. Use the simulations to explore the effect of stratification on the high load limit
5. Determine if intake boosting coupled with EGR is a viable method to extend the high load limit for MPRR constrained operation

2 Experimental Apparatus

All engine experiments were performed on a single cylinder research engine. The engine apparatus was built to provide a flexible testing platform capable of fully representing a gasoline fueled HCCI engine with:

- turbo-charging,
- fully variable valve timing,
- regenerative intake air heating, and
- external cooled Exhaust Gas Recirculation (EGR)

This flexible test engine consisted of a single cylinder Ricardo Hydra research block that was combined with a VW TDI 1.9 liter head. The camshafts were removed from the head and replaced with an electromagnetic valve actuation (EVA) system. This EVA system was manufactured by Aura System Inc. and allowed independent control of all valve events (IVO, IVC, EVO, EVC). An accelerometer was mounted to the EVA system to allow the timing of the valve events to be determined. The EVA system was controlled using PC based controller developed in the Sloan Lab. Figure 2.1 shows a picture of the engine test apparatus.

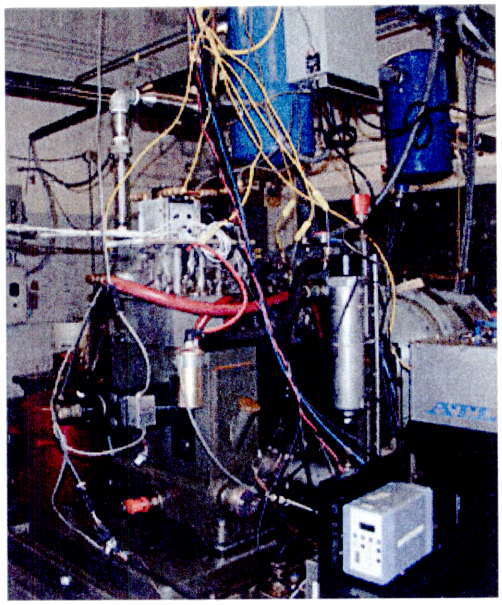

Figure 2.1: Engine Test Apparatus

The engine's compression ratio could be adjusted by placing spacers between crankcase and cylinder. The compression ratio was set to 9.94:1 which corresponds to a modern spark ignition

engine. As discussed in Section 1, a practical HCCI engine will likely have dual mode capabilities, allowing it to switch to spark ignition for high load and idling operation. Thus a compression ratio that corresponded to a modern spark ignition engine was selected. The specifications for the test engine are summarized in Table 2.1.

Table 2.1: Test Engine Specifications

Bore [mm]	80.26
Stroke [mm]	88.90
Connecting Rod [mm]	158
Displacement [L]	449.8
Compression Ratio	9.94:1
Intake Valve Diameter [mm]	28.0
Exhaust Valve Diameter [mm]	30.0
Intake Valve Lift [mm]	4.7
Exhaust Valve Lift [mm]	4.7
Fuel Injector ΔP [bar]	2.7
Piston Geometry	Flat piston

The selected compression or 9.94:1 required that intake air heating be used to enable HCCI operation. In a practical engine this heating would be accomplished with an exhaust regenerative heating system. In the test engine a 3-phase electric heater was used. The intake heater featured a closed loop controller allowing precise intake temperature control.

The single cylinder test engine was coupled to a motoring dynamometer. The dynamometer was used in motoring mode to start the engine and switched to absorption mode once the engine was running. A closed loop dyno controller allowed the engine speed to be maintained at the desired setpoint with a variation of roughly ± 1 RPM.

A schematic of the test system is shown in Figure 2.2. The intake system was designed to enable precise control of the intake charge temperature and pressure. It featured a supercharger taken from a Mini Cooper which was driven by a variable speed electric motor. The inlet side of the supercharger was connected to a damping tank (damping tank #1 in Figure 2.2). The discharge side of the supercharger was connected to a water-cooled intercooler. The intercooler utilized cooling water from the Sloan Laboratory cooling system. The cooling water ranged in temperature from approximately 7°C in the winter to 20°C in the summer. After leaving the intercooler, the air entered the second damping tank which was connected to the first damping

tank with an electrically controlled bypass valve. The bypass valve was used to control the flow and thus pressure of the charge going into the engine.

After leaving the second damping tank, the air flowing into the engine (the air not going through the bypass loop) then passed through the electric heater. After exiting the heater, the air was mixed with external EGR (only for operation with EGR). The EGR mixing location was well upstream of the intake port and the EGR was assumed to be well mixed with the air by the time it entered the engine. A thermocouple located just upstream of the fuel injector tip was used for the heater temperature control. Thus the heater temperature control was based on the temperature of the EGR and air mixture. Note the thermocouple was placed just upstream of the fuel injector to avoid any temperature measurement error due to evaporative cooling of the fuel on the thermocouple probe.

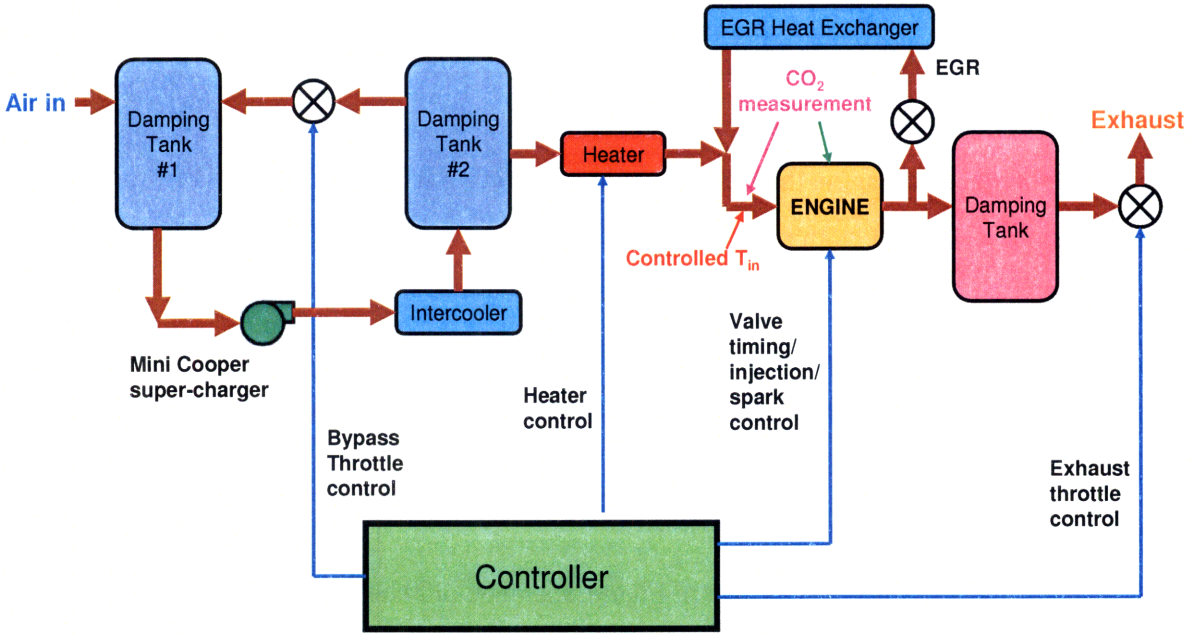

Figure 2.2: Schematic of Engine Test System

The exhaust system featured an electronically controlled butterfly valve to precisely control the exhaust back pressure. To allow operation with EGR, the exhaust pressure was maintained at 0.03 bar above the intake pressure. This enabled burn gases to flow from the exhaust system through an EGR control valve and EGR heat exchanger into the intake system. The temperature of the EGR exiting the EGR heat exchanger was carefully controlled to limit the amount of water condensation from the burned gas. Note that in the most of the non-EGR data, the exhaust

pressure was also maintained at 0.03 bar above the intake pressure however for some of the data recorded early in the project, the exhaust pressure was set equal to the intake pressure. This had minimal effect on the results and the early data can be compared with the later data.

The described supercharger bypass system and exhaust throttle were used rather than an actual turbocharger because they enabled tight control of the intake and exhaust pressure. It is important to realize that the intake to exhaust pressure relationship depends on the turbocharger size and system design as well as the load, boost pressure, and engine speed [8]. Designing a turbocharger system to maintain a desired $P_{intake}/P_{exhaust}$ over a range of operating conditions would have been extremely difficult.

Unleaded Test Gasoline (UTG-91) from Chevron Phillips was injected into the charge (air or air+EGR) with a port fuel injector aimed at the back of the intake valve. The properties of this test fuel are provided in Table 2.2. The injector pressure difference was maintained at 2.7 bar and the duration and timing of each injection were controlled with the PC based engine controller. The injector was calibrated to allow calculation of the fuel mass from the injection pulse width.

Table 2.2: Properties of UTG [9]

Research Octane Number	90.8
Motor Octane Number	83.0
Fuel Sensititivity	7.8
Carbon Content [%]	86.3
Hydrogen Content [%]	13.7
Olefins [vol %]	6
Aromatics [vol %]	23
Saturates [vol %]	70
Stoichiometric n_{O2}/n_{fuel}	12.1

In all tests the engine coolant was maintained at 85°C ±1°C. This corresponds to the temperature at which the thermostat opens in most modern engines [10]. It is important to realize that because HCCI combustion is very sensitive to temperature, the coolant temperature can strongly affect the engine performance.

The fully variable valve timing was used to operate the engine with high levels of trapped residual (30-65%). The residual was trapped using a negative valve overlap (NVO) approach and Figure 2.3 shows a schematic of this valve strategy. With a NVO valve strategy, the exhaust valve is closed early so as to trapped burned gases in-cylinder. The trapped residual gases are

then compressed during remainder of the exhaust stroke. The intake valve opening is retarded to allow the compressed residual gas to be expanded. The intake valve opening is symmetric with the exhaust valve closing to minimize the losses from the recompression of burn gases. The NVO half angle (θ_{NVO}) is defined in Figure 2.3 and this metric is used throughout the study to describe the NVO timing.

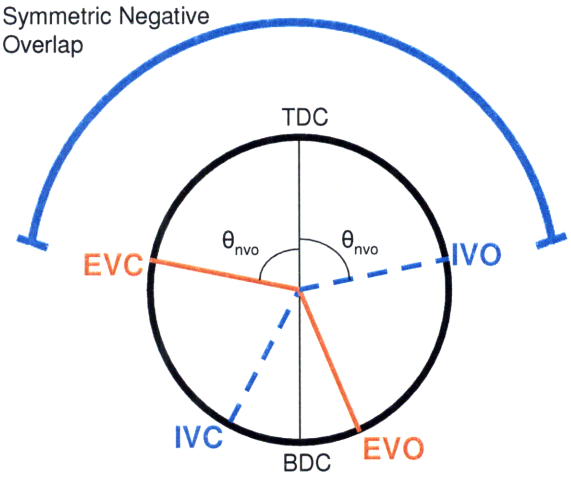

Figure 2.3: Schematic of Negative Valve Overlap Timing Strategy

3 Engine Measurements

Labview 8.2 software was used to record a number of important operating parameters. The in-cylinder pressure and the voltage output from the EVA accelerometer were recorded on a crank angle basis. The MAP and exhaust pressure were recorded on a cycle-by-cycle basis. The temperature of the cylinder head, exhaust gas (in exhaust port), intake mixture (just upstream of the fuel injector), and engine coolant (after exiting the engine) were recorded at a rate of approximately 2 Hz. Additionally the intake CO_2 concentration was measured with a Horiba Mexa 554J analyzer and recorded by hand when operating with external EGR. The cylinder volume was computed from the encoder measured crank angle using the slider crank relationship.

The heat release rate was determined from the pressure and volume data using the Rassweiler and Withrow method. This method is described in detail in Heywood [11]. The IVO, IVC, EVO and EVC timing were determined from the output of the accelerometer mounted to the EVA system.

The calculation/estimation of the EGR rate, residual gas fraction, mixture temperature at 15° BTC and residual temperature at IVO are discussed in the sections below.

3.1 EGR Measurement

The EGR rate was determined using the ratio of the intake mixture CO_2 concentration to the exhaust CO_2 concentration. This ratio is equal to the mole fraction of EGR in the air-EGR mixture just upstream the injector:

$$EGR_{measured} = \frac{[CO_2]_{\text{intake}}}{[CO_2]_{\text{exhaust}}} = \frac{n_{EGR}}{n_{EGR} + n_{air}} \tag{3.1}$$

The intake CO_2 measurement was made was made just prior the fuel injector. The exhaust CO_2 concentration was assumed to be constant at 14%. For stoichiometric operation the CO_2 concentration when none of the water in the reaction products condenses out (dry concentration) is 13.3% and if all the water condenses out (wet concentration) it is 15.2%. Thus a CO_2 concentration of 14% corresponded to about half of the water condensing out of the stoichiometric exhaust gas.

3.2 Residual Gas Fraction Estimation

The burn gas mole fraction is an important parameter for characterizing HCCI operation. It is defined as the ratio of the number of moles of burned gas to the total number of moles.

$$x_{burn,mole} = \frac{n_{EGR} + n_{trap}}{n_{air} + n_{fuel} + n_{EGR} + n_{trap}} \tag{3.2}$$

In equation (3.2) the moles of fuel (n_{fuel}) are determined from the fuel pulse width and injector calibration. The moles air (n_{air}) of are determined using the measured lambda with the number of moles of fuel. The moles of EGR (n_{EGR}) are determined using the measured EGR rate (equation (3.1)) with the calculated moles of air. However the moles of trapped burned gas (n_{trap}) are more difficult to determine. Fast response in-cylinder CO_2 measurements can be used to directly measure the trapped gas fraction however these in-cylinder CO_2 measurements are difficult to perform as the sampling head quickly becomes dirty and must be completely disassembled and cleaned. Thus it was not practical to use in-cylinder CO_2 measurements for the full data set. Instead the in-cylinder CO_2 measurements were used to develop a method to estimate the burn gas fraction.

A fast response non-dispersive infrared detector (NDIR) manufactured by Cambustion was used to make the in-cylinder CO_2 measurements. This analyzer provided a 10-90% signal response time of approximately 8 milliseconds, or 72° at 1500 RPM [24]. This fast response allows measurement of the in-cylinder CO_2 concentration before and after the combustion event. Figure 3.1 shows the in-cylinder CO_2 trace for three consecutive HCCI cycles. The post combustion in-cylinder CO_2 concentration of ~14% is labeled 'b' and the pre-combustion in-cylinder CO_2 concentration is labeled 'a'. The molar burn gas fraction is equal to the ratio of the pre-combustion CO_2 concentration to the post combustion CO_2 concentration:

$$x_{burn} = \frac{n_{EGR} + n_{trap}}{n_{total}} = \frac{a}{b} \tag{3.3}$$

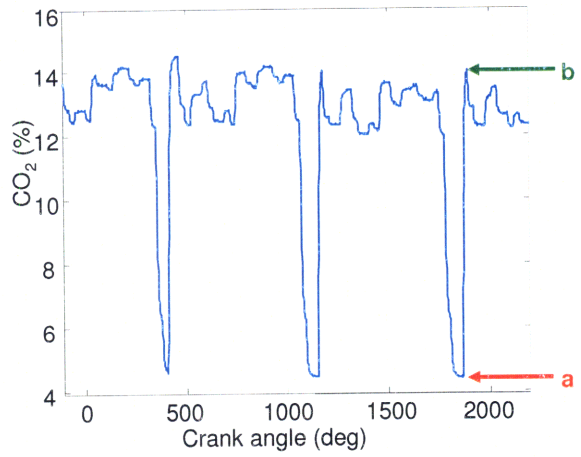

Figure 3.1: In-cylinder CO_2 Measurement

The ideal gas law at exhaust valve closing (EVC) can be used to estimate the moles of trapped residual gas:

$$n_{trap} = \frac{P_{EVC} V_{EVC}}{T_{EVC} R} \tag{3.4}$$

While the pressure and volume are known at EVC, the temperature is not. The temperature is measured in the exhaust port, however this measured temperature represents a multi-cycle average exhaust temperature and because of heat transfer it is lower than the in-cylinder temperature at EVC. However it was found that if the exhaust port temperature and pressure were used with the ideal gas law instead of T_{EVC} and P_{EVC}, the estimated trapped gas fraction (calculated with equation 3.5) was very close that measured using the in-cylinder CO_2 approach.

$$n_{trap,estimate} = \frac{P_{EXH} V_{EVC}}{T_{EXH} R} \tag{3.5}$$

$$x_{trap,estimate} = \frac{n_{EGR} + \frac{P_{EXH} V_{EVC}}{T_{EXH} R}}{n_{air} + n_{fuel} + n_{EGR} + \frac{P_{EXH} V_{EVC}}{T_{EXH} R}} \tag{3.6}$$

Figure 3.2 plots the trapped gas fraction estimated using equation (3.6) as a function of the CO_2 measured trapped gas fraction for a range of trapped gas fractions at several boost pressures. T_{EXH} and P_{EXH} underestimate T_{EVC} and P_{EVC}, however as Figure 3.2 shows, these errors appear to cancel.

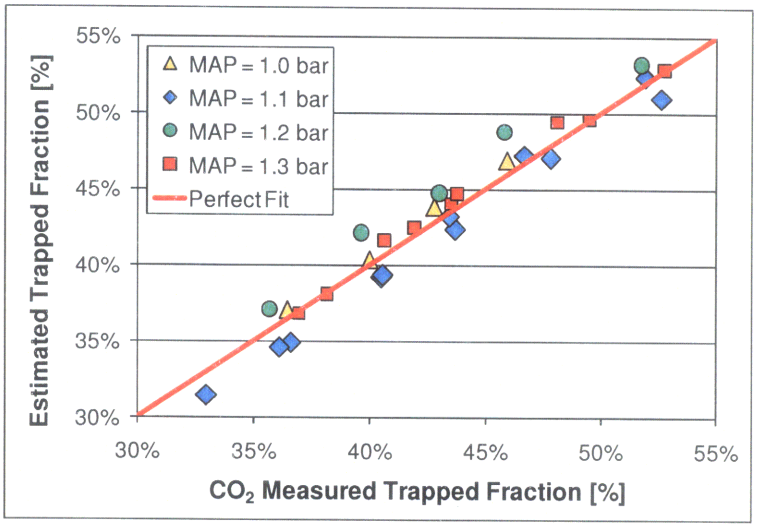

Figure 3.2: Estimated Trapped Fraction versus Measured Trapped Fraction

3.3 Estimation of Temperature at 15º BTDC

The temperature at 15° BTC (T_{15BTC}) was estimated from the ideal gas law:

$$T_{15BTC} = \frac{P_{15BTC} \cdot V_{15BTC}}{n_{total} \cdot R} = \frac{P_{15BTC} \cdot V_{15BTC}}{R} \cdot \frac{1}{n_{air} + n_{fuel} + n_{EGR} + n_{trap}} \tag{3.7}$$

Values for P_{15BTC}, V_{15BTC}, n_{air}, n_{fuel} and n_{EGR} were directly measured or calculated using directly measured values. Equation (3.5) was used to estimate n_{trap}. Unfortunately the test apparatus did not have a way to measure the charge temperature and thus the accuracy of the T_{15BTC} estimate. However the estimated T_{15BTC} values follow expected trends. Figure 3.3 shows T_{15BTC} as a function of the residual gas fraction for stoichiometric operation without EGR for several boost pressures. As can be seen, for residual fractions less than about 45%, increasing the residual fraction provides increased T_{15BTC}. This occurs because for residual fraction less than 45%, the effect of trapping a larger amount of hot burned gases outweighs the reduction in trapped gas temperature that results from increased dilution. For residual fractions greater than 45%, increases in residual fraction lead to reduced T_{15BTC}. This occurs because the effect of reduced burned gas temperature (due to increased dilution) outweighs the effect of trapping a larger amount of burned gases.

Also notice from Figure 3.3, that for a given residual fraction, T_{15BTC} increases with boost pressure. This occurs because as the boost pressure is increased the fueling for a given residual

fraction increases. The increased chemical energy released results in higher engine surface temperatures. The higher engine surface temperatures reduce the heat loss from mixture during the compression process thus leading to increased mixture temperatures at 15° BTC.

While the general trends observed are correct and quite useful for understanding the data, it is shown in later sections that this approach for estimating temperature does not fully capture the actual in-cylinder temperature. In Section 12 it is shown that this approach does not fully capture the effect of EGR on mixture temperature.

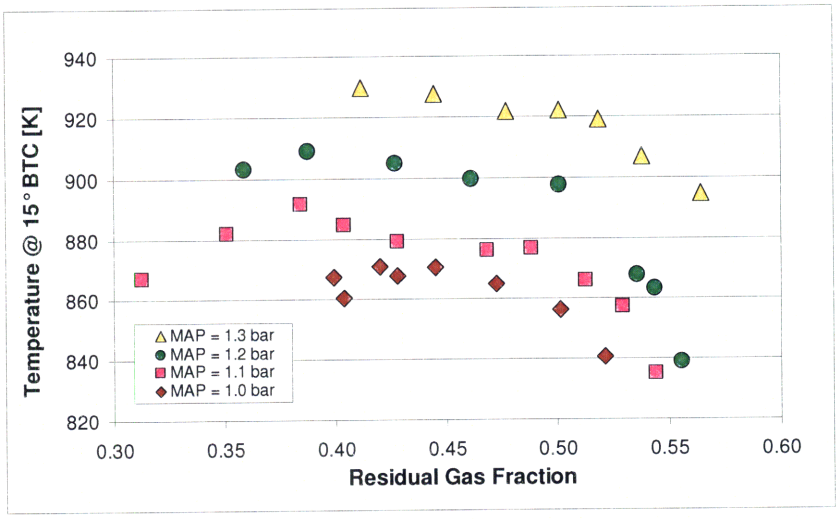

Figure 3.3: Estimated in-cylinder temperature at 15° BTC versus the Residual Gas Fraction. Data from stoichiometric NVO sweeps performed at several pressures and an intake temp of 120°C.

3.4 Estimation of Temperature at IVO

The temperature of the trapped residual at IVO was estimated using the ideal gas law:

$$T_{IVO} = \frac{P_{IVO} \cdot V_{IVO}}{n_{trap} \cdot R} \tag{3.8}$$

Values for P_{IVO} and V_{IVO} were directly measured and equation (3.5) was used to estimate n_{trap}. While the temperature at IVO could not be measured to confirm this method of estimation, the estimated T_{IVO} values follow expected trends. Figure 3.4 shows T_{IVO} as a function of the residual gas fraction for stoichiometric operation without EGR for several boost pressures (the same data set shown in Figure 3.4). With increasing residual gas fraction the estimated temperature of the residual fraction falls. This results because with increased dilution the burned gas temperature falls. Also notice that for a given residual fraction, T_{IVO} increases with pressure.

As with T_{15BTC}, this occurs because as the boost pressure is increased, the fueling for a given residual fraction increases. The increased chemical energy released results in higher engine surface temperatures. The higher engine surface temperatures reduce the heat loss from trapped residual during the negative valve overlap period.

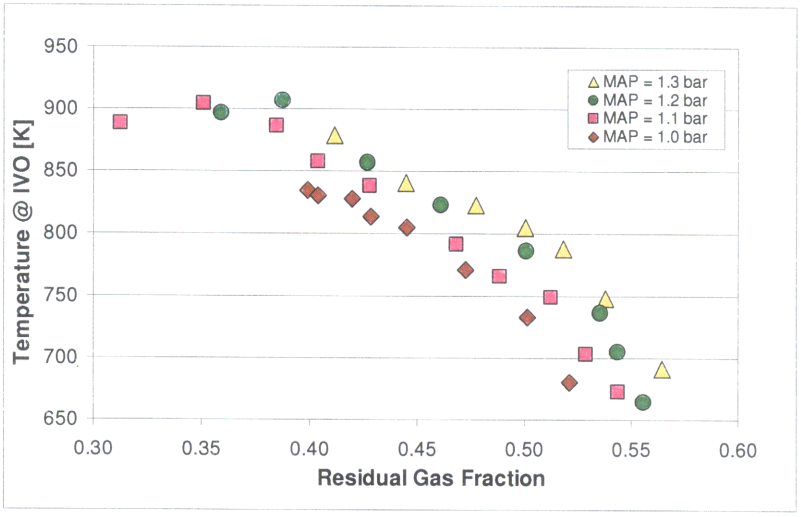

Figure 3.4: Estimated temperature at IVO as a function of the Residual Gas Fraction. Data from stoichiometric NVO sweeps performed at several pressures and an intake temp of 120°C.

4 Experimental Data Set

To enable a complete understanding of the HCCI high load limit a large quantity of data was taken across a range of different intake pressures, intake temperatures, residual fractions, EGR rates and equivalence ratios.

4.1 Stoichiometric NVO Sweeps

NVO sweeps were performed at several intake temperatures and pressures. These sweeps allowed the affects of residual fraction, intake temperature and boost pressure to be examined. Table 4.1 summarizes these sweeps. At each temperature and pressure the NVO timing was swept from a symmetric NVO half angle (θ_{NVO}) of approximately 100° BTC to the lowest θ_{NVO} that could be achieved. The lowest θ_{NVO} was limited either by excessive pressure rise or misfire. To prevent damage to the engine the MPRR was limited to ~20 MPa/ms. The highest value of θ_{NVO} was limited by the valve actuation system. For most operating conditions θ_{NVO} could not be advanced past 100° BTC.

Table 4.1: Stoichiometric NVO Set. NVO sweeps were performed at each temperature and pressure.

Intake Temperature	Intake Pressure [bar]
60°C	1.2, 1.3, 1.4, 1.5
90°C	1.1, 1.2, 1.3, 1.4
120°C	1.1, 1.2, 1.3, 1.4

Section 8.1 presents the stoichiometric NVO sweeps performed at 120°C. The trends observed at 60 and 90°C were comparable and Appendix B provides the corresponding data plots these intake temperatures.

4.2 Stoichiometric Temperature Sweeps

Intake temperature sweeps were performed at intake pressures of 1.0, 1.1, 1.2, 1.3 and 1.4 bar with a fixed NVO timing of 82° BTC. With a fixed NVO timing, the residual fraction was relatively constant and these sweeps allowed the affects of intake temperature be explicitly examined. At each pressure, the intake temperature was swept from 120°C to the lowest value achievable. The lowest temperature achievable was due to misfire for 1.0, 1.1 and 1.2 bar. At 1.3 and 1.4 bar the lowest temperature achievable was due to limitations in test apparatus. Section 8.2 presents these stoichiometric temperature sweeps.

4.3 Examination of Dilution

The effect of dilution with EGR and excess air were examined. To accomplish this, NVO sweeps were performed various fixed dilution levels at several intake pressures. Table 4.2 summarizes these sweeps. At each temperature and pressure the NVO timing was swept from a symmetric NVO half angle (θ_{NVO}) of approximately 100° BTC to the lowest θ_{NVO} that could be achieved. The lowest θ_{NVO} was limited either by excessive pressure rise or misfire. The highest value of θ_{NVO} was limited by the valve actuation system.

Table 4.2: Dilution Sweeps. NVO sweeps were performed at pressure and dilution.

1.1 bar	1.3 bar	1.5 bar
5%	5%, 10%, 15%	10%, 15%, 20%, 23%

Section 8.3 presents the 10% dilution data for 1.3 bar intake pressure. The corresponding plots for 10% and 15% dilution at 1.5 bar are provided in Appendix C. The data for 5% dilution at 1.3 bar is used for generating the operating contours shown in Section 9.

4.4 EGR Sweeps at different intake pressures

To examine the effect of EGR coupled with boosting on the high load limit, EGR sweeps were performed over a range of NVO timings for pressures of 1.1, 1.3, 1.5, 1.7 bar with the intake temperature fixed at 120°C. For each NVO timing, the EGR rate was increased until the engine misfired. Table 4.3 summarizes these sweeps. These sweeps are discussed in Section 12.1.

Table 4.3: EGR sweeps at different intake pressures.

EGR Sweeps performed at each NVO timing (NVO half angle timing in CAD BTC)			
1.1 bar	1.3 bar	1.5 bar	1.7 bar
100°, 95°, 90°, 85°, 80°, 75°, 70°	95°, 90°, 85°, 80°, 75°, 70°	100°, 95°, 90°, 85°, 80°, 75°, 70°	95°, 90°, 85°, 80°, 75°, 70°

4.5 EGR Sweeps at different intake temperatures

EGR sweeps were performed over a range of NVO timings for intake temperatures of 60, 90, 120 and 150°C. For each NVO timing, the EGR rate was increased until the engine misfired. These sweeps allowed the comparison of using EGR to change the mixture temperature versus just changing the intake temperature. That is, for a given burn fraction, does replacing trapped residual with EGR produce the same effect as reducing the intake temperature? Table 4.4 summarizes these sweeps. These sweeps are discussed in Section 12.2.

Table 4.4: EGR sweeps at different intake temperatures.

EGR Sweeps performed at each NVO timing (NVO half angle timing in CAD BTC)			
60°C	90°C	120°C	150°C
100°, 95°, 90°, 85°, 80°, 75°, 70°	95°, 90°, 85°, 80°, 75°, 70°	100°, 95°, 90°, 85°, 80°, 75°, 70°	95°, 90°, 85°, 80°, 75°, 70°

5 Factors controlling the MPRR

HCCI high load operation is often limited by the MPRR. Figure 5.1 shows the ringing intensity [12] as a function of the MPRR for several NVO sweeps. As can be seen the ringing intensity is strong function of the MPRR, thus control of the MPRR is essential for meeting NVH requirements.

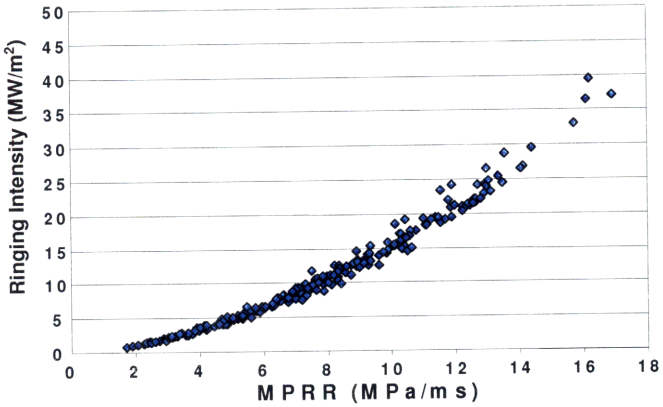

Figure 5.1: Engine Ringing Intensity as a function of the MPRR for several NVO sweeps performed at intake pressures of 1.0, 1.1, 1.2, 1.3, 1.4 and 1.5 bar.

Using the First Law of thermodynamics, the MPRR can be related to basic engine operating parameters. This relationship is derived below and is quite useful for understanding the drivers for reducing the MPRR.

Applying the First Law to the in-cylinder charge and neglecting heat transfer:

$$V\dot{q} = \frac{d(mc_v T)}{dt} + p\frac{dV}{dt} \tag{5.1}$$

Where $\dot{q}$ denotes the volumetric heat release rate. The burned and unburned gases are assumed to behave as ideal gases ($mT = PV/R$) with equivalent constant specific heat ratios. Using the ideal gas relationship, equation (5.1) can be written as:

$$V\dot{q} = c_v \frac{d(PV/R)}{dt} + p\frac{dV}{dt} = \frac{c_v}{R}\left(P\dot{V} + \dot{P}V\right) + p\dot{V} \tag{5.2}$$

Where $\dot{P}$ and $\dot{V}$ refer to dP/dt and dV/dt respectively.

Noting that $C_v / R = (\gamma - 1)^{-1}$, equation (5.2) can be rewritten as:

$$\dot{p} = (\gamma - 1)\dot{q} - \gamma \underbrace{\frac{p\dot{V}}{V}}_{SMALL} \tag{5.3}$$

The second term on the right hand side of equation (5.3) represents the pressure change that results from the movement of the piston. At conditions of MPRR (near TDC) this term is substantially smaller than the heat release term. Thus the pressure rise rate is primarily governed by the heat release rate:

$$MPRR = (\gamma - 1)\dot{q} \tag{5.4}$$

The volumetric heat release rate $\dot{q}(\theta)$ at crank angle θ can be related to the charge with:

$$\dot{q}(\theta) = \frac{LHV\rho_o \left(\frac{V_o}{V(\theta)}\right)(1 - x_b)\frac{1}{1 + A/F}}{\tau_{reaction}} \tag{5.5}$$

Where LHV is the Lower Heating Value of the fuel, ρ_0 is the charge density when the cylinder volume is V_0 and $\tau_{reaction}$ combustion reaction time. Note that with boosting ρ_0 increases and $\tau_{reaction}$ decreases thus leading to increased volumetric heat release. Equation (5.5) can be put into simpler terms using the following relationship for fuel mass per cycle:

$$m_{fuel} = \frac{\rho_{\theta=IVC}(1 - x_b)V_{\theta=IVC}}{1 + A/F} \tag{5.6}$$

Where $\rho_{\theta=IVC}$ and $V_{\theta=IVC}$ are the charge density and volume at IVC.

Substituting equations (5.5) and (5.6) into equation (5.4) provides the following relationship for MPRR:

$$MPRR = \frac{1}{\tau_{reaction}} \frac{(\gamma - 1)m_{fuel} LHV}{V(\theta_{MPRR})} \tag{5.7}$$

To increase fueling while controlling the MPRR, the potential parameters to control are $\tau_{reaction}$, $V(\theta_{MPRR})$, and γ. Notice that burn gas fraction, charge pressure and charge temperature are not explicitly in equation (5.7) but are captured by $\tau_{reaction}$, $V(\theta_{MPRR})$, and γ.

While γ changes with burned gas fraction, the maximum possible change is only on the order of a couple percent. The potential for changing the volume MPRR is also limited. As shown in Table 5.1 below, the volume at 15° ATC is only 19.7% greater than the volume at top center.

Table 5.1: Volume Increase with Crank Angle

MPRR CAD ATC	Volume Increase over TC
5°	2.2%
10°	8.8%
15°	19.7%

Equation (5.7) can be related to the mean effective pressure (MEP) with the following equation for the fuel mass:

$$m_{fuel} = \frac{MEP \cdot V_{displaced}}{LHV \cdot \eta} \tag{5.8}$$

Substituting equation (5.8) into (5.7):

$$MPRR = \frac{1}{\tau_{reaction}} \frac{(\gamma - 1) MEP \cdot V_{displaced}}{\eta \cdot V(\theta_{MPRR})} \tag{5.9}$$

Ignoring the effect of combustion phasing on the thermal efficiency (η), retarding the MPRR location from top center to 15° ATC will allow for an increase in MEP of less than 20%. Thus the reaction time ($\tau_{reaction}$) is the parameter which must be focused on for controlling the MPRR while increasing the fueling.

Equation (5.7) can be applied to engine operating points using the 10-90% burn duration to represent $\tau_{reaction}$ and the crank angle location of 50% mass fraction burned (CA50) to represent the location of MPRR:

$$MPRR = \frac{1}{BD_{10-90}} \cdot \frac{(\gamma - 1) \cdot m_{fuel} \cdot LHV}{V_{CA50}} \tag{5.10}$$

Equation (5.10) was confirmed using the entire data set. Figure 5.2 shows $MPRR \cdot BD_{10-90} \cdot V_{CA50}$ as a function of $(\gamma - 1) \cdot m_{fuel}$. As can be seen, the data set collapses extremely well.

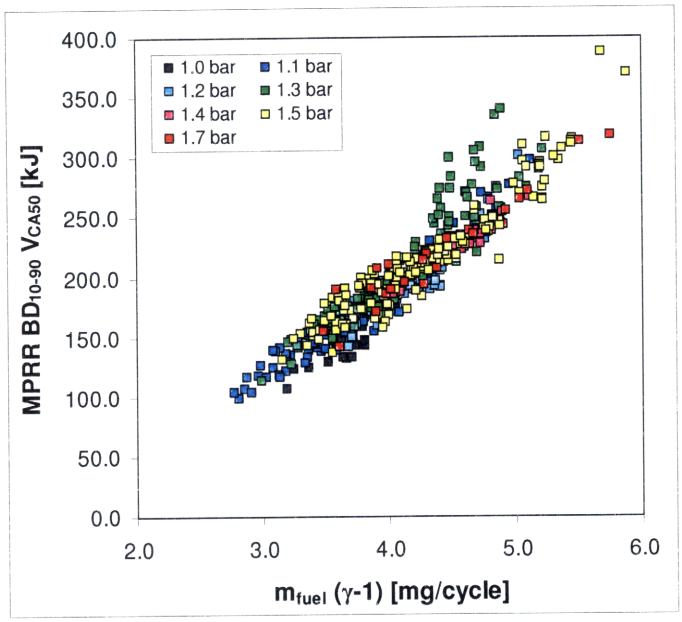

Figure 5.2: $MPRR \cdot BD_{10-90} \cdot V_{CA50}$ versus $(\gamma - 1) \cdot m_{fuel}$ for the entire data set

Equation (5.7) can also be rearranged for $\tau_{reaction}$ and used with measured values for $MPRR$, V_{CA50}, m_{fuel} and γ:

$$\tau_{reaction} = \underbrace{\frac{1}{MPRR} \cdot \frac{(\gamma - 1) \cdot m_{fuel} \cdot LHV}{V_{CA50}}}_{\text{Meausred Quantities}} \tag{5.11}$$

Figure 5.3 shows $\tau_{reaction}$ calculated with equation (5.11) as a function of the measured 10-90% burn duration. As can be seen, the developed relationship accurately describes the data set.

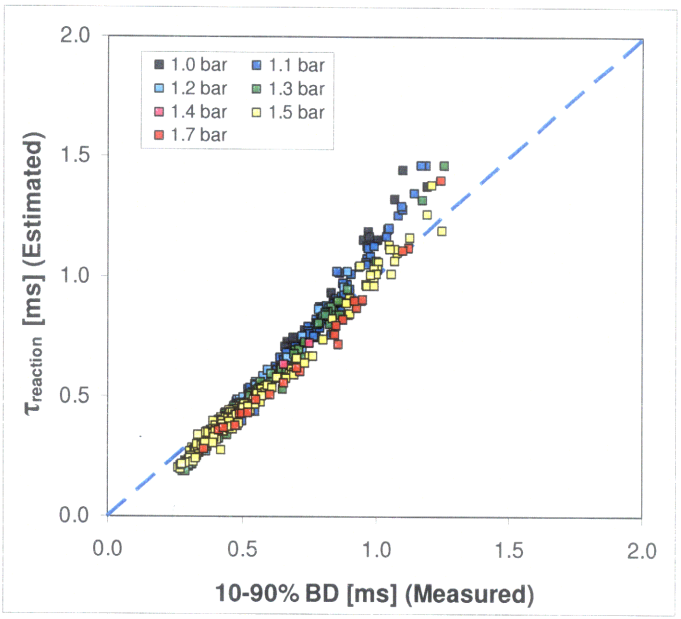

Figure 5.3: $\tau_{reaction}$ calculated with equation (5.11) versus the measured 10-90% BD for the entire data set

6 HCCI multi-zone model

A multi-zone combustion model was utilized to better understand the parameters controlling the MPRR. The multi-zone model was used to simulate HCCI combustion across a range of operating conditions for three different stratification conditions. The resulting pressure profile and zone heat release outputs were used to confirm the form of the correlation for $1/\tau_{reaction}$ developed using engine data (Section 10.3). The $\tau_{reaction}$ correlations obtained using the multi-zone model were then utilized with WAVE to examine the HCCI operating region (Section 11). This section describes the multi-zone model and the matrix of simulations used in Section 10.3 for the $1/\tau_{reaction}$ correlations.

6.1 Description of the multi-zone model

A multi-zone HCCI model from Numerica Technology LLC was used for simulations. In this model each zone is treated as a single lumped mass with uniform composition and temperature. The zones are not defined spatially and there is no heat or mass transfer between the zones; the chemistry of each zone is treated independently. The only coupling between the zones is through the pressure which is assumed to equilibrate instantaneously during the heat release process. The total volume of all the zones was computed using the slider crank relationship [11], with the same engine dimensions as the experimental engine. Each of the zones had equivalent mass, therefore the volume of each zone was dependant on its temperature relative to the other zones. Ten zones were used to provide a relatively smooth pressure rise rate. While using fewer zones would have reduced the computation time, the resulting reaction pressure rise would have had more of a "staircase" profile and interpreting the MPRR would be more difficult.

A large matrix of simulations was required to develop the $1/\tau_{reaction}$ correlations. Therefore a full detailed mechanism would not have been practical. A simplified reaction mechanism developed by Tanaka et al. was utilized [13, 14]. This simplified mechanism consisted of 32 species and 55 reactions and provided sufficient accuracy with quick computation times.

Using the simplified Tanaka mechanism with a 2.1 GHz processor produced computation times between 1 and 4 minutes. The model was run using Numerica's Jacobian solver software. This software utilizes matrix scarcity to more quickly complete simulation computations.

Iso-octane was used in all simulations. Iso-octane was used rather than a PRF with a lower volume percentage of iso-octane (i.e. PRF90) because it has a very limited first stage ignition. Iso-octane's single stage ignition is similar to the that of gasoline.

The simulation was run from 38 ABC to 126 ATC. The start of the simulation at 38 ABC corresponds to conditions after intake valve closing. The initial global pressure was specified along with the temperature, burn gas fraction and equivalence ratio for each zone. Air was assumed to consist only of N_2 and O_2 with a molecular ratio of 3.773 to 1.

6.2 Simulation Matrix

A large matrix of simulations was needed to sweep out the parameters in the $1/\tau_{reaction}$ correlation. To accomplish this, simulations were performed across a range of pressures, temperatures, burn fractions and equivalence ratios. Table 6.1 summarizes the sweeps performed.

Table 6.1: 10-zone simulation matrix

	Average Temp @ IVC	Pressure @ IVC	Initial Burn Gas Fraction	Lambda
Temperature Sweeps	#1	1.5	0.500	1.0
	#2	1.5	0.350	1.0
	#3	1.5	0.450	1.0
	#4	1.3	0.300	1.0
Pressure Sweeps	511	#1	0.400	1.0
	522	#2	0.500	1.0
	516	#3	0.450	1.0
	501	#4	0.300	1.0
	526	#5	0.350	1.0
Burn Gas Fraction Sweeps	516	1.4	#1	1.0
	524	1.3	#2	1.0
	511	1.5	#3	1.0
	516	1.3	#4	1.0
Lambda Sweeps	506	1.5	0.350	#1
	506	1.3	0.300	#2
	526	1.1	0.350	#3
	516	1.4	0.375	#4

The composition stratification was linked to the temperature stratification by assuming adiabatic mixing between the cool fresh charge and hot residual as discussed in Appendix A. A quadratic temperature profile was used in all simulations and this produced pressure traces similar to that of the engine. Figure 6.1 compares the measured pressure trace with that obtained using the 10-zone simulation. The quadratic temperature profile used in this simulation had a thermal width (defined as the difference between the temperature of the hottest and coolest zones) of 50K. The burn fraction and pressure at IVC were the same for both the simulation and the experiment with

values of 50% and 1.35 bar respectively. The bulk temperature of the simulation was adjusted such that the pressure traces lined up.

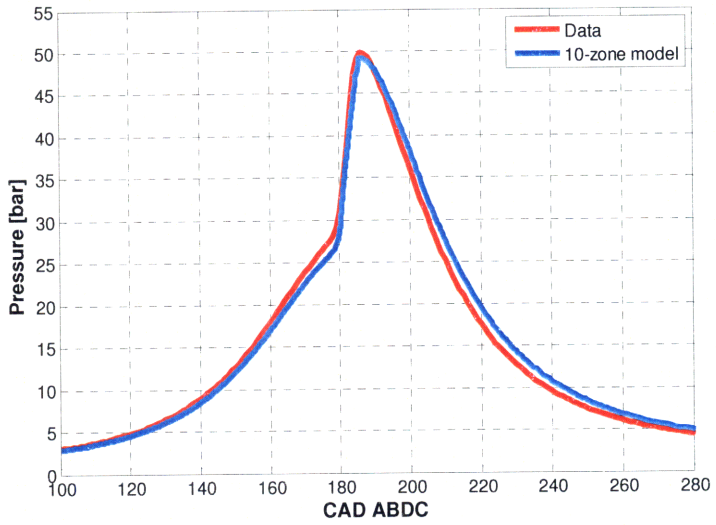

Figure 6.1: Comparison of measured and simulated pressure. TW = 50K; x_{burn} = 50%; P_{IVC} = 1.35 bar

Three different stratification conditions were considered and these are provided in Table 6.2. The simulation matrix shown in Table 6.1 was performed for each of these stratification conditions. The equivalence ratio and burn fraction profiles for the third stratification condition in Table 6.2 were calculated from the temperature profile assuming adiabatic mixing (this is described in Appendix A). Figure 6.2 shows temperature profiles for TW = 25K and TW =50K for an equivalent bulk temperature of 521K.

Table 6.2: Stratification Conditions Considered.

#	Temperature Profile	Equivalence Ratio Profile	Burn Fraction Profile
1	Quadratic with TW = 50K	Constant	Constant
2	Quadratic with TW = 25K	Constant	Constant
3	Quadratic with TW = 50K	Based on temperature profile assuming adiabatic mixing	Based on temperature assuming adiabatic mixing

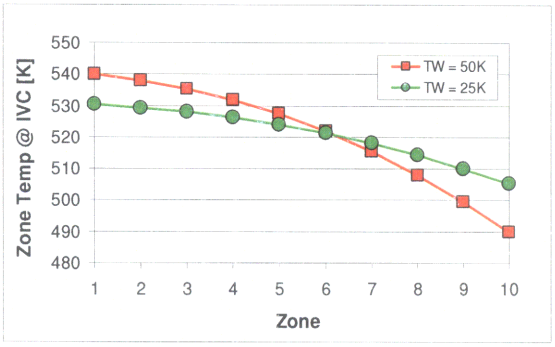

Figure 6.2: TW = 25 K and TW = 50 K temperature profiles for a bulk temperature of 521 K.

Figure 6.3 shows the simulated 10-90% burn duration as a function of the CA50 for the entire simulation matrix at each stratification condition. As explained in Section 7.2.1, increases in the thermal stratification retard the phasing and lengthen the duration. As the composition stratification was determined assuming adiabatic mixing, the higher temperature zones had higher burn gas fractions (lower oxygen fractions) and reduced fuel content while the lower temperature zones had lower burn fractions (higher oxygen fractions) and increased fuel content. These effects cause the high temperature zones to ignite later and the low temperature zones to ignite earlier thus shortening the burn duration. This retarding of the phasing and shortening of the burn duration for the composition stratified case was observed in the simulations, however the shortening effect was relatively small.

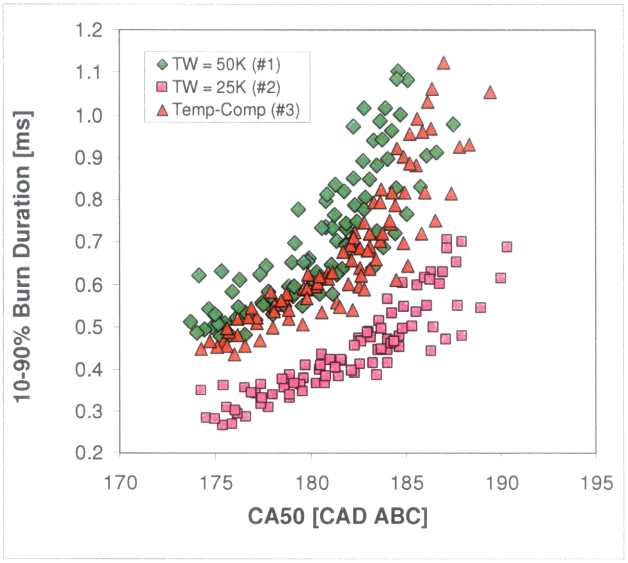

Figure 6.3 10-90% Burn Duration versus CA50 for simulation points at the three stratification conditions

7 HCCI combustion, burn duration and combustion phasing

The HCCI combustion process and the effect of temperature and composition stratification are described in this section. Furthermore the relationship between the combustion phasing and duration is explored.

7.1 HCCI Combustion

HCCI combustion begins with ignition at a number of locations within the combustion chamber where the local temperature and/or fuel mixture provide favorable conditions for reaction. This process is distinctly different from a propagating turbulent flame as in a spark ignition engine. The heat release process is not controlled by heat and species transport processes across sharp concentration and temperature gradients between the burned and unburned gases.

Figure 7.1 is a sequence of chemiluminescence images showing the HCCI combustion process taken at Sandia [15]. These images were taken on a 0.98 liter direct injection HCCI engine with a compression ratio of 18:1. The engine was operating at 1200 RPM with iso-octane fueling with lambda set to 4.17 and minimal burn gas fraction. While these conditions differ from that of this study, the volumetric combustion process is accurately captured. Furthermore these images are useful in understanding the sequential nature of HCCI combustion.

In Figure 7.1 the combustion begins in the upper left and lower right corners which are presumably the hottest regions in the field of view. As the combustion proceeds, these areas become brighter and as the global pressure rises, other areas begin showing chemiluminescence. The region just to the left of center does not begin burning until combustion is well underway in the other regions. This region likely is the coldest in the field of view.

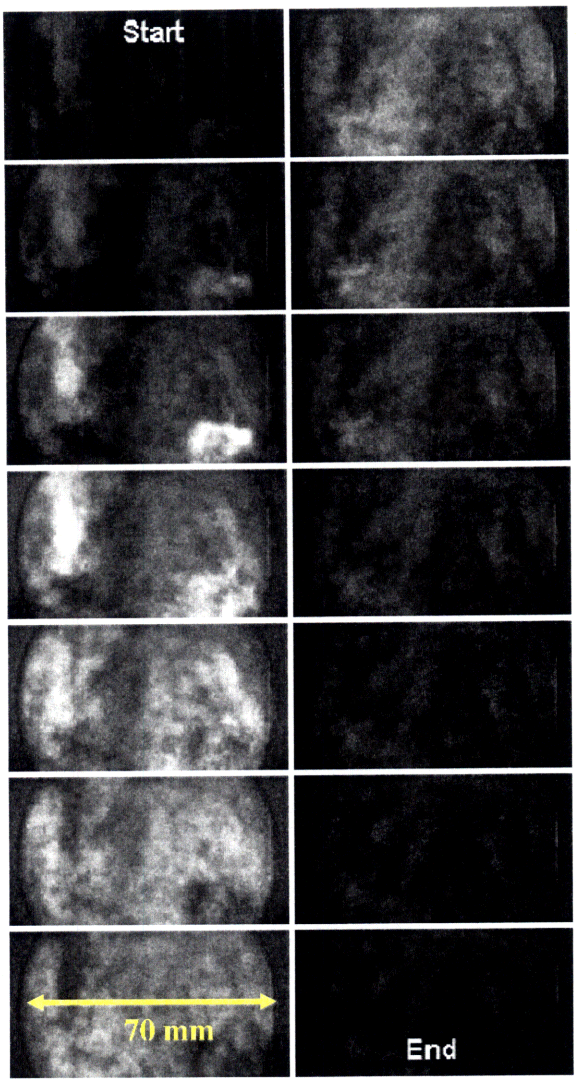

Figure 7.1: HCCI Combustion Sequence taken from [15]. The interval between the frames is 0.71°.

The combustion sequence shows that the HCCI reaction occurs sequentially as various regions ignite and then burn out. There are no strong reaction gradients in the images and the smooth changes in the chemiluminescence intensity provide no indication of a propagating flame front. Furthermore as [15] points out, the rate at which the chemiluminescence spreads, far exceeds typical turbulent flame speeds. For example between the first and second frame, the chemiluminescence goes from the bottom right all the way to the top of the frame. This is a distance of approximately 25 mm and for propagating flame to cover this distance would require a flame speed of 250 m/s (the time between images is 100 μs). This is more than an order of magnitude greater than a typical turbulent hydrocarbon flame speed [11].

The combustion process thus appears to be a sequential ignition of progressively cooler regions. The cooler regions ignite later as the global pressure rise results in conditions favorable for reaction [15]. Imaging experiments performed by Hultqvist et al. [16] had nearly identical findings.

It is also interesting to note from Figure 7.1 that there is no significant fluid motion during the combustion process. Heywood [11] states that a typical turbulent velocity at TDC is roughly half the mean piston speed, which is 2.4 m/s for this operating condition. This velocity would produce a motion of only 0.24 mm between frames.

This understanding of the HCCI sequential ignition process is useful in qualitatively understanding the relationship between the combustion phasing and duration. The initial ignition occurs at the location where the temperature, pressure, oxygen fraction and fuel content provide the minimum ignition delay timing. The form of the ignition delay time can be written as:

$$\tau_{ignition} = A \cdot P^{n} \cdot \phi^{m} \cdot x_{O_2}^{k} \cdot \exp\left(\frac{E_a}{R \cdot T}\right) \tag{7.1}$$

He et al. [17] recently studied the autoignition of iso-octane under HCCI conditions using a rapid compression machine. The ignition delay was measured over a range of equivalence ratios ($\phi = 0.25 - 1.0$), pressures (P = 5.12 – 23 *atm*), temperatures (T = 943 – 1027 K), and oxygen mole fractions ($x_{O_2} = 9 - 21\%$) as described more fully in [9]. The data was used to determine the constants in equation (7.1) with a R^2 of 0.98:

$$\tau_{ignition} = 1.3 \times 10^{-4} \cdot P^{-1.04} \cdot \phi^{-0.77} \cdot x_{O_2}^{-1.41} \cdot \exp\left(\frac{33{,}700}{R_{(cal/mol-K)} \cdot T}\right) \tag{7.2}$$

In equation (7.2), $\tau_{ignition}$ is in ms, P is in atm, and T is in K. The experiments conducted to obtain equation (7.2) were made using N_2 as the balance gas. The equivalence ratio was thus calculated using the iso-octane to O_2 molar ratio. The study also examined how the addition of H_2O and CO_2 affect the ignition delay. According to [17], the potential effects of H_2O and CO_2 can be grouped into two categories: physical effects and chemical effects. The physical effects are due to the large heat capacities of the tri-atomic CO_2 and H_2O (compared to N_2). This heat

capacity effect can be captured by the temperature component in (7.2). The addition of CO_2 appears to have no chemical effect on the ignition delay for the HCCI conditions studied. The addition of H_2O however did lead to reduced ignition delay times; the average reduction for addition of 3% H_2O (molar basis) was 7.1%.

He et al. [9] also evaluated the performance of several iso-octane mechanisms at reproducing the measured ignition delay times. Of these, the reduced kinetic model developed by Tanaka et al. [13, 14] was evaluated. This Tanaka model was used in the HCCI modeling work discussed in Section 6. The trends predicted by the Tanaka model were in very good agreement with the experimental measurements performed by He et al [17]. Table 7.1 compares the constants corresponding to the ignition delay model given by equation (7.1).

Table 7.1: Comparison of He et al. [17] and Tanaka et al. [13,14] iso-octane ignition delay function. Constant parameters correspond to ignition delay function given by equation (7.1)

	A	E_a *(kcal/mol)*	*n*	*m*	*k*
U. Michigan [17]	1.30E-04	33.7	-1.05	-0.77	-1.41
Tanaka et al. [13, 14]	1.28E-04	33.8	-1.01	-0.81	-1.73

7.1.1 Relationship between the ignition delay and burn duration

The burn duration can be interpreted as the time between the ignition of the parcel with the shortest ignition delay and the ignition of the parcel with the longest ignition delay. The global pressure rise associated with the ignition of the early parcels will shorten the ignition delay of the later burning parcels. The combustion process is generally less than a millisecond in duration and thus heat transfer between the regions is minimal and the shortening of the latest ignited region is due primarily increased pressure that results from the combustion of the earlier parcels. While the earliest burning parcels are typically in the hottest regions of the charge and the latest burning parcels are typically the coldest regions of the charge, it is important to note from equation (7.1) that temperature is not the only factor which determines ignition delay.

The ignition timing of the earliest burning parcels relative to latest burning parcels depends on the charge stratification, both in temperature and composition. For an equivalent bulk temperature, a charge with a large temperature stratification will lead to hotter hot parcels and cooler cold parcels. This will result in an earlier start of combustion (due to the hotter hot

parcels) but a longer burn duration (due to the later burning cooler cold parcels). Thus for equivalent start of combustion timing, the burn duration can be very different depending on the stratification.

Holding stratification constant, increasing in the bulk temperature, pressure, oxygen fraction, or fueling will reduce the ignition delay for both the earliest parcel and the latest parcel. However for this to produce a reduction in the total burn duration, ignition of the latest parcel needs to advance by more than the earliest parcel. It turns out that this is the case; when the bulk temperature, pressure, oxygen fraction, or fueling are increased, both the phasing advances and the burn duration is reduced. This results because, for a given fueling (total heat release), with earlier phasing the pressure rise is greater and the later burning parcels will ignite earlier (due to the pressure dependence of the ignition delay).

To summarize, the burn duration and combustion phasing both depend on the parameters given by the ignition delay. Thus increases in pressure, temperature, oxygen fraction or fuel fraction will lead to earlier combustion and shortened duration.

7.2 Effect of Stratification on HCCI Combustion

Stratification, both of temperature and composition, plays an important role in determining the timing and duration of the HCCI combustion event. Recently researchers have begun examining stratification as a means to lengthen the burn duration and thus allow increases in the high load limit while maintaining the MPRR at acceptable levels. In this section the results of some of the notable stratification studies are presented. Additionally the 10-zone model described in Section 6 is used to explore the effect of stratification.

7.2.1 Temperature Stratification

The influence of thermal stratification on the HCCI combustion process has been demonstrated by several researchers using both modeling [18] and experimental [19, 20] methods. The study performed Kakuho et al. [20] is reviewed here. In [20], a laser induced fluorescence (LIF) visualization technique was used to examine the influence of controlled non-uniform temperature distributions prior to combustion. The non-uniform temperature distributions were achieved by separating the two intake runners and independently controlling the temperature in each. The effect of the induced temperature distribution on the heat release rate for operation with n-

heptane (A/F = 32) at 800 RPM is shown in Figure 7.2. ΔT in Figure 7.2 refers to the difference in temperature between the two intake runners. The average bulk intake temperature in all cases was maintained at 398K. Increasing the thermal stratification was found to advance the start of combustion and lengthen the burn durations.

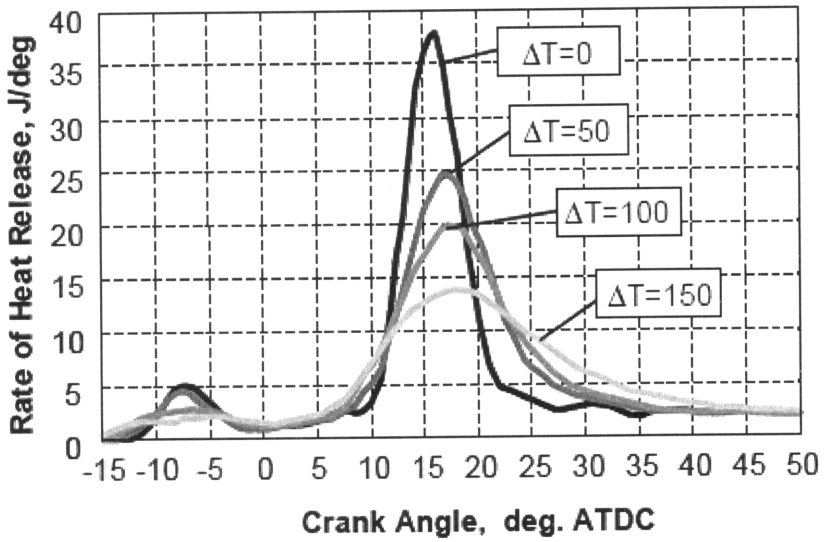

Figure 7.2: Effect of temperature stratification on heat release. ΔT refers to the difference in temperature between the two intake runners [20]

The ten-zone combustion model described in Section 6 was used to demonstrate the effect of thermal stratification. Three different temperature profiles were examined and are shown in Figure 7.3. All three had a quadratic form and the same average temperature of 520.8 K. The thermal width (TW), defined as $T_{max} - T_{min}$, for the three profiles was 25 K, 50 K, and 75 K. To isolate the effect of temperature, the burn gas fraction and fueling were fixed across all zones with $x_{burn} = 0.45$ and $\lambda = 1.00$. The pressure at IVC was set to 1.5 bar for all three simulations.

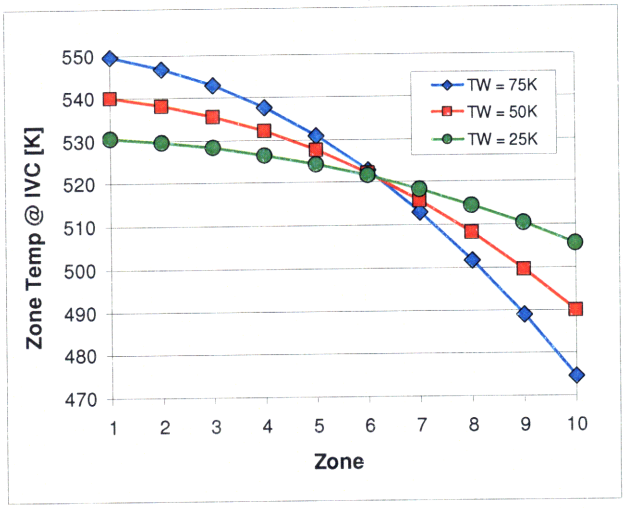

Figure 7.3: Temperature profiles used in stratification modeling study. Average temperature = 520.8 K.

Figure 7.4 shows the simulated pressure trace for the three temperature profiles provided in Figure 7.3. Additionally as a reference, the pressure trace for a homogenous charge is shown. The resulting MPRR are indicated in the figure key. Increasing the thermal stratification lengthened the combustion duration and provided sizable reductions in the MPRR. Also note that with increased thermal stratification the start of combustion occurred earlier because the temperature of the hottest zone increased. Similar results were obtained by Sjoberg et al. [18] using a 5-zone combustion model.

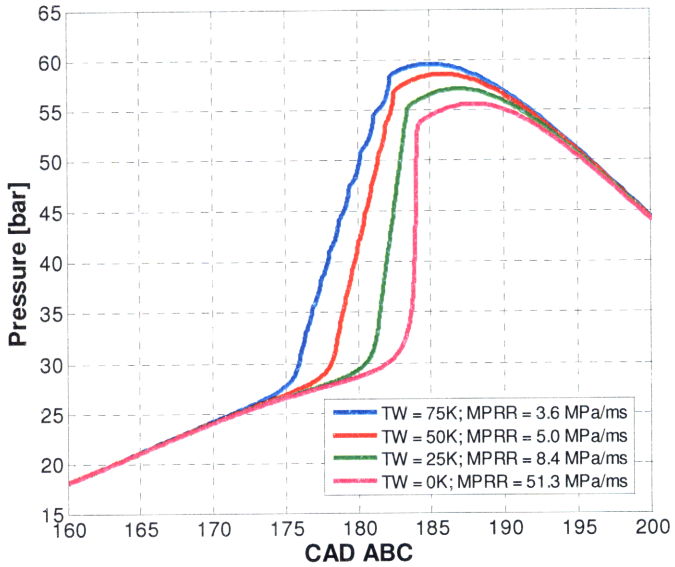

Figure 7.4: Simulated pressure trace corresponding to temperature profiles given in Figure 7.3. $T_{average}$ = 520.8 K; x_{burn} = 0.35; λ = 1.00; P_{IVC} = 1.5 bar

7.2.2 Impact of Residual Gas Fraction on Temperature Stratification

The in-cylinder temperature stratification has been shown to correlate with the residual gas fraction for NVO operation. In an excellent study by Babajimopoulos et al. [21] a multi-dimensional fluid mechanics code (KIVA) was used to model the gas exchange process of an HCCI utilizing high levels of trapped residual through an NVO strategy. Figure 7.5 shows snapshots of the in-cylinder flow field during the intake and compression strokes for an NVO timing of 60° BTC. The sequence of images starts 5° after IVO and ends 30° BTC. The equivalence ratio in the intake port was 0.3 and the residual gas fraction was 0.42.

The contours show the local equivalence ratio and the vectors indicate the local velocity direction. During the intake process the interaction of the fresh charge with the trapped residual can clearly be seen. The areas of high equivalence ratio indicate higher fractions of fresh charge. At 30° BTC the there exists significant stratification of the equivalence ratio and thus the fresh charge and trapped residual are not fully mixed. To better examine the temperature and equivalence ratio stratification that exists at 30° BTC, Babajimopoulos et al. [21] took three cross sections of the cylinder as shown in Figure 7.6. Figure 7.7 shows the temperature and equivalence ratio contours that correspond to these three cross sections.

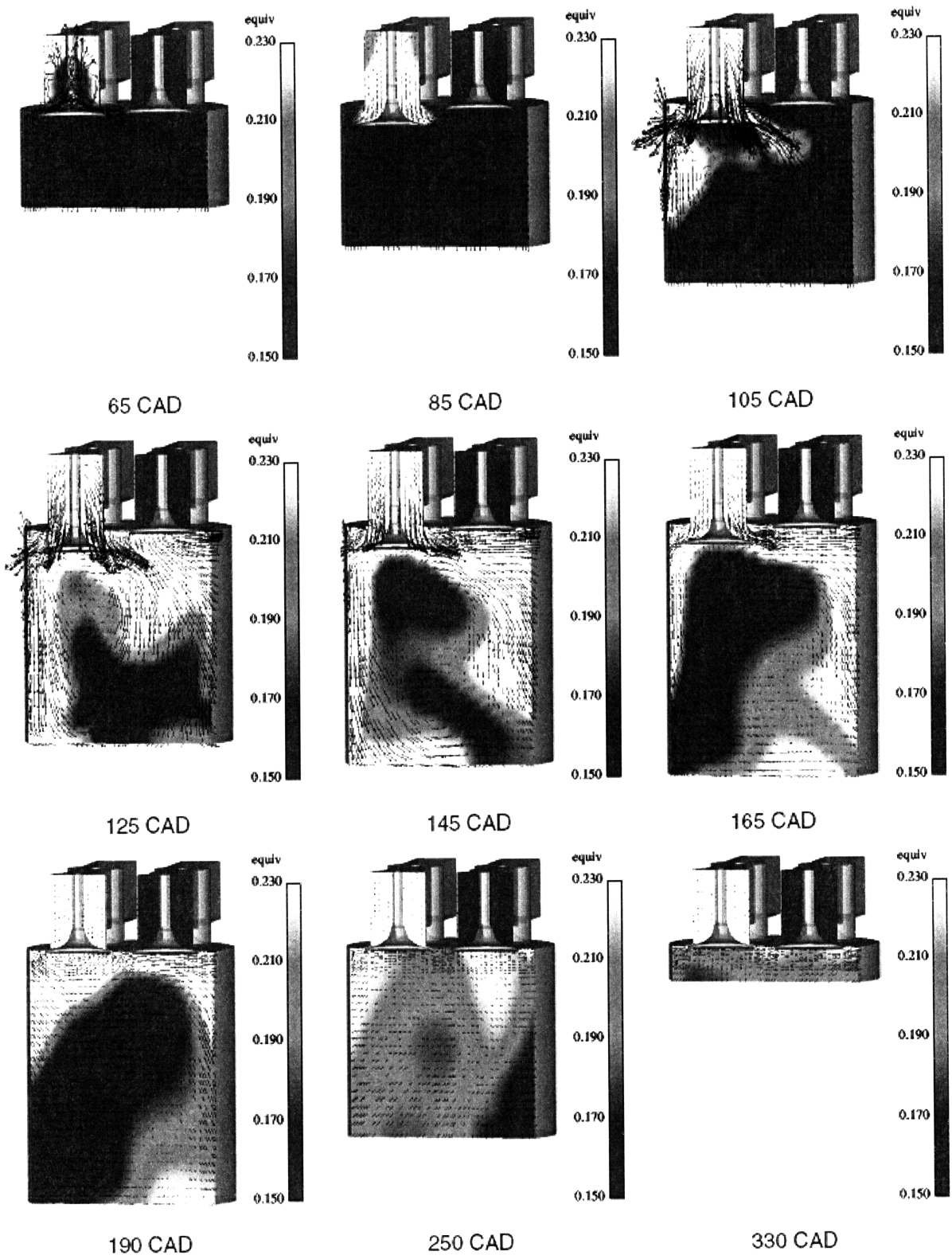

Figure 7.5: KIVA generated snapshots of the in-cylinder flow field during the intake and compression stroke with an NVO timing of 60° BTC. The equivalence ratio in the intake port was 0.3. The contours show the local equivalence ratio and the vectors indicate the local velocity direction. [21]

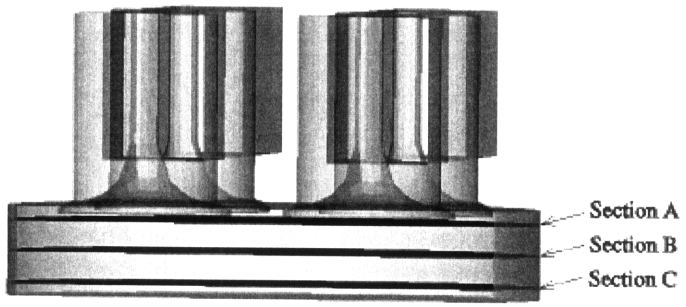

Figure 7.6: Cross sections taken of Figure 7.5 at 330 CAD [21]

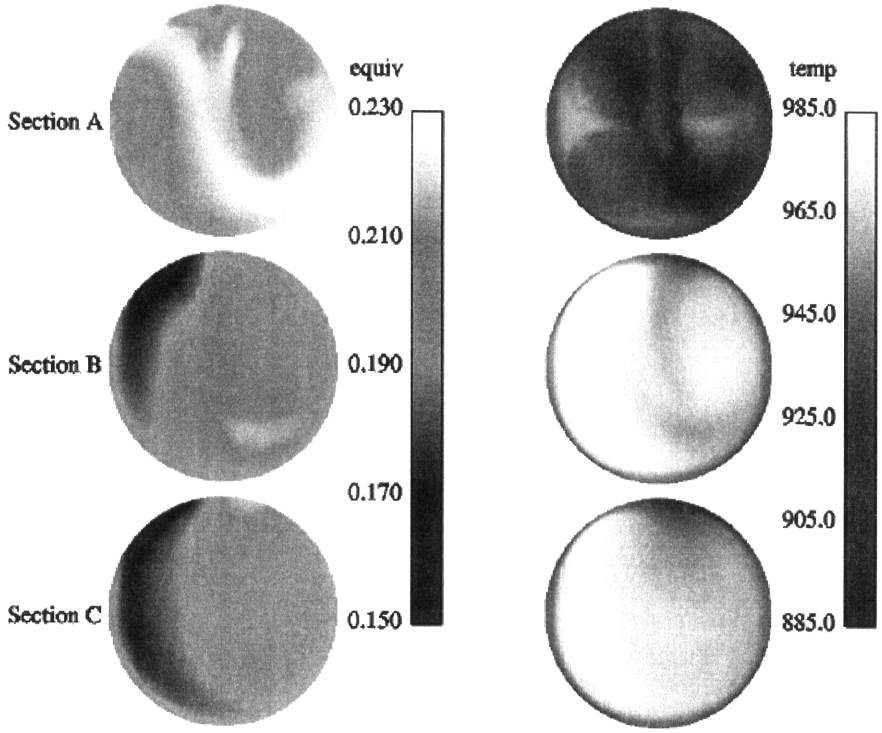

Figure 7.7: Equivalence ratio and temperature contour plots for three cross sections of 330 CAD in Figure 7.5. The location of each cross sections defined by Figure 7.6 [21]

Figure 7.7 clearly shows that there is a correlation between the local equivalence ratio and the local temperature. The areas of low equivalence ratio occur where there are high levels of residual and thus the temperature is higher. This is most clear in section B, where heat transfer to the head and piston is reduced. This indicates that the richest regions of the chamber will correspond to the coolest regions. It is also worth pointing out the equivalence ratio is higher near the cylinder head and that the temperature is highest in section B. The study [21] also showed that the temperature and equivalence ratio ranges increases with increasing residual gas

fraction for residual fraction ranges of 0.058 to 0.42. This is because with higher levels of trapped residual, incomplete mixing will lead to increased temperature and composition spreads.

In a follow-up study by Babajimopoulos et al. [22], the effects of heat transfer and mixing on the temperature and equivalence ratio linkage were examined using a KIVA model described in detail in [21]. The effect of mixing and heat transfer were decoupled by running the model with the heat transfer to the chamber walls turned off (adiabatic operation). Figure 7.8 shows the in-cylinder temperature – equivalence ratio distributions at 30° BTC for an NVO timing of 30° (residual fraction of 0.16). As can be seen, without heat losses to the chamber walls, there is a linear relationship between the temperature and the equivalence ratio. Heat transfer to the walls both lowers the bulk temperature and leads to substantial deviations from the adiabatic temperature-equivalence ratio line. An important observation is that the spread of the equivalence ratio is roughly the same as for both cases. This spread is the due to incomplete mixing; this incomplete mixing leads to large temperature differences even without heat transfer. Note that in a perfectly mixed charge there would be no variation in the equivalence ratio and the temperature distribution would be entirely driven by heat transfer.

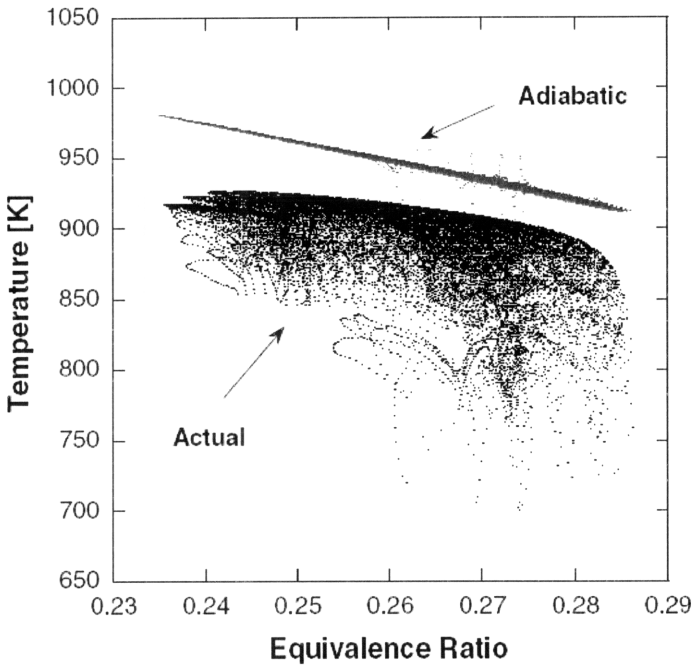

Figure 7.8: KIVA-3V generated in-cylinder temperature – equivalence ratio distributions at 30° BTC for an NVO timing of 30° (residual fraction of 0.16) [22]

7.2.3 Fuel Stratification

The effect of fuel stratification was examined for operation with and without a temperature gradient. As was observed by [23], fuel stratification of a gasoline type (single stage combustion) fuel has a reduced effect when applied to a thermally homogeneous charge. Fuel stratification more strongly affects the combustion process when coupled with thermal stratification. Figure 7.9 shows the three equivalence ratio profiles used. The quadratic temperature profile used for the thermally stratified simulations is also included in Figure 7.9. The overall ϕ was held constant for all three profiles with a value of 0.719.

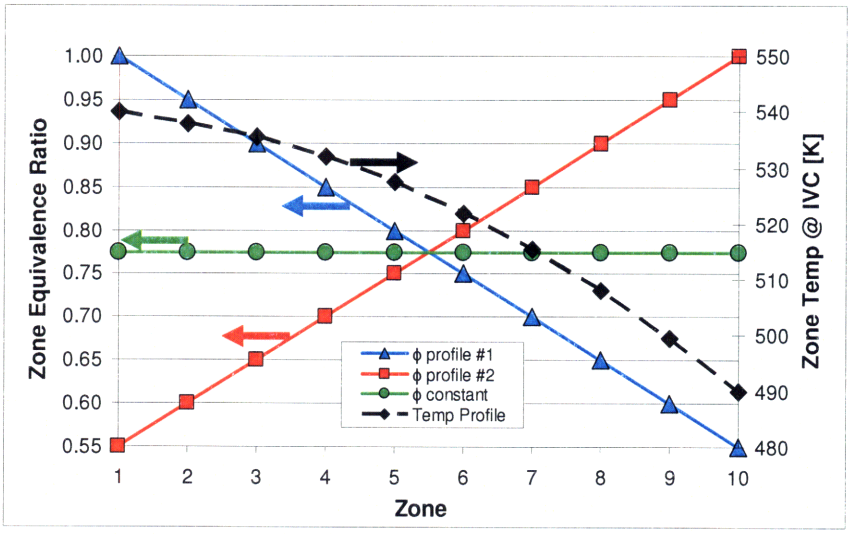

Figure 7.9: ϕ profiles used in fueling stratification study. The temperature profile used with the ϕ stratification simulations for which there was also thermal stratification.

Figure 7.10 shows the resulting pressure trace for ϕ profile #1 and constant ϕ in a charge with homogeneous temperature and burn fraction distribution.

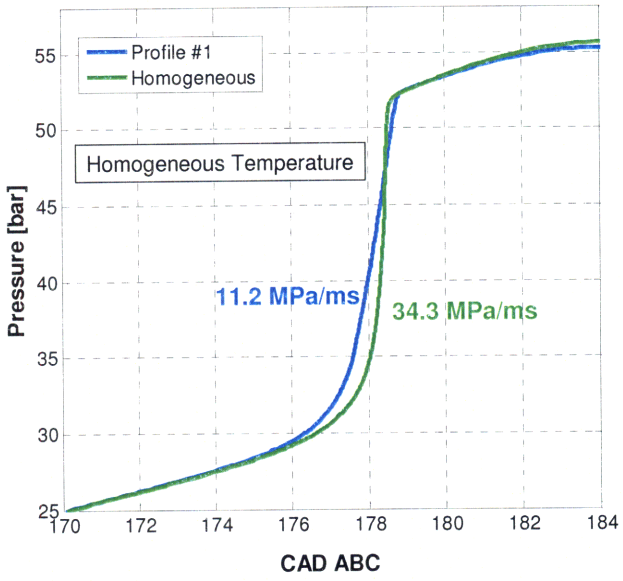

Figure 7.10: Effect of ϕ stratification for thermally homogeneous operation. T_{IVC} = 520.8 K; P_{IVC} = 1.5 bar; $\phi_{overall}$ = 0.719; χ_{burn} = .45

Figure 7.11 shows the pressure trace for the three ϕ profiles given in Figure 7.9 for operation with the temperature profile given in Figure 7.9. Increasing the fuel concentration in the direction of decreasing temperature (stratification profile #1 in Figure 7.9) increases the MPRR over the baseline homogeneous fueling. This results because the cooler regions have more fuel and ignite earlier and the hotter regions have less fuel and ignite later thus shortening the burn duration. Increasing the fuel concentration in the direction of increasing temperature (stratification profile #2 in Figure 7.9) reduces the MPRR over the baseline homogeneous fueling. This improvement results because the hotter regions have more fuel and ignite earlier and the cooler regions have less fuel and ignite later thus lengthening the burn duration.

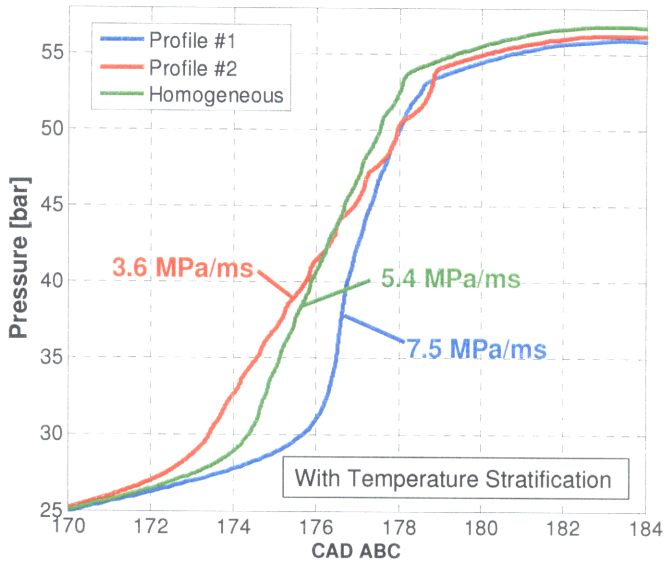

Figure 7.11: Effect of ϕ stratification for thermally stratified operation. The temperature profile used in these simulations is provided in Figure 7.9. P_{IVC} = 1.5 bar; $\phi_{overall}$ = 0.719; χ_{burn} = .45

In a practical HCCI engine thermal stratification will always be present due to heat transfer from the hot walls, mixing with hot residuals, and flow heating. Thus the reduced effect of fuel stratification in a thermally homogeneous charge is only of academic importance. Fuel stratification does affect combustion in a thermally stratified charge, with areas of high fuel concentration burning earlier and more quickly than areas of low fuel concentration. It is also important to understand that the fueling strategy can strongly influence the thermal stratification. This thermal effect is particularly strong for direct injection of liquid fuel because of the evaporative cooling that occurs.

8 Examination of Engine Data

8.1 Stoichiometric Operation without EGR: NVO Sweeps

As previously discussed, boosting has been proposed as a means to increase the HCCI high load limit. However the load increase provided by boosting comes at the expense of increased pressure rise rates. To more fully understand how boosting affects HCCI combustion, this section describes a set of NVO sweeps that were performed at intake pressures of 1.0, 1.1, 1.2 and 1.3 bar for stoichiometric fueling and without external EGR. In these sweeps the intake temperature was fixed at 120°C and the exhaust pressure was held equal to the intake pressure. Stoichiometric NVO sweeps were also performed at 60 and 90°C and had the same trends. Figures for these sweeps are provided in Appendix B.

The NIMEP as a function of the residual gas fraction is shown in Figure 8.1. As expected increases in the boost pressure provided increased NIMEP however it is important to examine how this boosting affects the pressure rise rate.

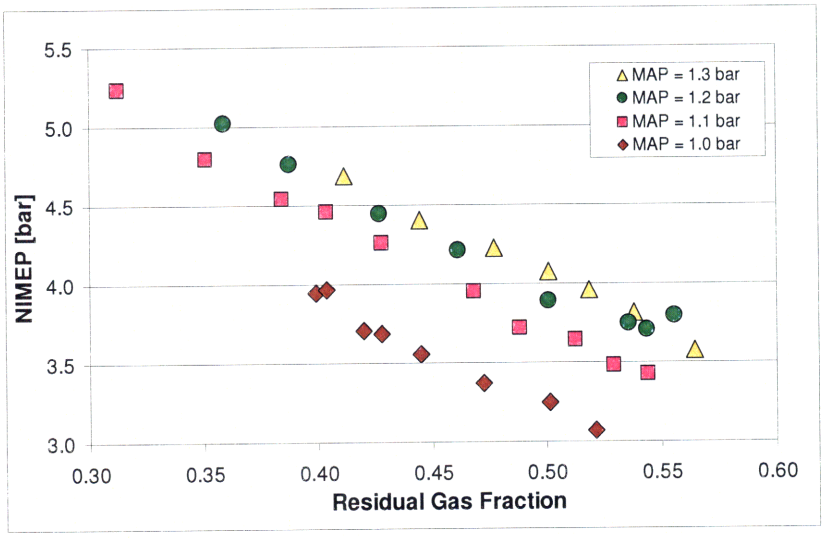

Figure 8.1: NIMEP versus the residual gas fraction for several boost levels. All points had stoichiometric fueling, no external EGR and an intake temperature of 120°C.

The intake temperature was fixed for all points and thus the combustion phasing varied between the points. The operating efficiency is strongly dependent on both the combustion phasing and burn duration and thus changes between operating points. Figure 8.2 provides the indicated efficiencies for each of the points. This changing efficiency affects the relative increase in

NIMEP associated with increased boost. This accounts for the small increase in NIMEP for going from 1.2 bar to 1.3 bar.

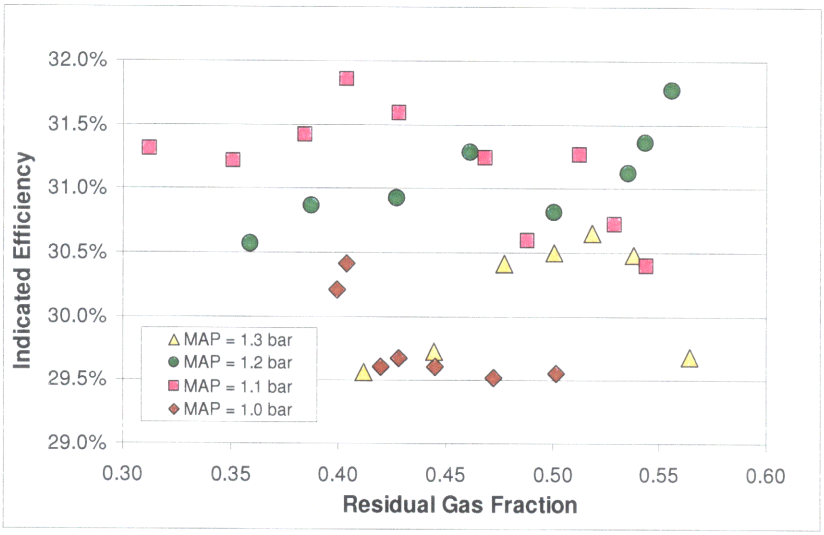

Figure 8.2: Indicated Efficiency versus the Residual Gas Fraction for several boost levels. All points had stoichiometric fueling, no external EGR and an intake temperature of 120°C.

The effect of efficiency can be removed by using the fuel mass instead of the NIMEP. Figure Figure 8.3 shows the fuel mass as a function of the burn gas fraction. Treating air and residual as ideal gases, increases in the pressure at IVC should provide proportional increases in the mass of fresh air (the effect of fuel is small). However in this low valve lift engine operating with significant negative overlap, pumping losses limit the flow of fresh charge into the engine. Consider the two circled points in Figure 8.3 which both have a burn fraction of 0.44, an increase in boost pressure from 1.0 bar to 1.3 bar (30% increase) provides an increase in fuel mass (directly proportional to air mass) of only 22%.

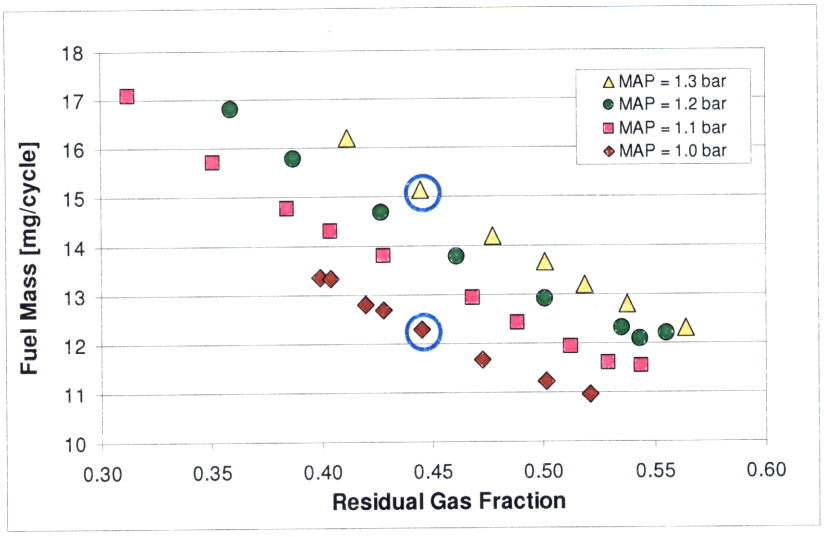

Figure 8.3: Fuel mass versus the Residual Gas Fraction for several boost levels. All points had stoichiometric fueling, no external EGR and an intake temperature of 120°C.

While increasing the boost pressure does provide increases in load, it also leads to increases in the MPRR as shown in Figure 8.4. Furthermore the relative increase in MPRR is greater than the relative increase in load. This is demonstrated by Figure 8.5 which plots the MPRR as function of the fuel mass. For a given fueling, operating at the lowest pressure will provide the lowest MPRR.

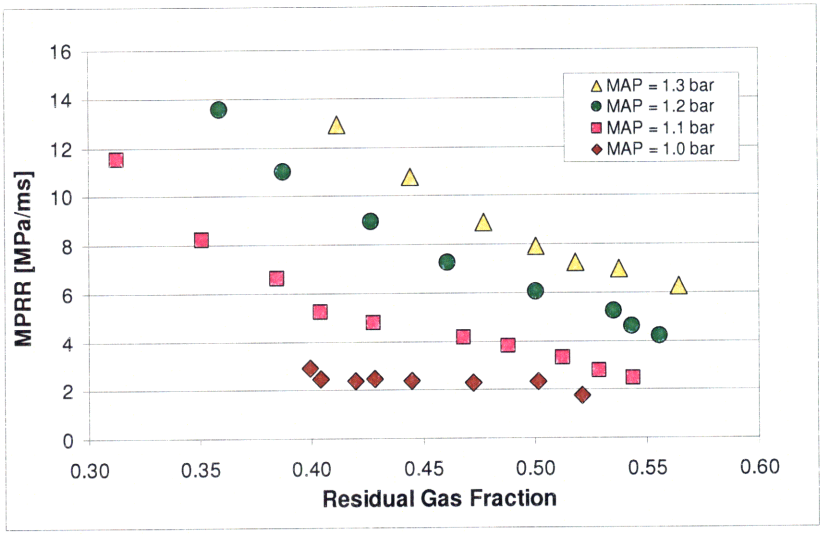

Figure 8.4: MPRR versus the Residual Gas Fraction for several boost levels. All points had stoichiometric fueling, no external EGR and an intake temperature of 120°C.

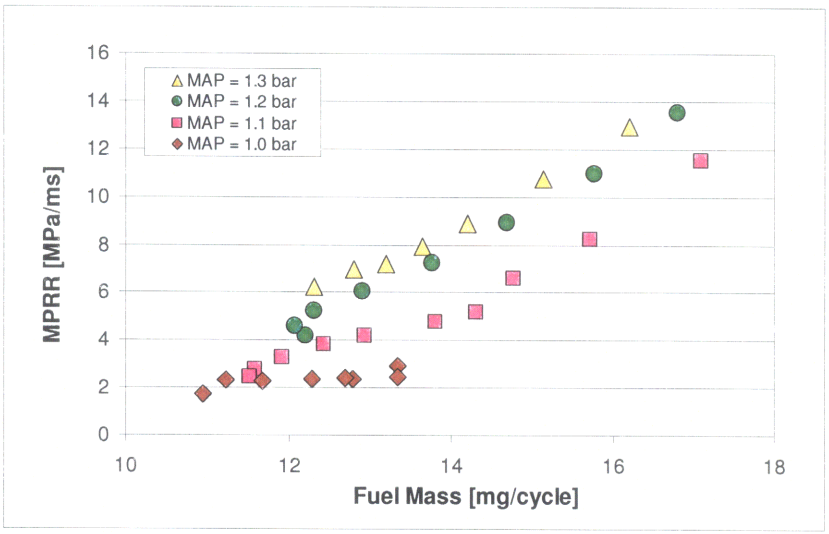

Figure 8.5: MPRR versus the fuel mass for several boost levels. All points had stoichiometric fueling, no external EGR and an intake temperature of 120°C.

Equation (5.10) from Section 5 is stated again as it is useful in understanding the MPRR trends:

$$MPRR = \frac{1}{BD_{10-90}} \cdot \frac{(\gamma - 1) \cdot m_{fuel} \cdot LHV}{V_{CA50}} \tag{8.1}$$

To increase fueling (and thus load) while controlling the MPRR, the potential parameters to control are $BD_{10\text{-}90}$, V_{CA50}, and γ. However as previously discussed the burn duration is the only parameter the can be substantially changed.

The CA50 is plotted as a function of the burn gas fraction in Figure 8.6. Note that while not shown, the trends for CA50 are nearly identical to those for CA10. CA50 shows a strong dependence on pressure, with combustion advancing for higher pressures. This advancing of the combustion phasing results from the pressure term in the ignition delay.

Somewhat surprisingly the CA50 timing was relatively independent of the residual gas fraction. As the residual fraction increases, the oxygen fraction is reduced. The charge temperature also changes with residual fraction and Figure 8.7 shows estimated temperature 15° BTC as a function of the residual fraction. For 1.1 and 1.2 bar, CA50 retards slightly as the residual fraction is increased above 0.50. This is attributed to be the drop in T_{15BTC} however this effect is not seen for 1.3 bar. For 1.0 bar, CA50 advances with increasing burn fraction and this can not be explained with T_{15BTC} or oxygen fraction. One possible explanation for these trends is that the effects of reduced oxygen concentration are offset by the increased thermal stratification that can

occur with increased residual trapping and for 1.0 bar the effect of thermal stratification dominates. Another possibility is that the T_{15BTC} estimates are inaccurate and the temperature does not start to decrease until a higher $x_{residual}$ value. In this scenario the effect of increasing temperature offsets the effect of decreasing oxygen concentration. Without more accurate temperature values and thermal stratification information, interpreting the CA50 trends in Figure 8.6 is difficult.

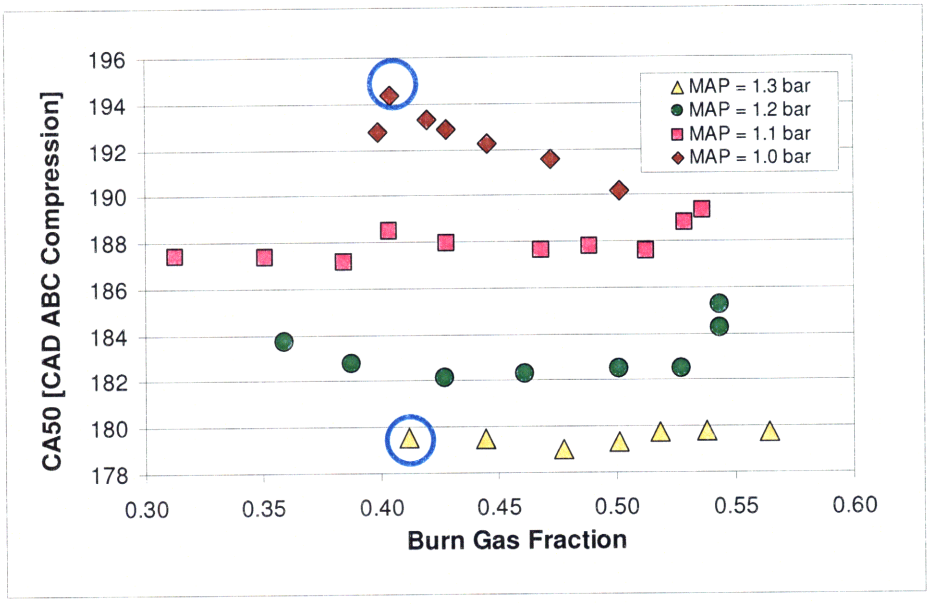

Figure 8.6: CA50 as a function of the Burn Gas Fraction for several boost levels. All points had stoichiometric fueling, no external EGR and an intake temperature of 120°C.

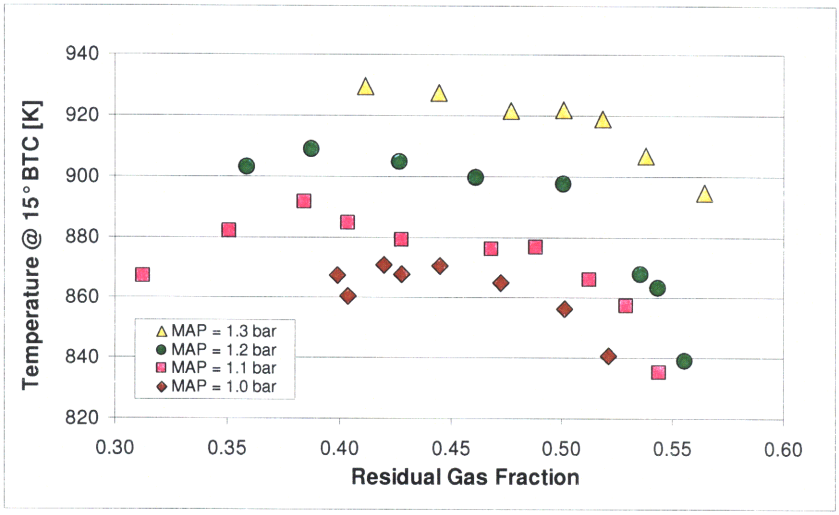

Figure 8.7: Temperature at 15° BTC versus the Burn Gas Fraction. for several boost levels. All 5points had stoichiometric fueling, no external EGR and an intake temperature of 120°C.

Figure 8.8 provides the cylinder volume at CA50 as a function of the burn gas fraction. The increase in volume between the most advanced point and the most retarded point is only 18.5% (these points are circled). However the MPRR/m_{fuel} increases by 421% for these two points. Clearly the V_{CA50} term does not account for the change in MPRR.

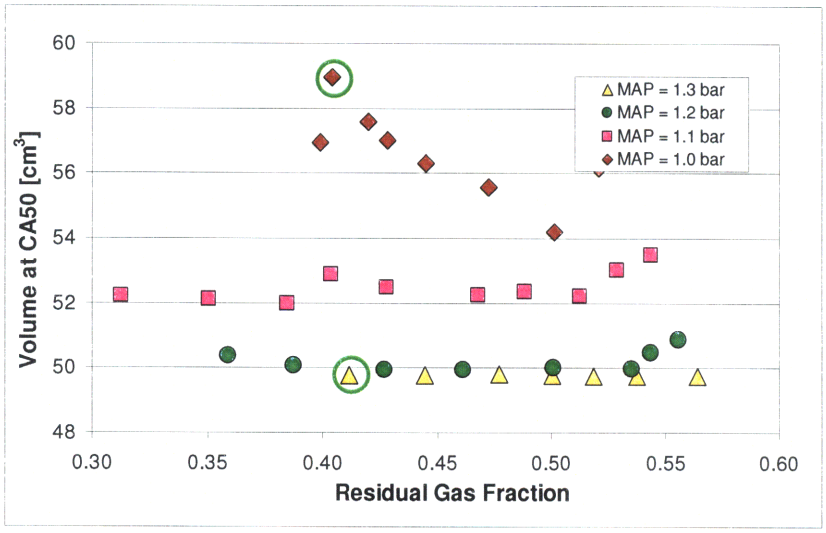

Figure 8.8: V_{CA50} versus the Residual Gas Fraction for several boost levels. All points had stoichiometric fueling, no external EGR and an intake temperature of 120°C.

The large changes in MPRR can be captured by the burn duration. Figure 8.9 shows the burn duration as a function of the residual gas fraction. As shown by Figure 8.9, increasing the boost level provides large decreases in the burn duration. Also notice that increasing the residual

fraction lengthens the burn duration. With increasing residual dilution, the oxygen concentration falls leading to extended burn duration. Furthermore with increased residual fraction, the inert residual absorbs energy from the combusting charge which helps slow the reaction rate.

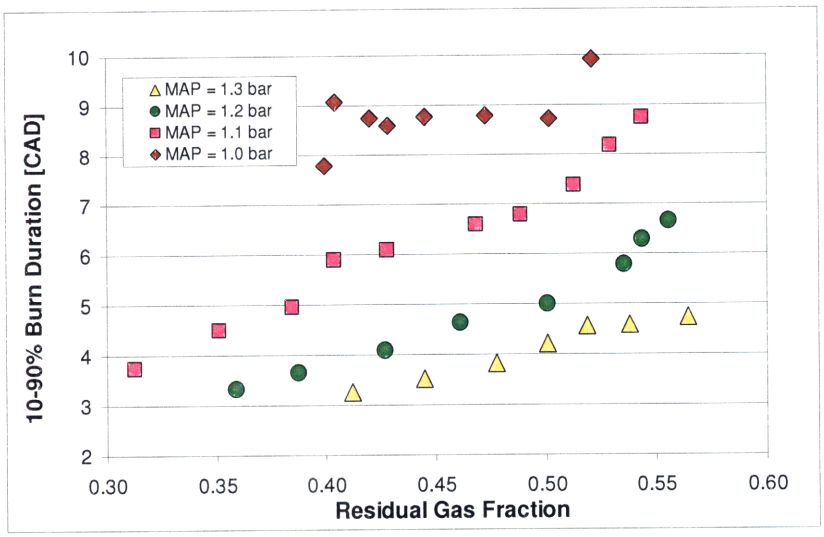

Figure 8.9: 10-90% Burn Duration versus the Burn Gas Fraction for several boost levels. All points had stoichiometric fueling, no external EGR and an intake temperature of 120°C.

The MPRR/m_{fuel} is plotted as a function of the 10-90% burn duration in Figure 8.10. The burn duration clearly accounts for the changes in MPRR/m_{fuel}. As was previously shown in Section 5, the burn duration closely approximates $\tau_{reaction}$, which is defined by equation (5.11). The opportunity for extending the high load limit is to lengthen the burn duration and thus $\tau_{reaction}$. A major part of this study is to understand the parameters that control $\tau_{reaction}$.

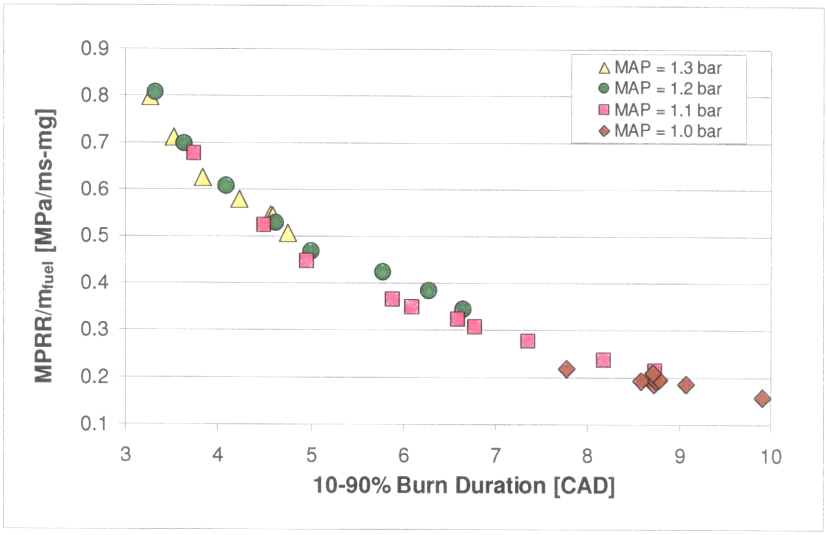

Figure 8.10: MPRR/m_{fuel} as a function of the 10-90% Burn Duration for several boost levels. All points had stoichiometric fueling, no external EGR and an intake temperature of 120°C.

In these NVO sweeps the intake temperature was fixed at 120°C and the combustion phasing was allowed to assume any value. In a real-world engine the combustion phasing will be more tightly controlled so as to optimize efficiency. With increased boost pressure, combustion phasing advances thus providing an opportunity to lower the intake temperature to maintain constant CA50 timing. The question is, does reducing the temperature to maintain a constant CA50 timing lengthen the burn duration by enough to offset the effects of increased pressure? This is explored in Section 12.

8.2 Stoichiometric Operation without EGR: Temperature Sweeps

Temperature sweeps were performed at intake pressures of 1.0, 1.1, 1.2, 1.3 and 1.4 bar while holding the NVO timing constant at 82° BTC. Stoichiometric fueling was used and the engine was operated without external EGR. These temperature sweeps were used to directly examine how temperature affects the MPRR.

Figure 8.11 shows the estimated in-cylinder bulk temperature at 15° BTC as a function of the intake temperature. The estimated T_{15BTC} increases essentially linearly with the intake temperature and the slope is roughly equivalent for the different boost pressures with a dT_{15BTC}/dT_{intake} value of approximate 0.5 °C/°C. This T_{15BTC} increase of 5°C for every 10°C increase of T_{intake} makes sense as the trapped gas fraction ranged between 40 and 46% as shown in Figure 8.12. For operation at 1.0, 1.1 and 1.2 bar boost, a misfire limit was reached as the

intake temperature was reduced; the circled points in Figure 8.11 denote this misfire limit. A misfire limit was not reached for 1.3 and 1.4 bar boost as the intake temperature could not be brought low enough. The low temperature points for 1.3 and 1.4 bar represent the lowest intake temperature achievable with the test system.

Also note that for a given intake temperature, T_{15BTC} increases with boost pressure. This results because fueling increases with boost pressure and the increased chemical energy released leads to higher engine surface temperatures. The increased surface temperatures reduce the heat loss from the mixture during the compression process.

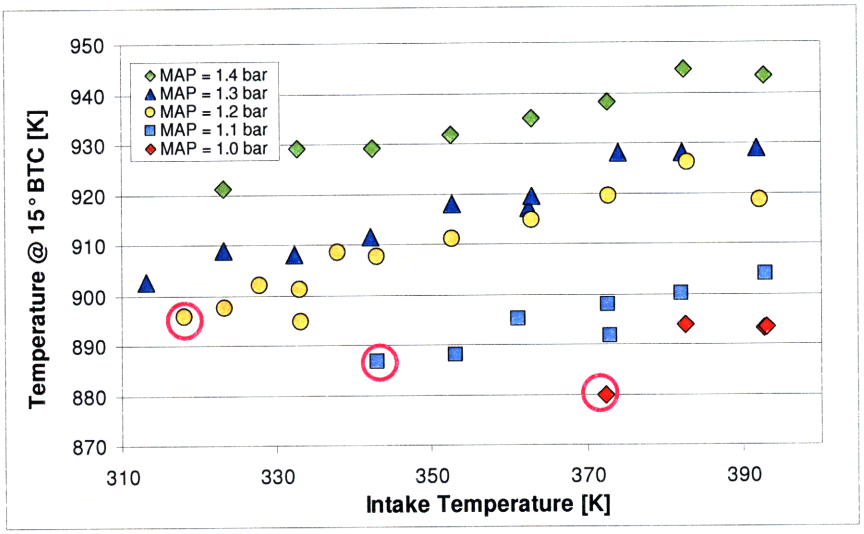

Figure 8.11: Estimated in-cylinder temperature at 10° BTC versus the Intake Temperature. Fixed NVO timing and $\lambda = 1$. The misfire limit points are circled.

Figure 8.12 shows that for a given boost pressure the burn gas fraction increases with intake temperature. This results because with increasing intake temperature, the density of the fresh charge (air and fuel) decreases by a larger percentage than the residual gas. Thus the relative amount of burned gas to fresh charge increases with increasing intake temperature. Also notice that increases in boost pressure lead to increases in the residual fraction. This occurs because this engine utilizes short lift valves with significant negative valve overlap, and as boost pressure increases it becomes more difficult to purge the larger quantity of burned gasses from the cylinder. Thus the ratio of residual gas to fresh charge increases.

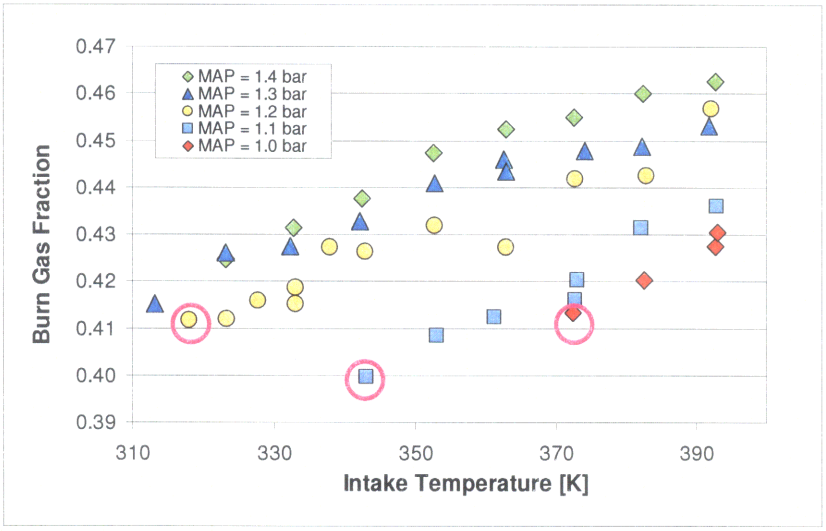

Figure 8.12: Residual Fraction versus the Intake Temperature. Fixed NVO timing and $\lambda = 1$. Misfire limit points are circled.

The effect of intake temperature on the MPRR is shown in Figure 8.13. For a given intake temperature, increasing the boost pressure leads to in increases in the MPRR. Note that with the exception of the 1.4 bar data, reducing the intake temperature provides significant reductions in the MPRR. These MPRR trends are explained shortly.

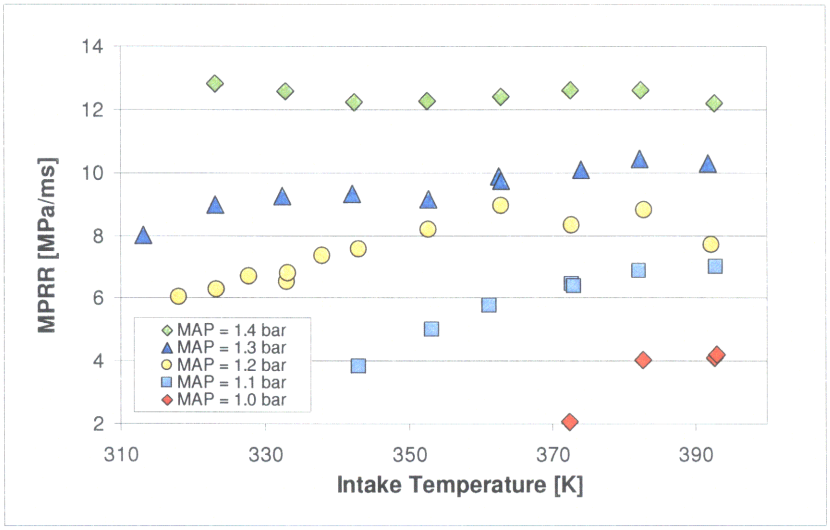

Figure 8.13: MPRR as a function of the Intake Temp. Fixed NVO timing and $\lambda = 1$.

Figure 8.14 shows the MPRR as a function of the fuel mass. For a given fuel mass the MPRR increases with boost pressure. Notice that for a given boost pressure, the highest fueling and lowest MPRR occur at the lowest possible temperature.

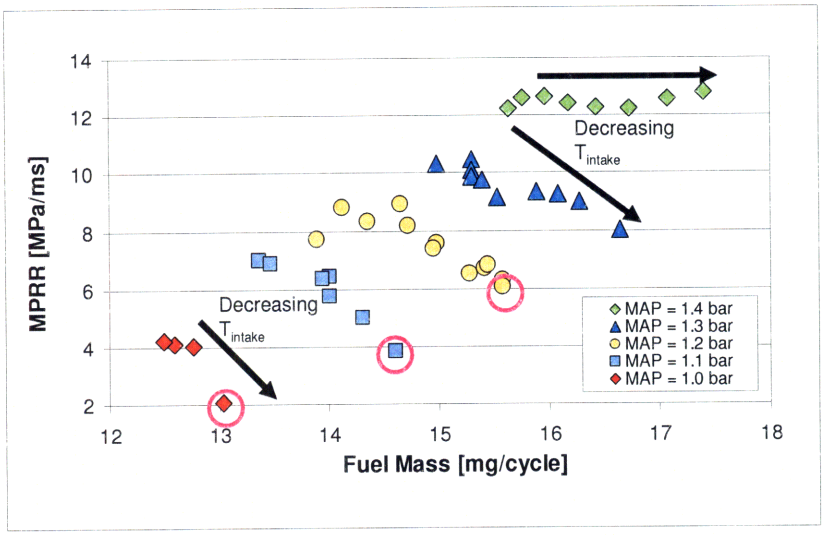

Figure 8.14: MPRR versus the Fuel Mass. Fixed NVO timing and $\lambda = 1$. Misfire points circled.

To better understand the MPRR trends shown in Figure 8.13, the CA50 and 10-90% burn duration as a function of the intake temperature are provided in Figure 8.15 and Figure 8.16 respectively.

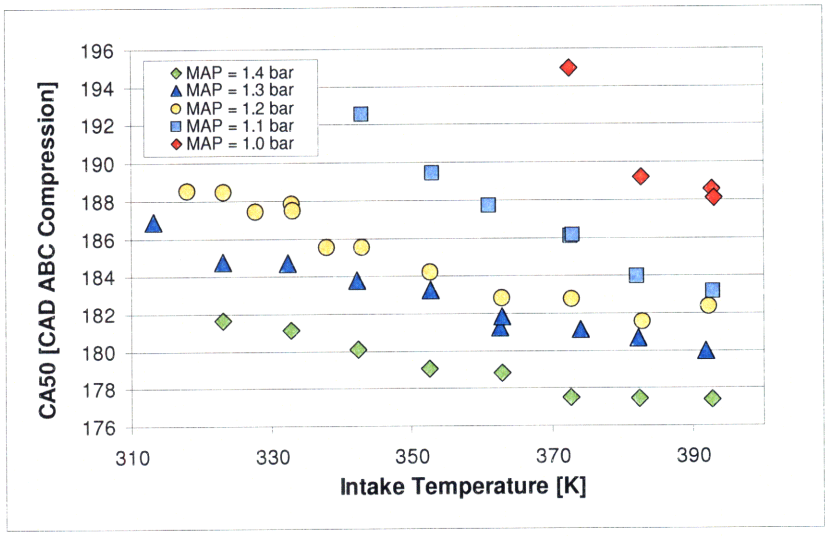

Figure 8.15: CA50 versus Intake Temperature. Fixed NVO timing and $\lambda = 1$.

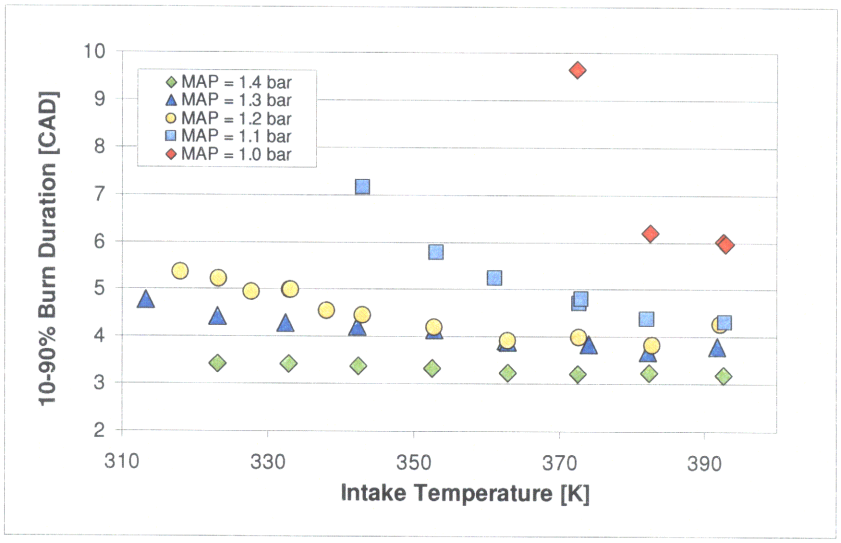

Figure 8.16: 10-90% Burn Duration versus Intake Temperature. Fixed NVO timing and $\lambda = 1$.

The CA50 captures effects from both the combustion phasing and the burn duration. The CA10 better represents the start of combustion (SOC). Figure 8.17 shows the CA10 as a function of the intake temperature. The CA10 timing is presented rather than the SOC timing because the SOC was affected by electrical noise on the pressure signal. Notice that slopes of the CA10 and CA50 curves differ more as the intake pressure is reduced. This results because for these points, the burn duration dependence on intake temperature increases with decreasing boost pressure; this is explained below.

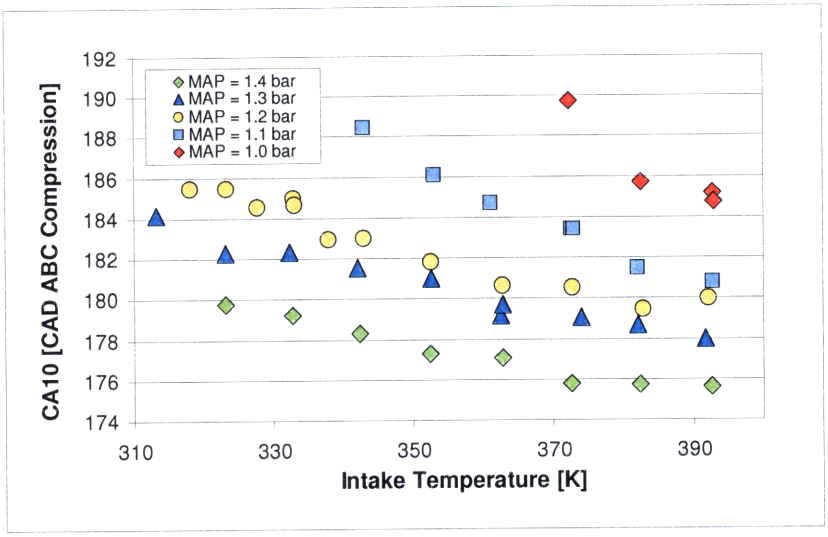

Figure 8.17: CA10 vs. Intake Temp. Fixed NVO timing and $\lambda = 1$.

The CA10 curves can be explained using the ignition delay equation. For a given boost pressure, equivalence ratio and oxygen fraction, increasing the charge temperature prior to ignition leads to an exponential reduction of the ignition delay. To demonstrate this, Figure 8.18 shows the iso-octane ignition delay plotted as a function of temperature for two different pressures using the ignition delay correlation developed by He et al. [9] which was discussed in Section 7.1. While the ignition delay for iso-octane will be different from that of UTG-91, the trends exhibited are useful in understanding what is happening. In Figure 8.18, the oxygen fraction and equivalence ratio are fixed at 11.5% and 1.0 respectively. The pressures of 15.0 and 19.5 bar correspond to the average pressure 15° BTC for the temperature sweep data at 1.1 bar and 1.4 bar respectively. Note that in these temperature sweeps, the pressure 15° BTC is essentially constant for each boost pressure and does not change with intake temperature.

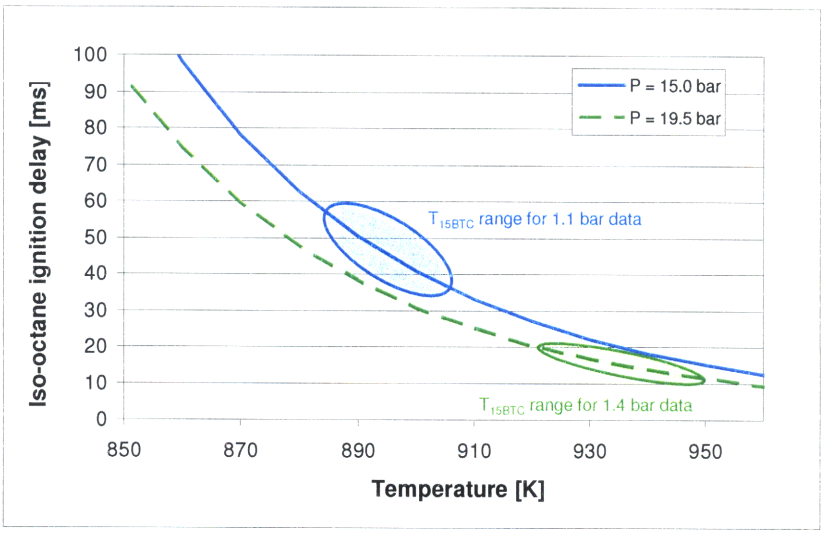

Figure 8.18: Iso-octane ignition delay as a function of temperature. χ_{O2} = 11% and ϕ = 1.00.

There are several important observations to make from Figure 8.18. First, operating at higher pressure shifts the ignition delay curve downward and flattens the slope. This partially accounts for the flattening of the CA10 lines that occurs for increased boost pressure. Additionally, as Figure 8.11 showed, for a given intake temperature, operating at higher pressure increases T_{15BTC}. This has the effect of shifting the range of T_{15BTC} values upward for increasing boost levels; the T_{15BTC} range is indicated for 1.1 and 1.4 bar boost. The slope of the ignition delay curve decreases with increasing temperature. Thus the shift in T_{15BTC} that results from increased boost also partially explains the flattening of the CA10 lines with higher boost levels.

The ignition delay for iso-octane was computed using T_{15BTC}, P_{15BTC}, χ_{O2} and ϕ from the temperature sweep data and is plotted in Figure 8.19 as a function of the intake temperature. The flattening of the ignition delay curves with pressure is clearly evident going from 1.2 to 1.3 to 1.4 bar.

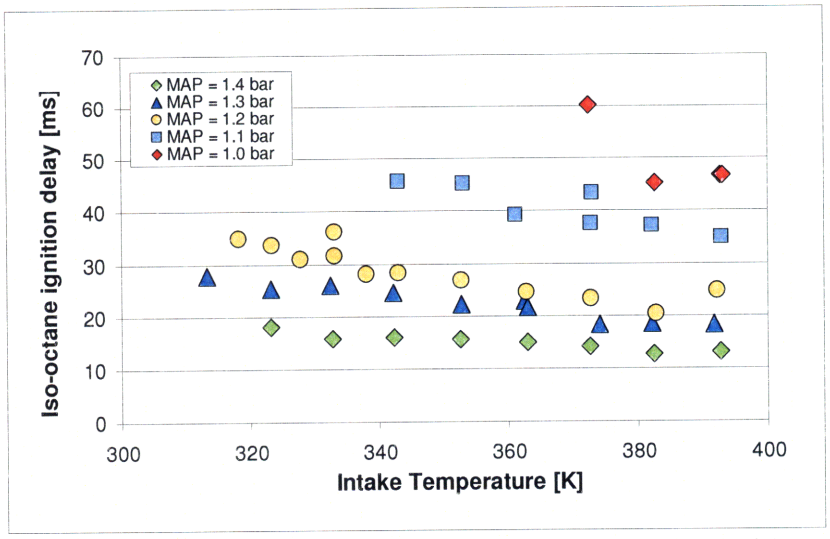

Figure 8.19: Iso-octane ignition delay computed with T_{15BTC}, P_{15BTC}, χ_{O2} and ϕ in Equation (7.2)

Now that the CA10 trends have been explained, the trends in the 10-90% burn duration are explored. As Figure 8.16 shows, with increasing intake temperature the burn duration decreases and the slope decreases with increasing temperature. Furthermore with increasing pressure these burn duration curves become more flat, with the curve for 1.4 bar showing only a slight decline with increasing temperature. This flattening of the curves with increasing boost pressure is consistent with the CA10 curves however the flattening effect with increased boost pressure is stronger for the burn duration curves. This can be explained by revisiting the relationship between combustion phasing and burn duration that was discussed in Section 7.1.1.

As described in Section 7.1.1, the HCCI combustion process can be thought of as consisting of the sequential ignition of parcels, with the earliest igniting parceling having the shortest ignition delay and the latest igniting parcels having the longest ignition delay. Holding stratification constant, increasing in the bulk temperature, pressure, oxygen fraction, or fueling will reduce the ignition delay for both the earliest parcel and the latest parcel. For this to produce a reduction in the total burn duration, ignition of the latest parcel needs to advance by more than the earliest parcel. This generally occurs because with earlier phasing the later burning parcels will be at a higher pressure because the volume will be smaller. This is equivalent to saying the pressure rise rate will be increase with advanced combustion. This breaks down if the combustion is significantly advanced and the latest parcels are igniting before top center.

In these temperature sweeps the residual fraction was relatively constant and the stratification can be assumed to be roughly constant. As the boost pressure was increased the effect of the intake temperature on the CA10 and CA50 timing was reduced (CA10 and CA50 curves flatten with increased pressure). Additionally with increased pressure the combustion timing advances closer to top center. As result, the decrease in volume at CA50 with increases in intake temperature becomes very small as boost pressure increased. This is shown in Figure 8.20.

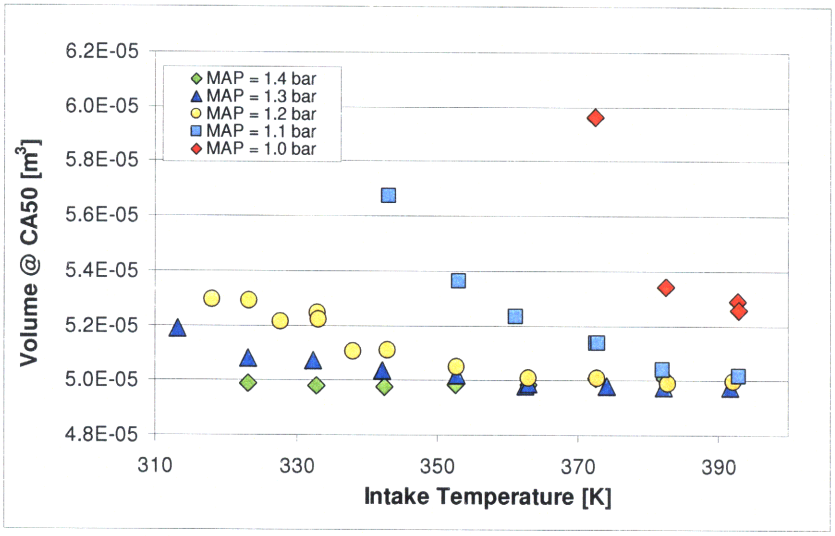

Figure 8.20: Volume at CA50 versus intake temperature.

Because the volume at CA50 is essentially constant for 1.4 bar, the burn duration does not decrease with advances in phasing for these points. This is because the pressure for the later burning parcels does not increase. This can be seen by plotting the 10-90% burn duration as a function of the CA50 timing as shown in Figure 8.21. As the stratification and oxygen fraction were roughly constant, the temperature sweep points collapse on a single curve and the relationship between CA50 and burn duration is relatively clear. Notice that as the CA50 retards, the slope of the line increases. The points from the stoichiometric NVO sweeps discussed in Section 8.1 are also shown for comparison. As the residual fraction changed for these NVO sweeps there is not a clear trend.

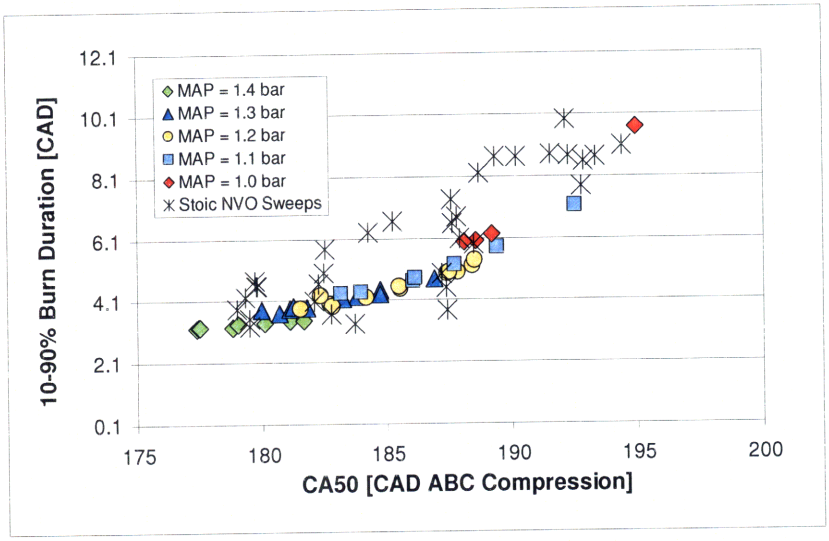

Figure 8.21: 10-90% Burn Duration versus CA50. Temperature sweeps with fixed NVO timing and stoichiometric fueling. Data from the stoichiometric NVO sweeps is also shown.

Lastly it is important to note that as Figure 8.22 shows, $MPRR/m_{fuel}$ is captured by the burn duration.

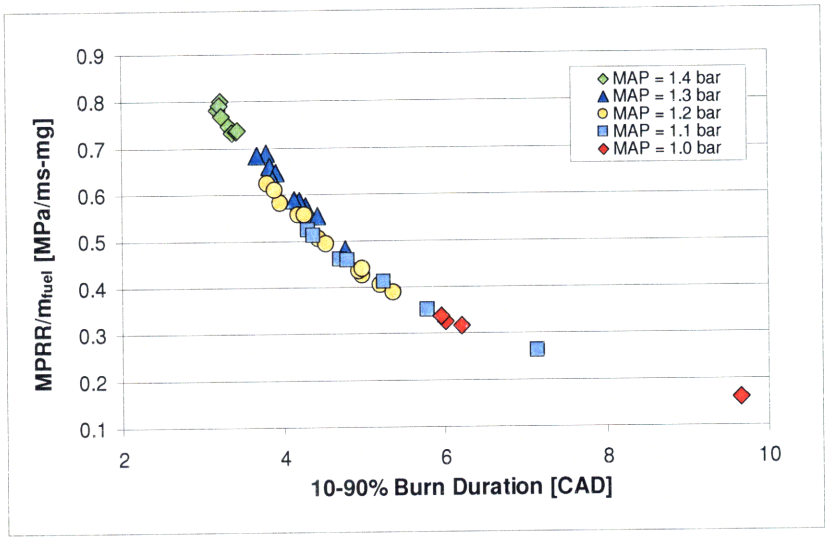

Figure 8.22: $MPRR/m_{fuel}$ versus 10-90% Burn Duration. Fixed NVO timing and stoichiometric fueling

8.3 Operation with EGR and excess air: NVO Sweeps

The effect of dilution with external EGR and excess air is examined in this section. NVO sweeps were performed for a range of dilution levels and boost pressures. This section explores

data for 10% dilution at a boost pressure 1.3 bar and a intake temperature of 120°C. Appendix C provides plots for 10 and 15% dilution for 1.5 bar.

To enable comparison between the different diluents, the total dilution ratio is defined as the ratio of the moles of stoichiometric EGR, trapped residual and excess air divided by the total number of moles:

$$x_{dilution} = \frac{n_{EGR} + n_{burn} + n_{excess\ air}}{n_{total}} \tag{8.2}$$

Figure 8.23 shows the estimated charge temperature at 15° BTC. Operating with 10% excess air or 10% EGR both provide reduced mixture temperatures as hot trapped residual is replaced with cool EGR or excess air. However EGR operation provides a larger temperature reduction. This larger temperature reduction results because the EGR has a larger specific heat ratio (gamma) and thus the temperature rise with compression is smaller compared to 10% excess air.

It is important to understand that in these tests the excess air and EGR dilution were maintained at 10% of the fresh charge. With increasing trapped residual (increasing total dilution) the fraction of fresh charge was reduced thus reducing the quantity of diluent. As a result, the ratio of diluent (EGR or excess air) to trapped residual gas decreased with increasing residual fraction. Thus as the total dilution increases, the observed temperature reduction diminishes for both EGR and lean operation.

For all three curves, the temperature initially increases as the total dilution increases. This occurs because more hot residual is trapped. Eventually further increases in dilution (residual fraction) lead to reduced mixture temperature because the effect of reduced residual gas temperature outweighs the effect of trapping more residual.

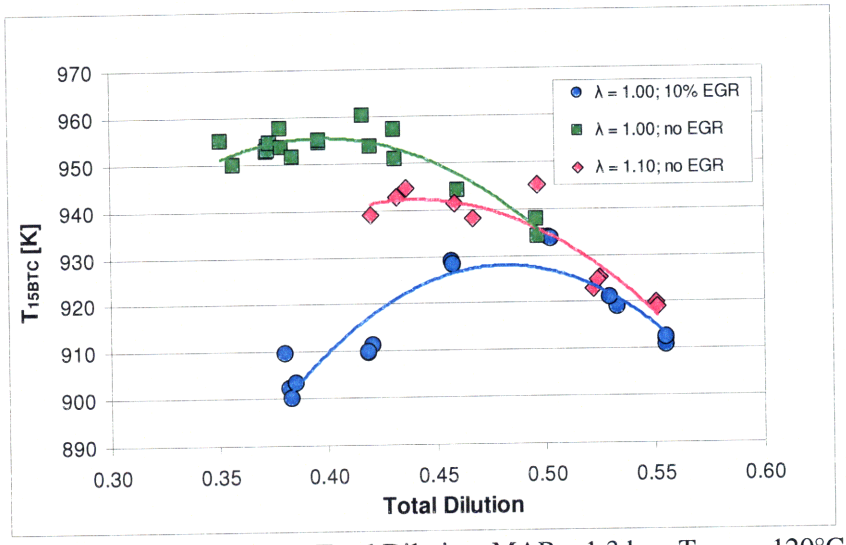

Figure 8.23: T_{15BTC} versus Total Dilution. MAP = 1.3 bar; T_{intake} = 120°C

The NIMEP as a function of the total dilution is shown in Figure 8.24. For a given dilution, utilizing EGR produces a higher NIMEP than either stoichiometric operation without EGR or operation with excess air. Lean operation provides a slightly higher output than stoichiometric operation without EGR. These differences in NIMEP are due to differences in indicated efficiency that result from changes in the combustion phasing and duration as well as improved breathing with the cooler diluent.

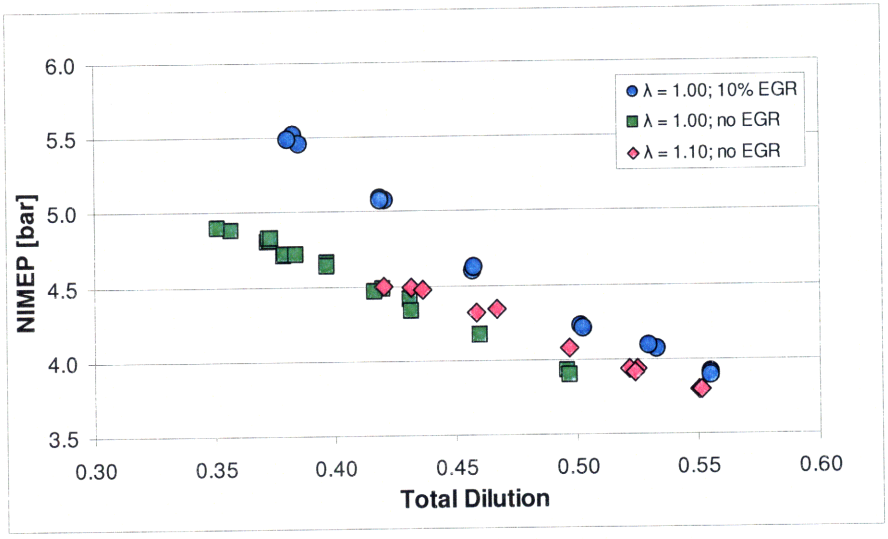

Figure 8.24: NIMEP versus Total Dilution. MAP = 1.3 bar; T_{intake} = 120°C

The effect of efficiency can be removed by plotting the fuel mass instead of the NIMEP. Figure 8.25 shows the fuel mass as a function of the total dilution. Note that for a given total dilution, the fuel mass is slightly larger for operation with EGR or excess air. This breathing benefit occurs because the EGR and excess air are more dense than the hot burned gas they are replacing. Thus the volume consumed by diluent is reduced, enabling the quantity of non-diluent fresh charge to be increased. Note this breathing benefit is reduced as the total dilution increases and the diluent becomes a smaller fraction of the charge.

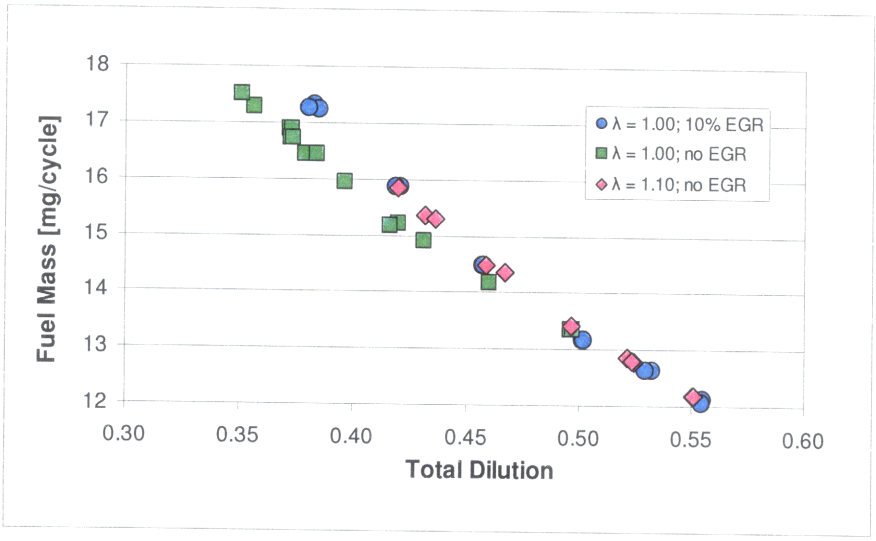

Figure 8.25: Fuel Mass vs. Total Dilution. MAP = 1.3 bar; T_{intake} = 120°C

The MPPR as a function of the total dilution is provided in Figure 8.26. For a given total dilution, operation with 10% EGR provides the lowest MPRR. Operating with 10% excess air leads to an increase in MPRR. As Figure 8.25 showed, the fuel mass at a given dilution is roughly the same for the all three dilution methods thus EGR provides the lowest MPRR for a given fuel mass. This is shown in Figure 8.27.

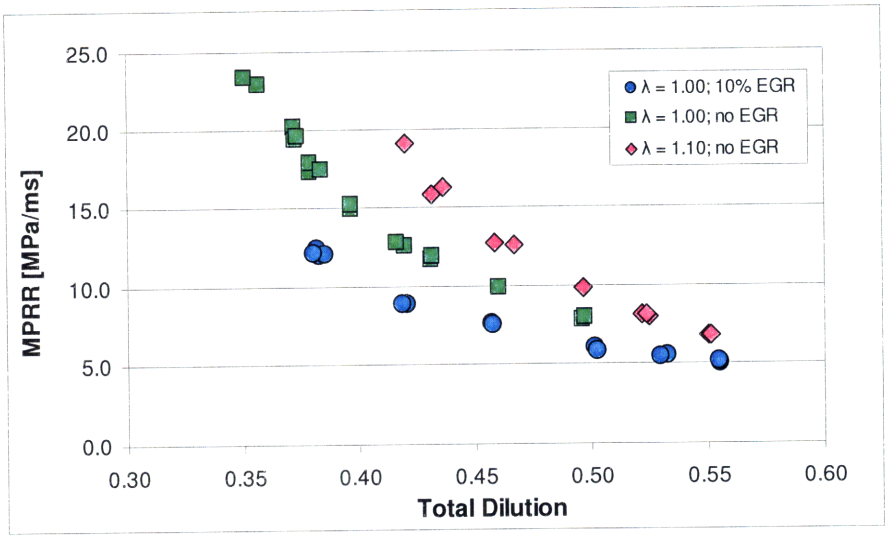

Figure 8.26: MPRR versus Total Dilution. MAP = 1.3 bar; T_{intake} = 120°C

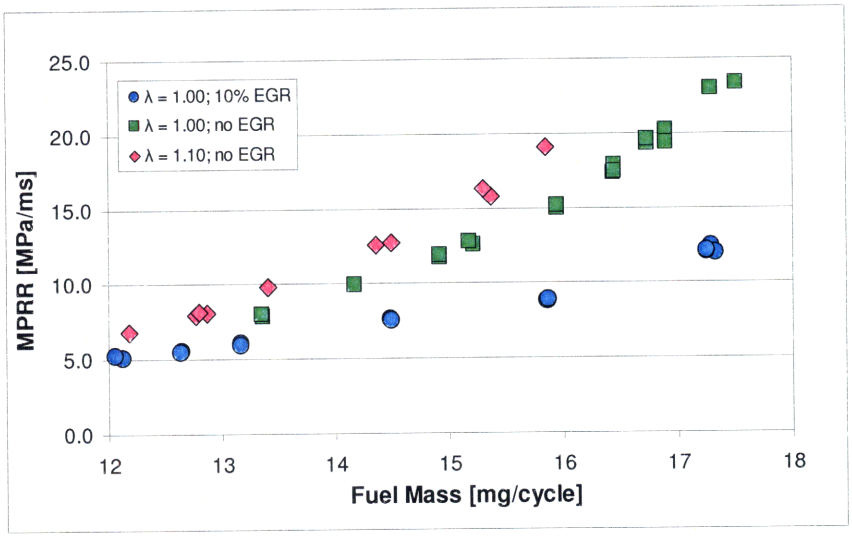

Figure 8.27: MPRR versus Fuel Mass. MAP = 1.3 bar; T_{intake} = 120°C

To explain these MPRR trends, the 10-90% burn duration as a function of the total dilution is provided in Figure 8.28. For a given dilution, operation with 10% EGR provides the longest burn duration and operation with 10% excess air provides the shortest burn duration. For operation with EGR the lengthening of the combustion duration is due to the reduction in mixture temperature. For a given dilution the composition is the same and the thermal stratification is assumed to be roughly the same. The shortening of the combustion duration with excess air is attributed to the increased oxygen in the mixture. This increased oxygen concentration appear to override the temperature reduction that the fresh excess air provides.

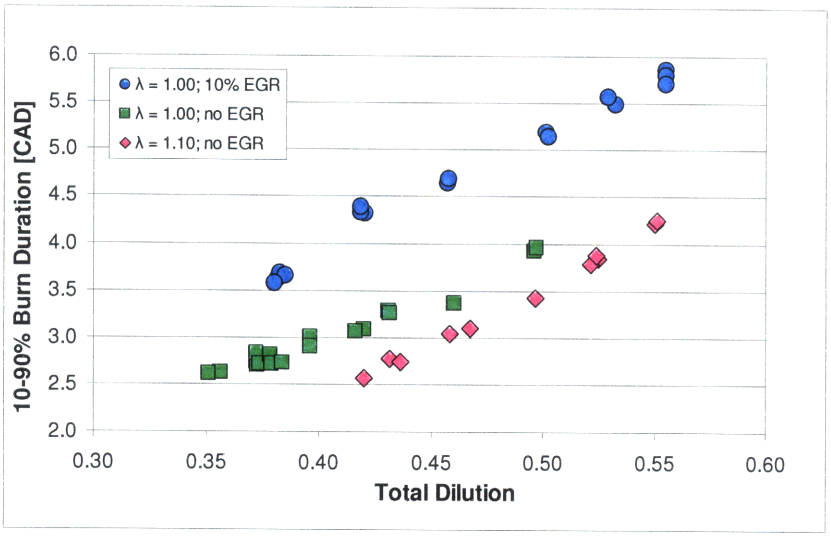

Figure 8.28: 10-90% Burn Duration versus Total Dilution. MAP = 1.3 bar; T_{intake} = 120°C

Figure 8.29 shows the CA50 as a function of the total dilution. The timing is significantly retarded for the EGR curve relative to the lean and no EGR curves. This results from the temperature reduction provided by EGR. Notice that as the total dilution increases, the EGR CA50 timing advances. This is somewhat surprising as the estimated mixture temperature shown in Figure 8.23 begins to decrease at a total dilution of around 0.5 and thus can not explain this trend. This trend is also inconsistent with the burn duration, which increases as the total dilution increases. One possibility is that the thermal stratification is increasing and this both lengthens the burn duration and advances the phasing.

The increased oxygen concentration is thought to override the effect reduced temperature for operation with 10% excess leading to combustion phasing that slightly advanced from the stoichiometric no EGR curve. Also note that the combustion phasing does not change with total dilution for the lean and stoichiometric (without EGR) curves. This is consistent with the results presented in Section 8.1. This insensitivity to increases in residual fraction must be the result of a balance between the effects of temperature, oxygen fraction and stratification.

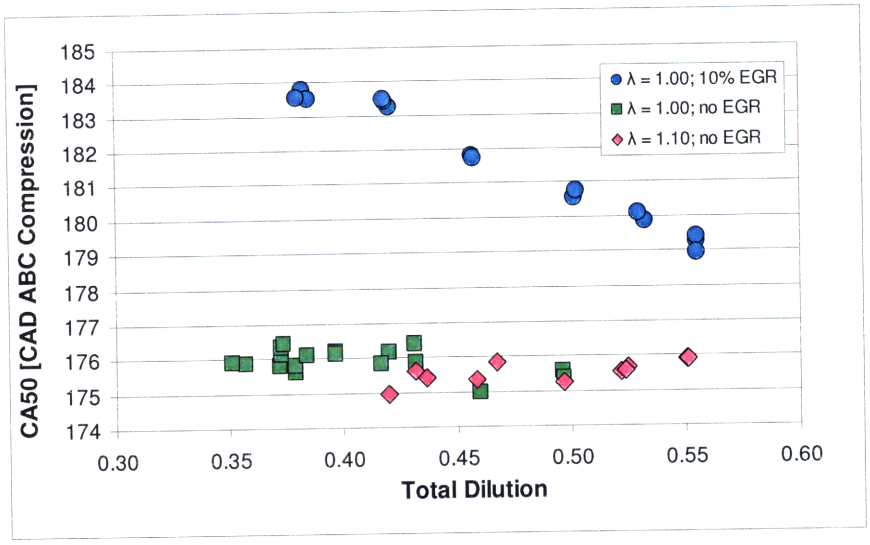

Figure 8.29: CA50 versus Total Dilution. MAP = 1.3 bar; T_{intake} = 120°C

Figure 8.30 shows that the fuel normalized MPRR is fully captured by the burn duration. This is consistent with the previous sections and again indicates that the burn duration is the metric to focus on for reducing the MPRR.

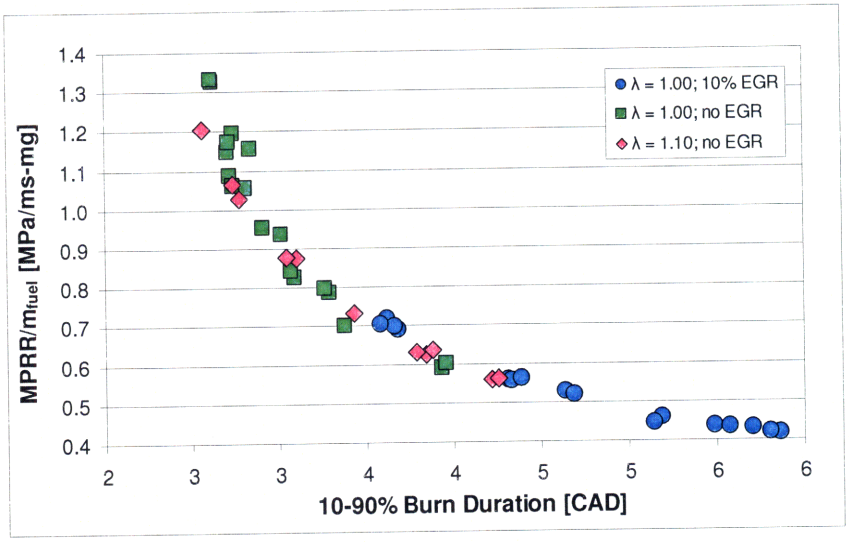

Figure 8.30: MPRR/m_{fuel} vs. 10-90% Burn Duration. MAP = 1.3 bar; T_{intake} = 393K

9 Understanding the HCCI Operating Region

The HCCI operating region and high load limit are discussed in this section. Specifically the relationship between the load and maximum pressure rise rate was examined for changes in oxygen fraction and boost pressure. Figure 9.1 shows the MPRR and NIMEP contours on a plot of x_{O2} versus MAP for stoichiometric operation without EGR. The MPRR and NIMEP contours were obtained from interpolation of data points using the 'griddata' function in MatLab.

In generating these contour maps, the NIMEP contours were calculated from the fuel mass using an indicated efficiency 33%. The actual measured NIMEP values produced the same trends but were less smooth due to changes in efficiency. The smoother contour lines provided by the fixed efficiency NIMEP allowed the important features of the plots to be more clearly shown.

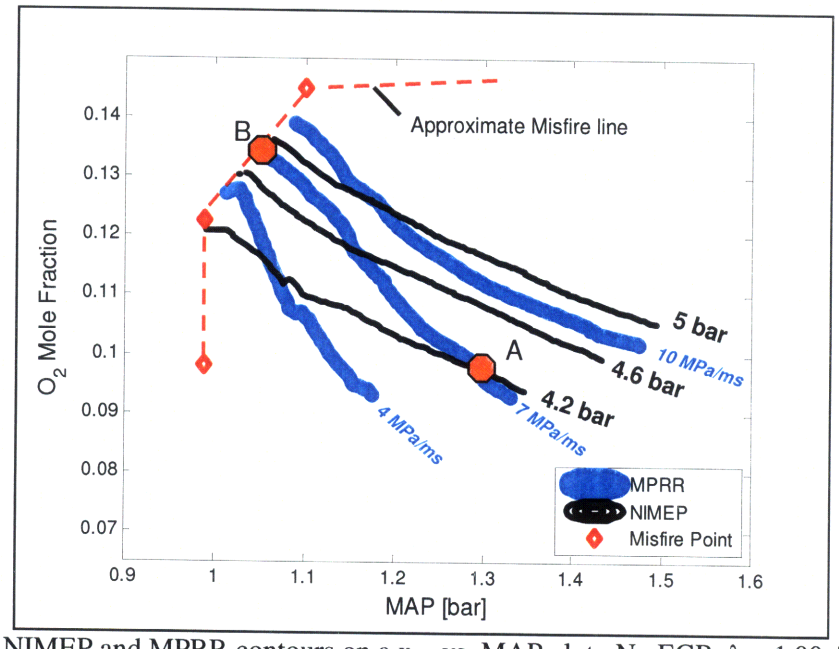

Figure 9.1: NIMEP and MPRR contours on a x_{O2} vs. MAP plot. No EGR; $\lambda = 1.00$; $T_{in} = 120°C$.

The lines of constant MPRR and NIMEP both slope downwards but the MPRR lines have a steeper slope. Thus the maximum load for a given MPRR constraint is obtained by moving the operating point along the MPRR contour line until the misfire limit is reached. To demonstrate this using Figure 9.1, consider an MPRR limit of 7 MPa/ms. Starting at operating point A, the NIMEP is 4.2 bar. Moving to the left along the 7 MPa/ms contour, the load increases until a maximum value of approximately 4.9 bar is achieved at the misfire limit (point B).

That the high load operating point occurs at the misfire limit results because the slope of the MPRR contour is steeper than the NIMEP contour. For all operating conditions considered including operating at different intake temperatures, EGR levels and lambda values, these same MPRR and NIMEP contour trends were observed. For MPRR constrained HCCI operation, the high load operating point always occurs at the misfire limit.

It is also important to note from Figure 9.1, that for a given NIMEP, the lowest MPRR is achieved at the lowest possible boost pressure. The lowest possible pressure is limited by the misfire limit. This is consistent with the data presented in Sections 8.1-8.3, where it was shown that for a given load (or fueling) the MPRR was reduced with decreasing boost pressure. This can be demonstrated in Figure 9.1 by moving the operating point along a NIMEP contour. As the operating point is moved to lower boost pressures, the MPRR is reduced until the minimum MPRR is reached at the misfire limit.

The effect of replacing trapped residual with cooled EGR is to shift the MPRR contours to the right. As discussed in Section 8.3, for a given burn fraction (and thus oxygen fraction), replacing hot trapped residual with cool EGR results in a lower charge temperature prior to ignition. This reduced charge temperature lengthens the combustion duration thus reducing the MPRR. However the reduced charge temperature that results from the addition of EGR will also affect the misfire limit. As the high load operating point occurs at the misfire limit, the effect of EGR on the MPRR constrained high load limit depends on both the shift of the MPRR curve and the affect on the misfire limit.

Figure 9.2 shows the MPRR and NIMEP contours on a plot of x_{O2} versus MAP for stoichiometric operation with 5% EGR and an intake temperature of 120°C. For a MPRR constraint of 7 MPa/ms the high load point at the misfire limit is approximately 4.9 bar (point B), which is the same value found for operation without EGR. To enable easier comparison of operating with and without EGR, the 7MPa/ms MPRR contour lines from Figure 9.1 and Figure 9.2 are shown on the same x_{O2} versus MAP plot in Figure 9.3. As Figure 9.4 shows, the constant efficiency NIMEP contours are roughly the same for 5% EGR and no EGR and only one set of NIMEP contours is shown in Figure 9.3. Again as Figure 9.3 clearly shows, the effect of adding EGR is to shift the MPRR curve to the right. However the addition of EGR also shifts the

misfire limit and the resulting high load limit moves from point A to point B and the value is roughly the same.

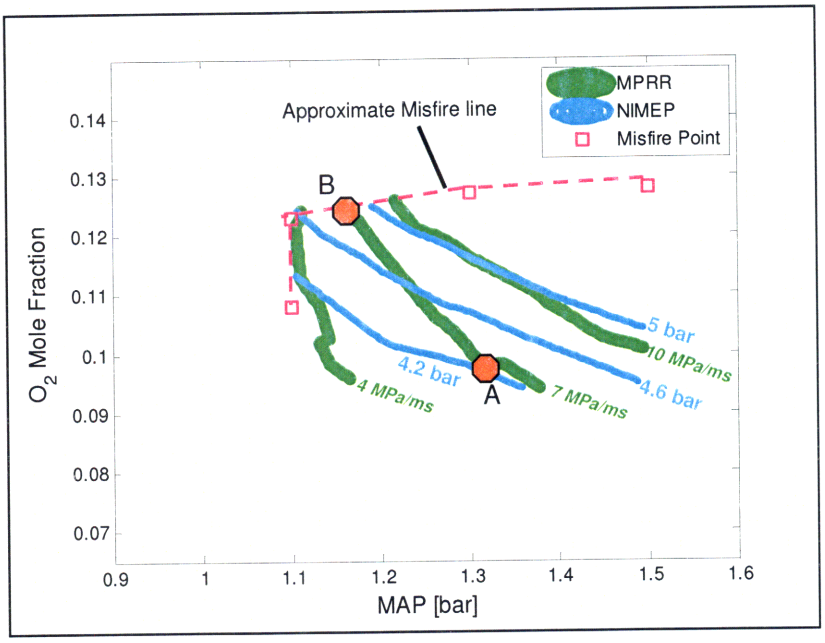

Figure 9.2: NIMEP and MPRR contours on a x_{O2} vs. MAP plot. 5% EGR; $\lambda = 1.00$; $T_{in} = 120°C$.

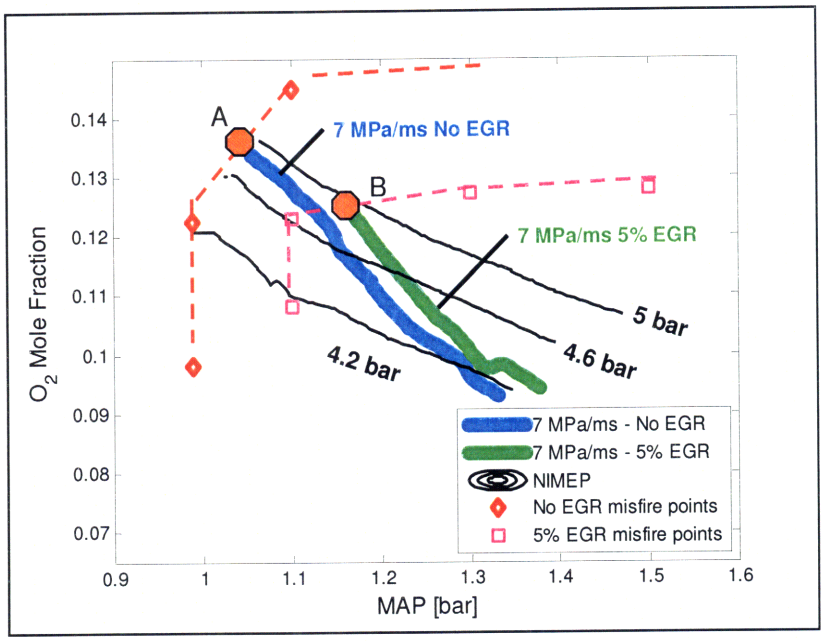

Figure 9.3: Comparison of 7 MPa/ms MPRR contours on a x_{O2} vs. MAP plot for operation with no EGR and 5% EGR. At 5% EGR the constant efficiency NIMEP contours are approximately the same as operation without EGR. $\lambda = 1.00$; $T_{in} = 120°C$.

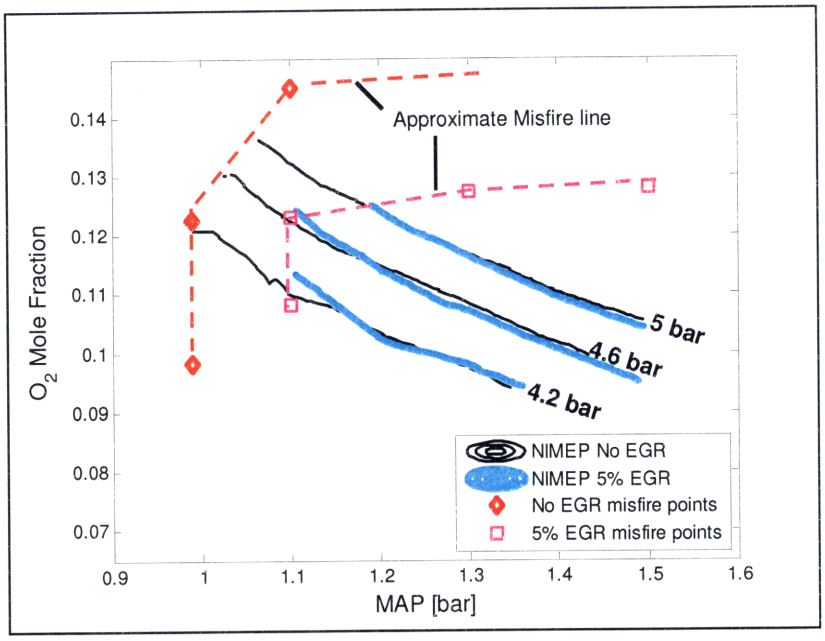

Figure 9.4: NIMEP contours on a x_{O2} vs. MAP plot for no EGR and 5% EGR; $\lambda = 1.00$; $T_{in} = 120°C$.

In this work the misfire limit was defined as the point where the engine would no longer operate. In real world engine, a high degree of robustness is needed and the operating limits would likely be defined more conservatively than the actual misfire limits. Additionally for some of the misfire points recorded, the engine did not sound "smooth" and while it may have been within MPRR limit, it would not meet NVH requirements. Thus NVH requirements would also lead to more conservative operating limits. However while the operating limit of the engine may be slightly different than the misfire limit, the maximum load for a given MPRR constraint still occurs at the point closest to the misfire limit.

The use of EGR has been shown to shift the MPRR contours to the right allowing operation at higher boost pressures for a given MPRR constraint. However as the high load limit occurs at the misfire limit any potential benefit of using EGR (with boosting) depends on how the misfire limit shifts with EGR. It was shown that for 5% EGR there does not appear to be any improvement of the high load limit however this is insufficient to conclude that EGR coupled with boosting does not allow for an increased high load limit. In Section 12, EGR sweeps are performed across a range of boost pressures, burn fractions, and intake temperatures to conclusively determine if there is any benefit to using EGR to allow operation at higher boost pressures.

The trends shown in this section utilizing actual engine data can also be shown utilizing the $1/\tau_{reaction}$ correlations coupled with WAVE simulations. In the next section this approach is described and used to demonstrate the effect of both EGR and stratification.

There were two very important findings in this section and they are restated here for clarity:

1. On a x_{O2} versus MAP plot for fixed intake temperature, the MPRR and NIMEP contours are always sloping downward and the MPRR contours always have a steeper slope.
2. For a given MPRR constraint, the high load point always occurs at the misfire limit.

10 Phenomenological correlation for $1/\tau_{reaction}$

A phenomenological correlation for $1/\tau_{reaction}$ was developed using engine operating parameters. Such a correlation is useful in exploring the HCCI operating region and examining potential operating points.

The phenomenological correlation is first developed without including any parameters to account for stratification. The form of this correlation is based on the binary reaction model. Collectively the correlation parameters completely describe the thermodynamic state and composition of the bulk charge. A linear regression is performed with the entire data set to determine the coefficients in the correlation. After developing this correlation, factors are added to capture the effects of stratification.

The $1/\tau_{reaction}$ correlation is then determined using the 10-zone combustion simulation described in Section 6. The simulation sets for the three different stratification conditions are used to determine the respective correlation coefficients.

10.1 Experimental correlation for $1/\tau_{reaction}$ without stratification factors

The form of the correlation was based on form of the binary reaction model:

$$\left(\frac{1}{\tau_{reaction}}\right)_{correlation} = a_1 \cdot x_{O2}{}^{a_2} \cdot x_{fuel}{}^{a_3} \cdot P_{165}{}^{a_4} \cdot \exp\left(\frac{a_5}{T_{165}}\right) \tag{10.1}$$

The P_{15BTC} and T_{15BTC} terms describe the thermodynamic state of the charge prior to combustion. The x_{O2} and x_{fuel} terms capture the burned gas dilution and the fuel/air ratio. Note that for a fixed λ, the ratio of x_{O2} to x_{fuel} is constant; for stoichiometric operation with UTG-91 x_{O2}/xfuel is 12.1. Also note that for a given λ, the ratio of x_{O2} to x_{burn} is constant. This is demonstrated in Figure 10.1 for some of the data used to determine the coefficients in equation (10.1). Note that the slight deviations from the lines are due to small departures from the target lambda.

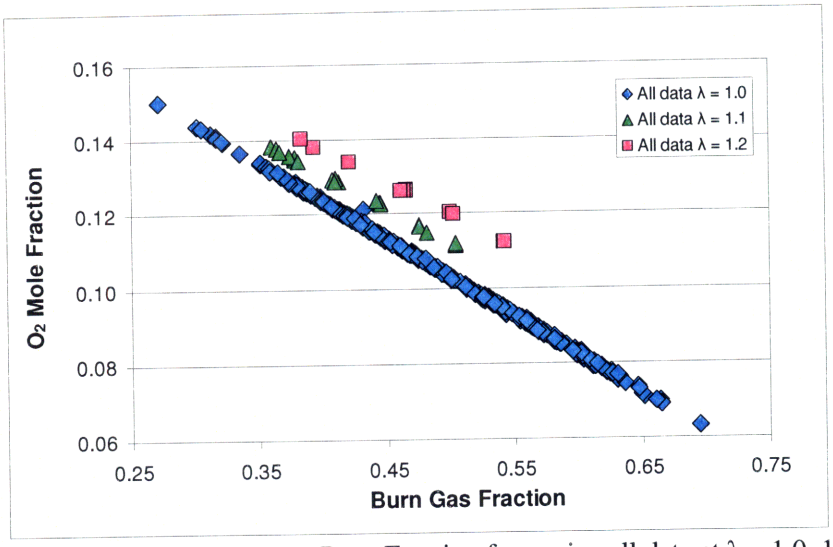

Figure 10.1: Oxygen Fraction versus Burn Fraction for engine all data at $\lambda = 1.0$, 1.1 and 1.2.

A linear regression was performed for the entire data set to determine the values of a_1 through a_5 in equation (10.1). The regression was performed using $1/\tau_{reaction}$ calculated with the following equation taken from Section 4:

$$\left(\frac{1}{\tau_{reaction}}\right)_{measured} = \underbrace{\frac{MPRR \cdot V_{CA50}}{(\gamma - 1) \cdot m_{fuel} \cdot LHV}}_{\text{Meausred Quantities}} \tag{10.2}$$

This $1/\tau_{reaction}$ calculated with measured values is referred to as the measured $1/\tau_{reaction}$ from this point forward. Using the measured $1/\tau_{reaction}$, the following correlation was obtained with an R^2 of 0.73:

$$\left(\frac{1}{\tau_{reaction}}\right)_{DATA\ correlation} = 47.5 \cdot x_{O2}^{\ 2.15} \cdot x_{fuel}^{\ 0.302} \cdot P_{165}^{\ 1.76} \cdot \exp\left(\frac{-1840}{T_{165}}\right) \tag{10.3}$$

The signs of the regression parameters a_1 through a_5 in equation (10.3) make physical sense. Increases in x_{O2}, x_{fuel}, P_{15BTC} or T_{15BTC} will increase $1/\tau_{reaction}$ (shorten the burn duration). This is in agreement with the ignition delay discussion from Section 7.

Figure 10.2 shows $1/\tau_{reaction}$ calculated with the correlation as a function of the measured $1/\tau_{reaction}$. The different CA50 ranges are indicated.

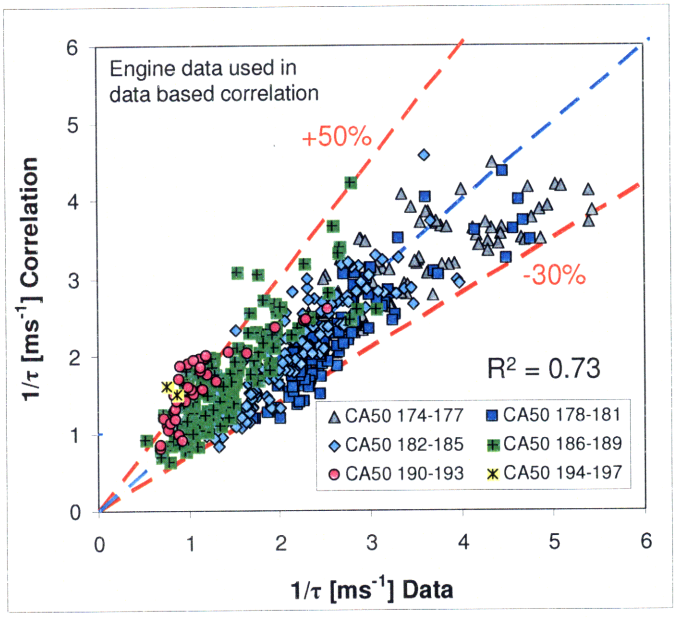

Figure 10.2: $1/\tau_{reaction}$ calculated using the data based correlation (equation (10.2)) plotted as a function of the measured $1/\tau_{reaction}$. Different CA50 ranges are indicated.

Almost all the $1/\tau_{reaction}$ values calculated with the correlation are within +50% and -30% of the measured values. The observed spread primarily results because the T_{15BTC} estimation does not fully capture the mixture temperature. Additionally the stratification may vary and the correlation does not have terms to capture this. In the next section several terms are added to the correlation to account for changes in the stratification and better capture the mixture temperature.

Note from Figure 10.2 that there is an ordering of the CA50 ranges. Starting with the points for the most advanced CA50 range, the correlation under predicts $1/\tau_{reaction}$. As the phasing retards, the correlation shifts to over predicting $1/\tau_{reaction}$. While there is some scatter in the bands of constant CA50, the spread in the predicted $1/\tau_{reaction}$ around the measured $1/\tau_{reaction}$ shows a clear ordering of the CA50 ranges. The correlation does not account for stratification and the estimated value of T_{15BTC} has considerable scatter and does not fully capture the mixture temperature. The observed ordering of the CA50 bands results because these bands capture the mixture temperature and stratification effects not captured by the terms of the correlation.

The effect of removing each of the parameters from equation (10.1) was examined and the results are provided in Table 10.1. It is important to realize that because of the interdependency between the different terms in equation (10.1), the relative decrease in R^2 can not be used directly to determine the importance of each parameter. If a metric (such as temperature) is not

properly captured, the coefficient of other interdependent terms will adjust to try to capture this missed information. This compensation from interdependent terms will affect the change in R^2 and can also lead to coefficient signs that are misleading.

Table 10.1: Effect of removing each parameter in the data based $1/\tau_{reaction}$ correlation

Correlation Form	a_1	a_2	a_3	a_4	a_5	$\mathbf{R^2}$
$\frac{1}{\tau_{reaction}} = a_1 \cdot x_{O2}^{a_2} \cdot x_{fuel}^{a_3} \cdot P_{165}^{a_4} \cdot \exp\left(\frac{a_5}{T_{165}}\right)$	117	2.14	0.215	1.53	-2450	0.73
$\frac{1}{\tau_{reaction}} = a_1 \cdot x_{O2}^{a_2} \cdot x_{fuel}^{a_3} \cdot P_{165}^{a_4}$	3.08	2.31	0.205	1.97	NA	0.72
$\frac{1}{\tau_{reaction}} = a_1 \cdot x_{O2}^{a_2} \cdot x_{fuel}^{a_3} \cdot \exp\left(\frac{a_5}{T_{165}}\right)$	105000	1.94	-0.126	NA	-6500	0.65
$\frac{1}{\tau_{reaction}} = a_1 \cdot x_{O2}^{a_2} \cdot P_{165}^{a_4} \cdot \exp\left(\frac{a_5}{T_{165}}\right)$	66.8	2.31	NA	1.50	-2440	0.73
$\frac{1}{\tau_{reaction}} = a_1 \cdot x_{fuel}^{a_3} \cdot P_{165}^{a_4} \cdot \exp\left(\frac{a_5}{T_{165}}\right)$	77500	NA	2.06	1.31	-4150	0.60

The removal of the T_{15BTC} term only reduces the correlation R^2 from 0.73 to 0.72. The small change in R^2 results because the estimated values for T_{15BTC} have significant scatter and fail to fully capture the actual mixture temperature. As a result the dependence the T_{15BTC} term is quite weak. The regressed values for a_2, a_3 and a_4 do no change significantly when the T_{15BTC} term is removed. It is shown later using multi-zone combustion simulations that the dependence on temperature is actually much stronger than indicated by the data based correlation.

The removal of the P_{15BTC} term reduces the R^2 from 0.73 to 0.65 and significantly affects the value of the other parameters. The regression parameters change significantly to compensate for the removal of the P_{15BTC} term. Notice the sign of a_3 becomes negative with the removal of the P_{15BTC} term. This results because for many of the NVO sweeps lower residual fractions were achievable at low boost pressures without reaching unacceptable MPRR levels. Thus there is a slight negative correlation between P_{15BTC} and x_{fuel} and this accounts for the negative value of a_3 when the P_{15BTC} term is removed.

The removal of the x_{fuel} term does not change the R^2 value and has little effect on the regression parameters. This results in part because 85% of the data (446 of the 526 regressed data points) was for stoichiometric operation and the ratio of x_{fuel} to x_{O2} was constant for these points.

Additionally the range of lambda values explored was relatively small with the largest lambda value being only 1.23. These factors result in a weak dependence on x_{fuel} for this data set.

The removal of the x_{O2} term reduces the R^2 from 0.73 to 0.60 and the regression parameters change significantly to compensate. Notice that the exponent for x_{fuel} becomes 2.21; this results because for 85% of the data the ratio of x_{O2} to x_{fuel} is constant and for these points the dependence on x_{O2} is captured by x_{fuel}.

10.2 Experimental correlation for $1/\tau_{reaction}$ with additional factors

Changes in the thermal and composition stratification between different operating points accounts for some of the error between the correlated and measured values of $1/\tau_{reaction}$. The other significant source of error was in the T_{15BTC} estimate. The estimated T_{15BTC} value did not fully capture the mixture temperature. The correlation given by equation (10.1) was modified to account the changing stratification and better capture the mixture temperature. As the stratification was not directly measured, several metrics were defined to capture the varying thermal and composition stratification. In addition to capturing the stratification, these metrics also capture some of the temperature differences that the estimated T_{15BTC} term misses. The objective of adding these additional terms was to demonstrate that stratification and the scatter in the T_{15BTC} estimate account for the errors observed in the correlation.

One metric that partially describes the thermal stratification is the difference between the residual temperature and the mixture intake temperature. As discussed in Section 7.2.2, the mixing of the fresh charge with the hot trapped residual leads to substantial thermal stratification. For a given residual gas fraction, increasing the difference between the residual temperature and the intake temperature will provide increased thermal stratification. The residual temperature at IVO was not directly measured but can be estimated as discussed in Section 3.4.

The residual trapped fraction can also be used to partially describe the thermal and composition stratification. The fresh charge and residual fraction have very different temperatures and compositions. As the residual gas fraction is increased from 0%, the thermal stratification increases. If the residual gas fraction is increased significantly beyond 50% the thermal stratification begins to decline because a majority of the mixture is now trapped residual. Roughly speaking, at a residual gas fraction of 50%, the mixing required to achieve a homogeneous mixture is greatest. Thus holding other factors constant, including the residual

temperature and heat transfer to the walls, the thermal and composition stratification is at a maximum when the trapped residual gas fraction is approximately 50%. The charge stratification was thus assumed to have a parabolic relationship with residual fraction with a maximum occurring at 50%. The metric used to capture this effect is $x_{trap}(1 - x_{trap})$.

The molar EGR fraction is another important metric for describing the thermal and composition stratification (the metric used was $1 - x_{EGR}$). In this experimental setup, the EGR was well mixed with the intake charge and was at the same temperature as the intake charge. Thus for a given burn gas fraction, increasing the amount of EGR (replacing hot trapped residual with cool EGR) will both lower the bulk temperature and potentially alter the stratification (both composition and thermal stratification). The effect of EGR on the stratification depends on many variables including the in-cylinder turbulence, the trapped residual fraction and the EGR rate. To demonstrate how the effect of EGR depends on the total burn fraction the effect of 15% EGR is examined for burn fractions of 40 and 70% in Table 10.2. Recall that the EGR rate is defined as the percentage of EGR in the fresh charge.

Table 10.2: Examination of the effect of EGR on the charge stratification

Burn Gas Fraction	No EGR	15% EGR Rate	Effect of EGR on stratification
$\mathbf{x_{burn} = 40\%}$	$x_{trap} = 40\%$	$x_{EGR} = 10.6\%$ $x_{trap} = 29.4\%$	For a burn fraction of 40%, operating with 15% EGR, increases the amount of well mixed cool charge to 70.6% of the total in-cylinder charge (compared to 60% for no EGR). Thus adding EGR reduces the amount of hot residual that must that must mix with the essentially homogeneous fresh charge. It is speculated that this will provide a reduction in the thermal and composition stratification.
$\mathbf{x_{burn} = 70\%}$	$x_{trap} = 70\%$	$x_{EGR} = 5.3\%$ $x_{trap} = 64.7\%$	For a burn fraction of 70%, operating with 15% EGR, increases the amount of well mixed cool charge to 35.3% of the total in-cylinder charge (compared to 30% for no EGR). The amount of mixing required to achieve a homogeneous charge increases and it is speculated that this will lead to an increase in the thermal and composition stratification.

The effect of EGR on the thermal and composition stratification depends on many factors and increased in EGR likely results in increased stratification for some points and reduced stratification for others. However for all the EGR rates considered, increases in EGR (while holding burn gas fraction constant) lengthened the combustion duration. This lengthening of the combustion duration was driven by the reduced bulk temperature and it is concluded that the

effect of EGR on the bulk temperature dominates any changes in stratification. Because the EGR fraction strongly affects the bulk temperature, adding the $1 - x_{EGR}$ term to the correlation helps capture the changes in the bulk temperature which the T_{15BTC} estimate fails to fully capture.

The effect of adding these three metrics to the correlation are summarized in Table 10.3. While not shown, the exponents for each stratification term were strongly dependant on which of the other stratification terms were added. This is due to the high degree of interdependency between the defined stratification metrics.

Table 10.3: Effect of adding stratification terms

Stratification terms to equation (10.1)	R^2
$(T_{IVO} - T_{Intake})^{a_6} \cdot (x_{trap} \cdot (1 - x_{trap}))^{a_7} \cdot (1 - x_{EGR})^{a_8}$	**0.89**
$(T_{IVO} - T_{Intake})^{a_6}$	**0.79**
$(x_{trap} \cdot (1 - x_{trap}))^{a_7}$	**0.73**
$(1 - x_{EGR})^{a_8}$	**0.85**
$(T_{IVO} - T_{Intake})^{a_6} \cdot (x_{trap} \cdot (1 - x_{trap}))^{a_7}$	**0.79**
$(T_{IVO} - T_{Intake})^{a_6} \cdot (1 - x_{EGR})^{a_8}$	**0.87**
$(x_{trap} \cdot (1 - x_{trap}))^{a_7} \cdot (1 - x_{EGR})^{a_8}$	**0.88**

The addition of the $T_{IVO} - T_{intake}$ and $1 - xEGR$ both improved the fit, bringing R^2 to 0.79 and 0.85 respectively. Conversely the addition of the $x_{trap}(1 - x_{trap})$ term provided essentially no improvement in the fit. The strong improvement with the $1 - x_{EGR}$ term is thought to be because it captures much of the temperature information that is missed by the T_{15BTC} term. Notice that when the $x_{trap}(1 - x_{trap})$ term is added with the $1 - x_{EGR}$, the fit improves slightly to an R^2 of .87. The highest R^2 was achieved when all three terms were added to the correlation and provided an R^2 of 0.89. The correlation obtained for the data set with the addition of these three terms was:

$$\frac{1}{\tau_{reaction}} = 127 \cdot x_{O2}^{0.842} \cdot x_{fuel}^{0.729} \cdot P_{165}^{1.99} \cdot \exp\left(\frac{-4840}{T_{165}}\right) \cdot (T_{IVO} - T_{Intake})^{-0.582} \cdot (x_{trap} \cdot (1 - x_{trap}))^{-3.19} \cdot (1 - x_{EGR})^{7.01} \quad (10.4)$$

The signs of the regression coefficients a_1 through a_5 match those obtained for the correlation without stratification terms however the values of the coefficients are significantly different. The differences in the coefficient values results from the dependencies between the terms.

As discussed before, the terms are not independent and if a metric (such as temperature) is not properly captured, the coefficient of other interdependent terms will adjust which can produce misleading coefficient signs. However the signs of coefficients a_6 through a_8 appear to make physical sense. The negative sign for a_6 means that increasing $T_{exh} - T_{int}$, while holding the other parameters constant, lengthens the combustion duration. This is in agreement with the above discussion. The negative exponent for the $x_{trap}(1 - x_{trap})$ term indicates that the $x_{trap}(1 - x_{trap})$ term is a minimum at a trapped residual fraction of 50%. Thus holding all other metrics constant, the burn duration is longest at a trapped residual fraction of 50%. This is consistent with the thermal and composition stratification reaching a maximum around 50% residual trapped fraction.

The $1 - x_{EGR}$ term has a positive exponent. Increases in x_{EGR}, while holding other parameters constant, leads to reductions in $1/\tau_{reaction}$ (increases in burn duration). As discussed earlier, for a given burn gas fraction, increasing x_{EGR} (replacing trapped residual with EGR) can lead to reductions in the thermal and composition stratification. Stratification reductions work towards reducing the burn duration however for all points considered increases in x_{EGR} (for a given total burn fraction) lengthened the burn duration. This indicates that the effect of EGR on the bulk temperature dominates. This temperature effect should be captured by the T_{15BTC} term but T_{15BTC} is not directly measured and features sizable scatter. Thus the x_{EGR} term is primarily capturing the effect of EGR on the bulk temperature.

Figure 10.3 shows $1/\tau_{reaction}$ calculated using the modified correlation (equation (10.4)) as a function of $1/\tau_{reaction}$ calculated directly from engine data using equation (10.2). The different CA50 ranges are indicated.

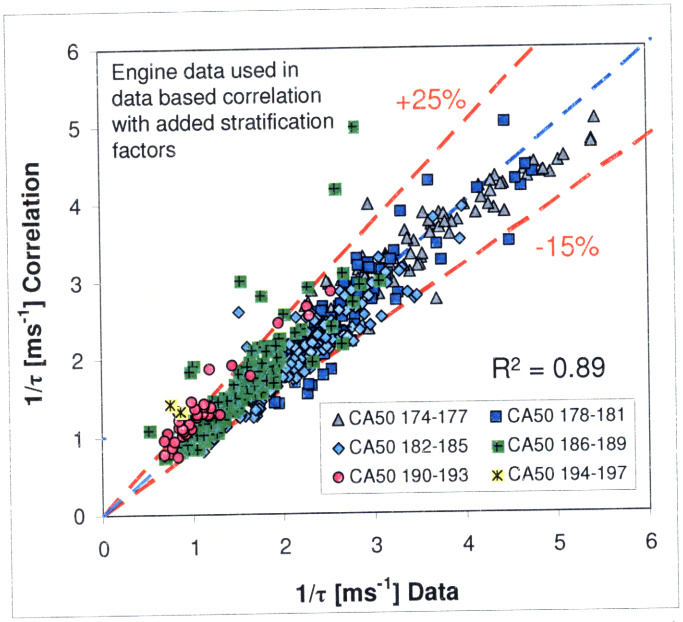

Figure 10.3: $1/\tau_{reaction}$ calculated using the data based correlation with added stratification terms (equation (10.4)) plotted as a function of the measured $1/\tau_{reaction}$. Different CA50 ranges are indicated.

When the correlation was modified to include stratification factors, the agreement between the correlated and measured values of $1/\tau_{reaction}$ was quite good. Most of the correlated $1/\tau_{reaction}$ values were within +25% and -15% of the measured values. Notice from Figure 10.3 that there are no observable CA50 bands. This indicates that the added terms helped to better capture the thermal stratification and bulk temperature. The remaining error is thought to largely result from any temperature and stratification effects that were not captured by the additional terms. The 10-zone model allowed the correlation coefficients to be determined for constant stratification and known T_{15BTC}. These 10-zone model based $1/\tau_{reaction}$ correlations are discussed in the next section.

10.3 $1/\tau_{reaction}$ correlation using 10-zone model

Correlations for $1/\tau_{reaction}$ were obtained using the 10-zone combustion simulations described in Section 6.2. As described in Section 6.2, a matrix of simulations were performed at three different stratification conditions. A linear regression was performed for each stratification condition to determine a_1 through a_5 in equation (10.1). As the stratification was constant for each correlation, the was no error due to changes in stratification. Additionally the correlation terms x_{O2}, x_{fuel}, P_{15BTC} and T_{15BTC} were all known values and the measurement error was eliminated. This was of particular importance for T_{15BTC}. In the data-based $1/\tau_{reaction}$ correlation,

the scatter in the estimated T_{15BTC} significantly reduced the correlation's functional dependence on the T_{15BTC} term.

The $1/\tau_{reaction}$ values used in the regression analysis were calculated using the following equation taken from Section 4:

$$\left(\frac{1}{\tau_{reaction}}\right)_{simulation} = \underbrace{\frac{MPRR \cdot V_{CA50}}{(\gamma - 1) \cdot m_{fuel} \cdot LHV}}_{\text{Simulation Quantities}} \tag{10.5}$$

In equation (10.5) m_{fuel} and V_{CA50} were obtained directly from simulation output and γ was assumed constant. The MPRR was defined as the pressure rise rate between 35% mass fraction burned and 65% mass fraction burned.

10.3.1 10-zone $1/\tau_{reaction}$ correlation with TW = 50K

The $1/\tau_{reaction}$ correlation was determined for the simulation data set with a fixed thermal width of 50K and constant composition. A linear regression of this simulated data set was performed using the simulated values of $1/\tau_{reaction}$ (equation (10.5)). The following correlation was obtained with an R^2 of 0.94:

$$\left(\frac{1}{\tau_{reaction}}\right)_{correlation,\ TW=50K} = 8.08e6 \cdot x_{O2}^{1.51} \cdot x_{fuel}^{1.04} \cdot P_{165}^{1.23} \cdot \exp\left(\frac{-10800}{T_{165}}\right) \tag{10.6}$$

The dependence on T_{15BTC} is much stronger for the TW = 50K simulation correlation than for the engine data based correlation because T_{15BTC} was accurately known.

The effect of removing each of the parameters from equation (10.1) was examined and the results are provided in Table 10.4. Again it is important to realize that because of the interdependency between the different terms in equation (10.1), the relative decrease in R^2 can not be used directly to determine the importance of each parameter.

Removal of any of the parameters from the model results in a significant reduction in the regression R^2. The value of the coefficients change substantially with the removal of a term because the remaining terms are trying to compensate for the missing term. Interdependencies between the terms affect the way the regression coefficients adjust to compensate.

Table 10.4: Importance of each parameter in $1/\tau_{reaction}$ correlation for TW = 50K simulation set

Correlation Form	a_1	a_2	a_3	a_4	a_5	R^2
$\frac{1}{\tau_{reaction}} = a_1 \cdot x_{O2}^{a_2} \cdot x_{fuel}^{a_3} \cdot P_{165}^{a_4} \cdot \exp\left(\frac{a_5}{T_{165}}\right)$	8.08e6	1.51	1.04	1.23	-10800	**0.94**
$\frac{1}{\tau_{reaction}} = a_1 \cdot x_{O2}^{a_2} \cdot x_{fuel}^{a_3} \cdot P_{165}^{a_4}$	6.48	1.05	-0.073	0.0892	**NA**	**0.50**
$\frac{1}{\tau_{reaction}} = a_1 \cdot x_{O2}^{a_2} \cdot x_{fuel}^{a_3} \cdot \exp\left(\frac{a_5}{T_{165}}\right)$	2.82e5	1.20	0.553	**NA**	-6830	**0.77**
$\frac{1}{\tau_{reaction}} = a_1 \cdot x_{O2}^{a_2} \cdot P_{165}^{a_4} \cdot \exp\left(\frac{a_5}{T_{165}}\right)$	179	1.01	**NA**	0.323	-3580	**0.67**
$\frac{1}{\tau_{reaction}} = a_1 \cdot x_{fuel}^{a_3} \cdot P_{165}^{a_4} \cdot \exp\left(\frac{a_5}{T_{165}}\right)$	716	**NA**	0.206	0.275	-5780	**0.27**

Figure 10.4 shows $1/\tau_{reaction}$ calculated using the correlation (equation (10.6)) as a function of $1/\tau_{reaction}$ calculated directly from simulation values in equation (10.5). The temperature sweeps, pressure sweeps, burn fraction sweeps and lambda sweeps are all accurately captured by the correlation.

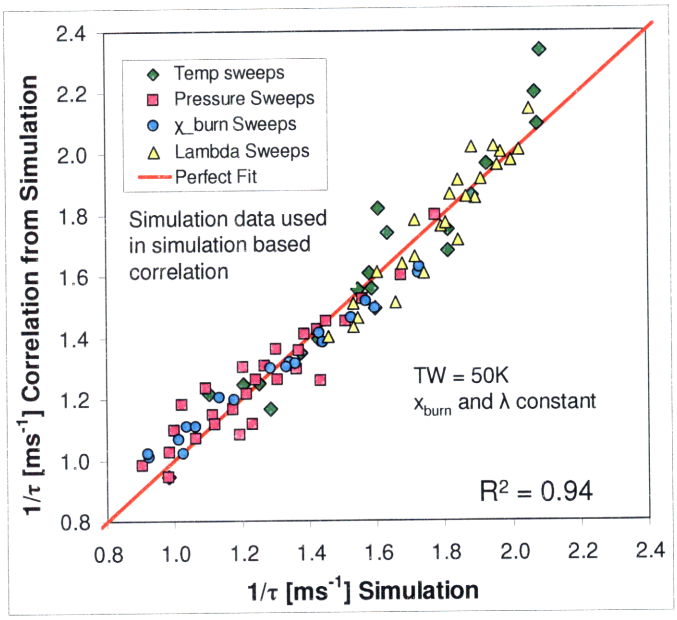

Figure 10.4: $1/\tau_{reaction}$ calculated using the TW = 50K correlation (equation (10.5)) plotted as a function of the TW = 50K simulation $1/\tau_{reaction}$.

10.3.2 10-zone $1/\tau_{reaction}$ correlation with TW = 25K

The $1/\tau_{reaction}$ correlation was determined for the simulation data set with a fixed thermal width of 25K and constant composition. A linear regression of this simulated data set was performed using the simulated values of $1/\tau_{reaction}$ (equation (10.5)). The following correlation was obtained with an R^2 of 0.92:

$$\left(\frac{1}{\tau_{reaction}}\right)_{correlation,\ TW=25K} = 1.65e6 \cdot x_{O2}^{\ 1.33} \cdot x_{fuel}^{\ 0.688} \cdot P_{165}^{\ 1.16} \cdot \exp\left(\frac{-10500}{T_{165}}\right) \qquad (10.7)$$

As with the correlation for the TW = 50K, the T_{15BTC} dependence is much stronger for the simulation correlation than for the engine data based correlation. Removal of any of the parameters from the model resulted in a significant reduction in the regression R^2 and the coefficient values changes substantially to try compensate for the missing term.

Figure 10.5 shows $1/\tau_{reaction}$ calculated using the correlation (equation (10.7)) as a function of $1/\tau_{reaction}$ calculated directly from simulation values in equation (10.5). The temperature sweeps, pressure sweeps, burn fraction sweeps and lambda sweeps are all accurately captured by the correlation.

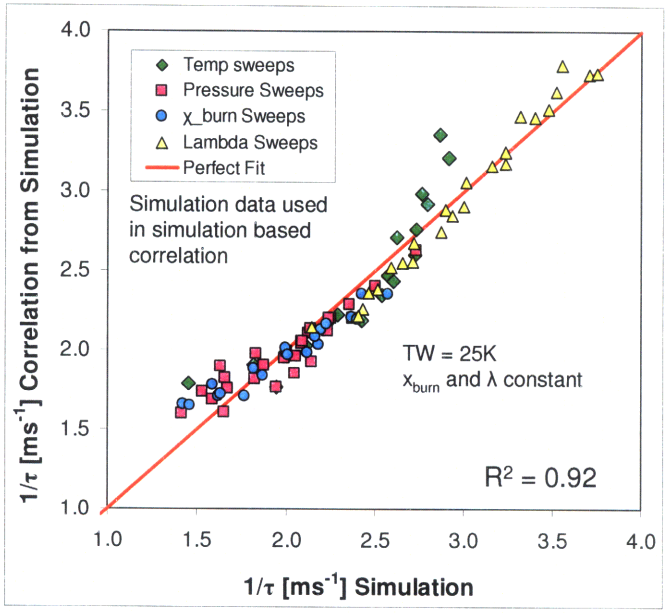

Figure 10.5: $1/\tau_{reaction}$ calculated using the TW = 25K correlation (equation (10.5)) plotted as a function of the TW = 25K simulation $1/\tau_{reaction}$.

10.3.3 10-zone $1/\tau_{reaction}$ correlation with Temperature – Composition Stratification Linked with TW = 50K

The $1/\tau_{reaction}$ correlation was determined for the simulation data set with a fixed thermal width of 50K and the x_{burn} and lambda in each zone calculated assuming adiabatic mixing (as described in Appendix A). A linear regression of this simulated data set was performed using the simulated values of $1/\tau_{reaction}$ (equation (10.5)). The following correlation was obtained with an R^2 of 0.92:

$$\left(\frac{1}{\tau_{reaction}}\right)_{correlation,\ Temp-Composition,\ TW=50K} = 4.63e7 \cdot x_{O2}^{\ 1.34} \cdot x_{fuel}^{\ 1.15} \cdot P_{165}^{\ 1.43} \cdot \exp\left(\frac{-12800}{T_{165}}\right) \qquad (10.8)$$

As with the other simulation correlations, the T_{15BTC} dependence is much stronger than for the engine data based correlation. Figure 10.6 shows $1/\tau_{reaction}$ calculated using the correlation (equation (10.8)) as a function of $1/\tau_{reaction}$ calculated directly from simulation values in equation (10.5). The temperature sweeps, pressure sweeps, burn fraction sweeps and lambda sweeps are all accurately captured by the correlation.

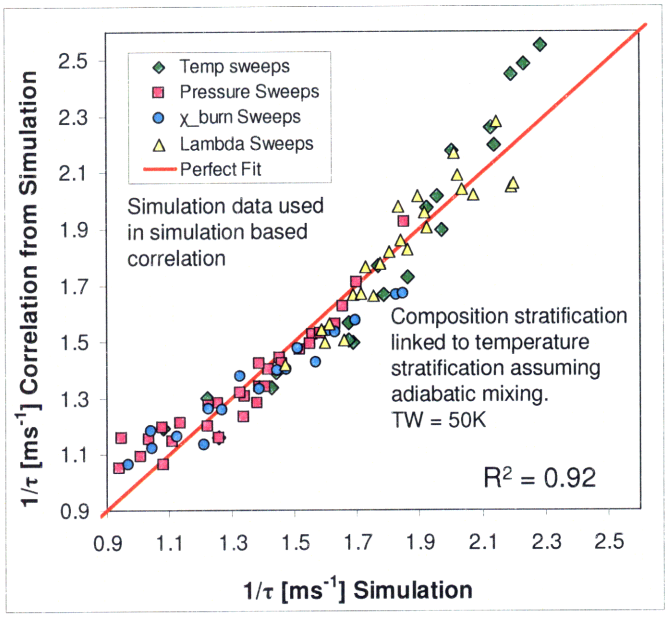

Figure 10.6: $1/\tau_{reaction}$ calculated using the temperature-composition stratification correlation (equation (10.5)) plotted as a function of the simulation $1/\tau_{reaction}$.

11 Using $1/\tau_{reaction}$ correlation to explore the HCCI operating region

The HCCI operating region and high load limit were also examined utilizing the correlations developed for $1/\tau_{reaction}$ coupled with WAVE simulations. These correlations have the form:

$$\left(\frac{1}{\tau_{reaction}}\right)_{correlation} = a_1 \cdot x_{O2}^{\ a_2} \cdot x_{fuel}^{\ a_3} \cdot P_{165}^{\ a_4} \cdot \exp\left(\frac{a_5}{T_{165}}\right) \tag{11.1}$$

WAVE was used generate values for the x_{O2}, x_{fuel}, P_{15BTC} and T_{15BTC} terms across a range of pressures and NVO timings. The $1/\tau_{reaction}$ values calculated using the correlation were then used to determine the MPRR with the following equation derived in Section 5:

$$MPRR = \left(\frac{1}{\tau_{reaction}}\right)_{correlation} \cdot \left(\frac{(\gamma - 1) \cdot m_{fuel} \cdot LHV}{V_{CA50}}\right) \tag{11.2}$$

As shown in Section 8, changes in γ and V_{CA50} are very small compared to changes in $1/\tau_{reaction}$ and these values were assumed constant. The fuel mass was determined directly from the WAVE simulations.

WAVE simulations were performed for operation without EGR and with 10% EGR. For each set of simulations, the NVO timing was swept from 60 to 125° in 5° increments at intake pressures of 1, 1.2, 1.4, 1.6 and 1.8 bar. The exhaust pressure was held equal to the intake pressure and the intake temperature was fixed at 50°C. Table 11.1 provides the important model parameters used in the WAVE simulations.

Table 11.1: Wave Model Parameters

Compression Ratio	9.94
Bore [mm]	80.26
Stroke [mm]	88.90
Head Temperature [K]	550
Piston Temperature [K]	520
Cylinder Wall Temperature [K]	500

The geometry of the WAVE model engine was identical to that of the test engine and 10-zone simulation. The combustion duration and timing were held constant for these simulations. Additionally the engine surface temperatures were held constant. These simplifications primarily affected the value for T_{15BTC}. The repercussions of this are discussed below.

As discussed in Section 10, the data based $1/\tau_{reaction}$ correlation has a weak dependence on T_{15BTC} that results from the high degree of scatter in the T_{15BTC} estimate. The 10-zone model based $1/\tau_{reaction}$ correlations are used because they better capture the temperature dependence and enable comparison of different stratification levels.

Figure 11.1 shows the MPRR and MEP contours on a plot of x_{O2} versus MAP for stoichiometric operation without EGR obtained using the $1/\tau_{reaction}$ correlation from the TW = 50K simulation. The MPRR and MEP contours show the same trends as observed for the data set. They are both sloping downwards and the slope of the MPRR contour is steeper. Thus for a given MPRR constraint the maximum MEP is achieved at the misfire limit. Again, this can be demonstrated by starting at point A (MEP = 4.5 bar) and moving the operating point along the 7 MPa/ms contour until the misfire limit is reached at point B (MEP = 6.5 bar).

The MEP values were computed from the WAVE generated fuel mass using a fixed efficiency of 33%. The misfire line is approximated using a T_{15BTC} threshold of 890 K. The misfire limit depends on many factors and this temperature threshold is a very rough approach. However as discussed earlier, the exact location of the misfire limit does not change the conclusion that the high load limit occurs at the misfire limit. This lack of a strong metric for misfire is an issue when examining the EGR as discussed later on.

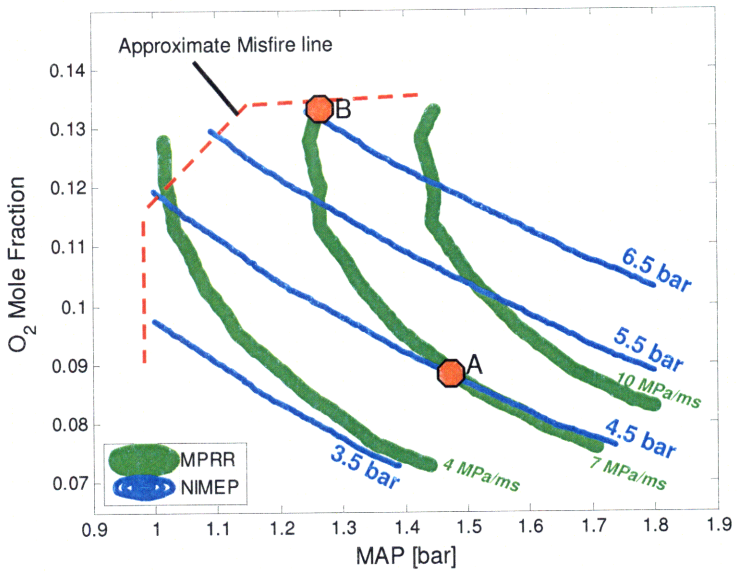

Figure 11.1: MEP and MPRR contours on a x_{O2} vs. MAP plot. The contours were generated using WAVE generated values for x_{O2}, x_{fuel}, P_{15BTC} and T_{15BTC} in the $1/\tau_{reaction}$ correlation obtained from the TW = 50K 10-zone simulations. No EGR; $\lambda = 1.00$; $T_{in} = 120°C$.

Note that the MPRR contours in Figure 11.1 curve upward more sharply than for the engine data. In the WAVE model the calculated T_{15BTC} drops at a faster rate with increased x_{O2} (decreased x_{trap}) than in a real engine. This more rapidly dropping temperature works against the effect of increased oxygen fraction in the $1/\tau_{reaction}$ correlation and accounts for the sharply increasing slope of the MPRR contours in Figure 11.1. The WAVE calculated T_{15BTC} drops at a faster rate because the metal surface temperatures are assumed constant in the WAVE model and increases in load (increased x_{O2}) do not provide increased metal surface temperature. In an actual engine increased load leads to increased metal surface temperature and this increased surface temperature negates some of the temperature drop that occurs with reduced trapped hot residual.

While the simulation based MPRR contour is steeper at the misfire limit than the data based contour, the simulation based plots still provide insight on how changes to the engine dilution or stratification affect the high load limit. The effect of EGR on the MPRR contour is first demonstrated and results support the experimental findings. The simulation is then used to examine the effect of stratification on the high load limit.

11.1 Effect of EGR on HCCI operating region

The effect of EGR on the HCCI operating region can be shown using the $1/\tau_{reaction}$ correlation coupled with WAVE data. Figure 11.2 shows the 7 MPa/ms contours for operation without EGR and with 10% EGR. These contours were calculated as described above using x_{O2}, x_{fuel}, P_{15BTC} and T_{15BTC} from the WAVE simulations in the $1/\tau_{reaction}$ correlation from the TW = 50K simulation. The 10% EGR contour utilized the WAVE matrix for 10% EGR and the no EGR contour utilized the WAVE matrix for no EGR. The 10% EGR constant efficiency MEP contours are roughly the same as those without EGR and only one set of MEP contours is shown.

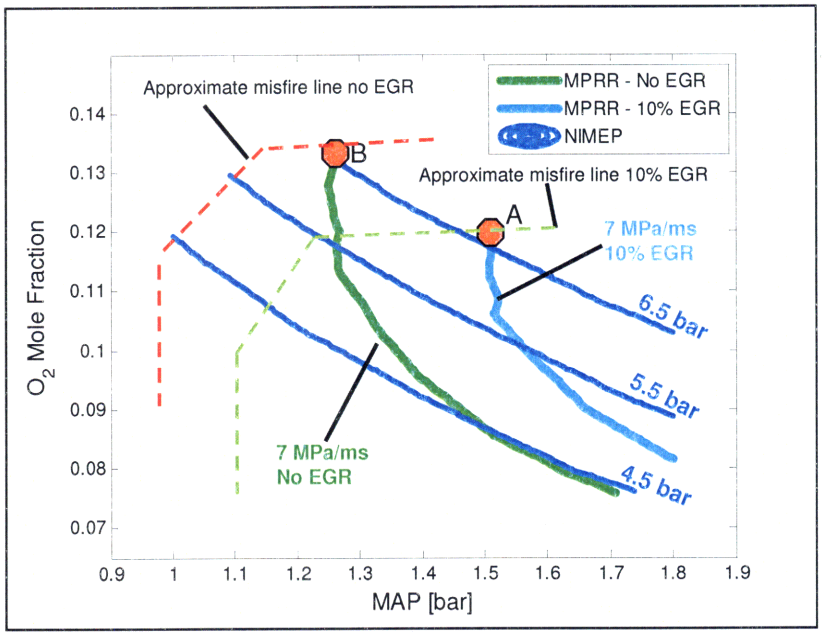

Figure 11.2: Comparison of 7 MPa/ms MPRR contours on a x_{O2} vs. MAP plot for operation with no EGR and 10% EGR. MPRR contours calculated using WAVE values in $1/\tau_{reaction}$ correlation from the TW = 50K simulation. At 10% EGR the constant efficiency MEP contours are approximately the same as operation without EGR. $\lambda = 1.00$; $T_{in} = 50°C$.

In agreement with the data set, operation with EGR shifts the MPRR contour to the right. This shift is driven by the effect of EGR on temperature as the other terms in the $1/\tau_{reaction}$ correlation did not change significantly with EGR. As discussed above, the misfire limit was roughly defined by a T_{15BTC} threshold of 890K. Using this rough misfire definition, the high load limit did not increase with the addition EGR. The approximated misfire limit prevents these simulations from being used to draw any definite conclusions regarding using EGR with boosting. However this demonstrates the usefulness of the developed $1/\tau_{reaction}$ correlation. These types of plots can be generated very quickly across a range of conditions and used to quickly

examine a potential operating region. An accurate misfire correlation would further extend the usefulness of these $1/\tau_{reaction}$ correlations.

11.2 Effect of stratification on HCCI operating region

The $1/\tau_{reaction}$ correlations can also be used to examine the effect of stratification. In this section the effect of composition stratification is first examined utilizing the $1/\tau_{reaction}$ correlation developed for the temperature-composition linked 10-zone simulations. The effect of thermal stratification is then explored.

11.2.1 Effect of composition stratification

Figure 11.3 compares the MPRR contours calculated from the $1/\tau_{reaction}$ correlation for the temperature-composition linked 10-zone simulations and the MPRR contours calculated from the $1/\tau_{reaction}$ correlation for the fixed composition 10-zone simulations. The temperature profile was the same for both 10-zone simulations and any differences in the MPRR contours are due to the composition profile. Values for x_{O2}, x_{fuel}, P_{15BTC} and T_{15BTC} were determined with WAVE for operation without EGR.

As described in Appendix A, the composition stratification was linked to the temperature stratification by assuming adiabatic mixing between the cool fresh charge and hot residual. Thus the higher temperature zones had higher burn gas fractions (lower oxygen fractions) and reduced fuel content. The lower temperature zones had lower burn fractions (higher oxygen fractions) and increased fuel content. These effects cause the high temperature zones to ignite later and the low temperature zones to ignite earlier thus shortening the burn duration. This shortening of the burn duration was observed in the simulations as shown in Figure 6.3 of Section 6, however the shortening effect was relatively small.

Using the $1/\tau_{reaction}$ correlations from the simulations, the expected effect of composition stratification on the MPRR was observed at low oxygen fractions. That is for a given oxygen fraction and boost pressure, the MPRR was higher with composition stratification. However the composition stratified MPRR contour lines were steeper and at higher oxygen fractions the stratified MPRR contours crossed the constant composition contours. This crossing of the contours occurred very close to the approximated misfire limit such that the maximum load for a given MPRR was essentially the same.

The stratified composition contours were steeper than the constant composition contours because the temperature dependence was stronger in the composition stratified $1/\tau_{reaction}$ correlation. As discussed earlier, as the oxygen fraction is increased the mixture temperature is reduced and the reduction in temperature calculated with the WAVE simulations is stronger than actual engine data. This more rapid fall in temperature amplified the effect of the stronger temperature dependence in the composition stratified $1/\tau_{reaction}$ correlation leading to the steeper MPRR contours.

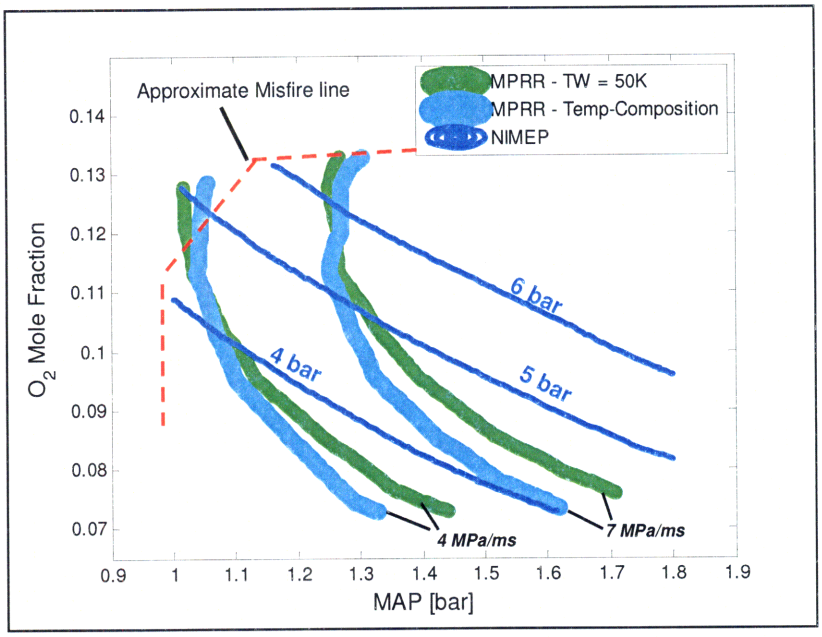

Figure 11.3: Comparison of 7 MPa/ms MPRR contours on a x_{O2} vs. MAP plot for operation with no EGR. MPRR contours calculated using WAVE values in $1/\tau_{reaction}$ correlations from the TW = 50K and Temperature-Composition Linked 10-zone simulations. $\lambda = 1.00$; $T_{in} = 50°C$.

11.2.2 Effect of thermal stratification

Figure 11.4 compares the MPRR contours calculated from the $1/\tau_{reaction}$ correlations for TW = 25K and TW = 50K. Values for x_{O2}, x_{fuel}, P_{15BTC} and T_{15BTC} were determined with WAVE for operation without EGR.

Increasing the thermal stratification increases the burn duration and thus reduces the MPRR. Referring to Figure 11.4, doubling the thermal width from 25K to 50K increases the high load limit from 4.8 bar MEP at point A to 6.3 bar MEP at point B. Again the size of this increase depends on the details of the misfire limit. However unlike EGR, stratification does not shift the misfire limit to lower oxygen fractions. In fact, increases in stratification generally extend the

misfire limit to higher oxygen fractions (lower bulk temperatures) because the hottest parcels are sufficiently hot for ignition to occur. While the effect of stratification on the misfire limit was only approximated, the potential benefit of extending the misfire limit is clearly demonstrated. This again demonstrates the usefulness of the developed $1/\tau_{reaction}$ correlations. It is also important to note that in a practical engine a doubling of the thermal stratification would be difficult to achieve.

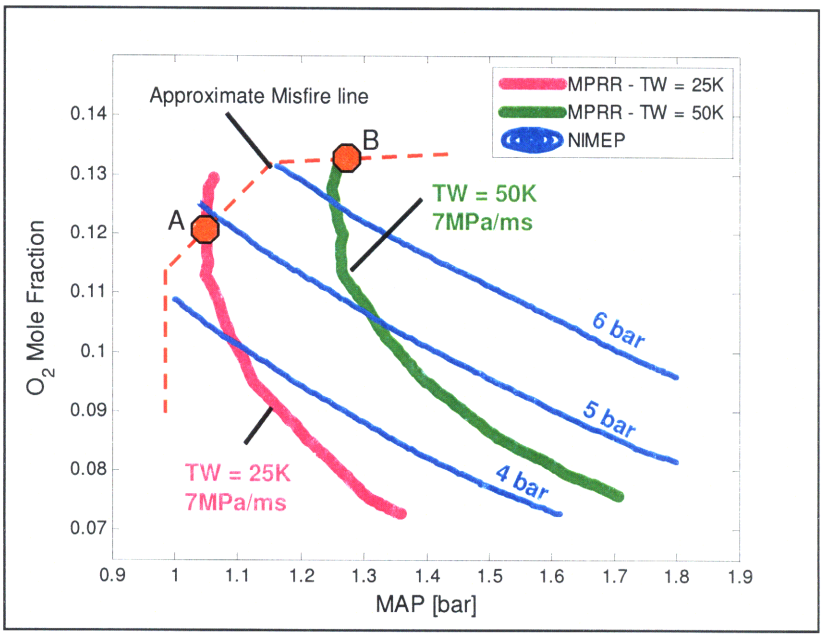

Figure 11.4: Comparison of 7 MPa/ms MPRR contours on a x_{O2} vs. MAP plot for operation with no EGR. MPRR contours calculated using WAVE values in $1/\tau_{reaction}$ correlations from the TW = 50K and TW = 25K 10-zone simulations. $\lambda = 1.00$; $T_{in} = 50°C$.

12 Understanding the effect of external EGR

In Section 9 it was shown that the high load limit always occurs at the misfire limit. It was also shown that any potential benefit of using EGR depends on how addition of EGR affects the misfire limit. It was shown that when 5% EGR was used, the MPRR contours shifted to higher boost pressures but misfire limit shifted to a lower shift oxygen fraction and there was no benefit. While this was very useful in understanding the high load limit, more data is needed to determine if coupling EGR and boosting can be used to extend the high load limit.

To fully examine the relationship between EGR fraction and the high load limit, EGR sweeps were performed over a range of NVO timings for boost pressures of 1.1, 1.3, 1.5, 1.7 bar with the intake temperature fixed at 120°C. For each NVO timing the EGR rate was increased until the engine misfired.

As was discussed in Section 8.2, a real world engine would likely control the intake temperature to more tightly control the CA50 in order to optimize efficiency and achieve low engine NVH. Thus is also important to examine the effect of EGR across several intake temperatures. To accomplish this EGR sweeps were performed over a range of NVO timings for intake temperatures of 60, 90, 120 and 150°C. In these sweeps the intake pressure and exhaust pressure were fixed at 1.5 bar 1.53 bar respectively.

This data was taken with the assistance of Craig Wildman. Mr. Wildman closely examined the parameters affecting the misfire limit as this was a significant portion of his thesis work. In Mr. Wildman's thesis, several empirical relationships based on P_{15BTC}, oxygen fraction and intake temperature were developed using this data. Mr. Wildman's thesis also contains misfire data for operation without EGR.

12.1 EGR sweeps at different boost pressures

The data is explained using a series of contour maps. The vertical axis used to plot these contour maps is the ratio of x_{EGR} to x_{burn}. This is the fraction of total burned gas that is cooled EGR. The horizontal axis is x_{burn}. The misfire points in each plot are indicated with green squares and all other points used to generate the contours are indicated by black circle outlines.

Figure 12.1 shows the MPRR contours at the four boost pressures considered. Notice that the x_{EGR}/x_{burn} misfire profile is different for each pressure. For a given burn fraction, the allowable ratio of EGR to burn gas increases with pressure. The two exceptions to this are the 1.5 bar misfire points at x_{burn} of 0.38 and 0.42. The details of these misfire contours are not explored here as this was not the focus of this work. However it is important to realize that the misfire limit depends on several variables including pressure, temperature, oxygen fraction and fuel fraction.

The 7 MPa/ms contour is indicated for each boost pressure in Figure 12.1. Taking this as the MPRR constraint, the available operating region for each pressure is to the right of this contour. For all four boost pressures the MPRR contours have the same basic trend and slope downward and to the right. This slope occurs because for a given burn fraction, replacing hot trapped residual with cooled EGR (increasing x_{EGR}/x_{burn}) results in a lower mixture temperature prior to combustion. This reduced temperature lengthens the combustion process and thus provides reduced MPRR. This is demonstrated in the enlarged MPRR contour map for 1.5 bar shown in Figure 12.2. Starting at point A with a MPRR of 7 MPa/ms and increasing x_{EGR}/x_{burn} to point B, the MPRR is reduced to 3.5 MPa/ms. Moving along an MPRR contour from point A to point C, the effect of reduced mixture temperature from increased EGR offsets the effect of reduced dilution (increased oxygen fraction). Note that these trends are consistent with the data presented in Section 8.3 which showed for a given burn gas fraction, increasing the EGR content will reduce the MPRR. Note for any burn fraction, the minimum MPRR occurs at the misfire limit where the EGR rate is the highest.

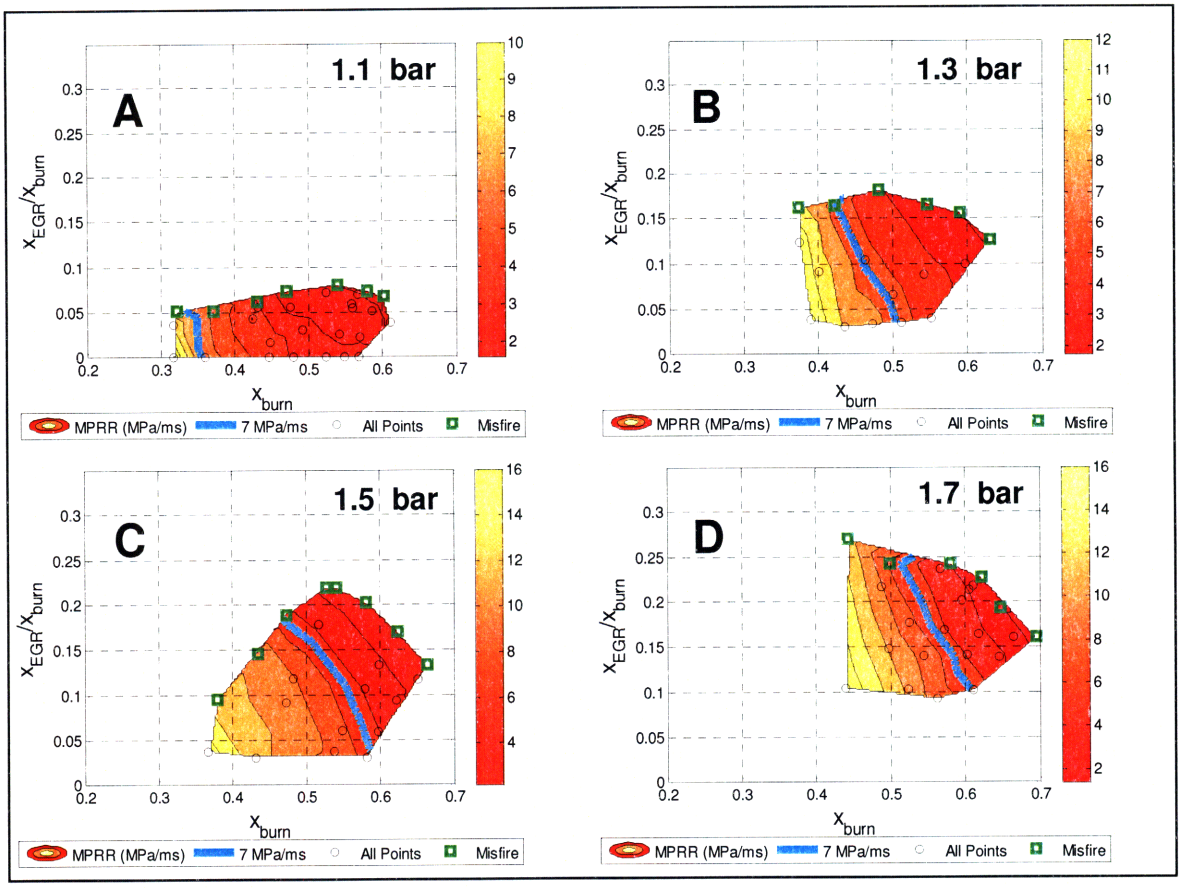

Figure 12.1: MPRR contour maps on a x_{EGR}/x_{burn} versus x_{burn} plot for boost pressures of (A) 1.1 bar, (B) 1.3 bar, (C) 1.5 bar and (D) 1.7 bar. Intake temperature fixed at 120°C.

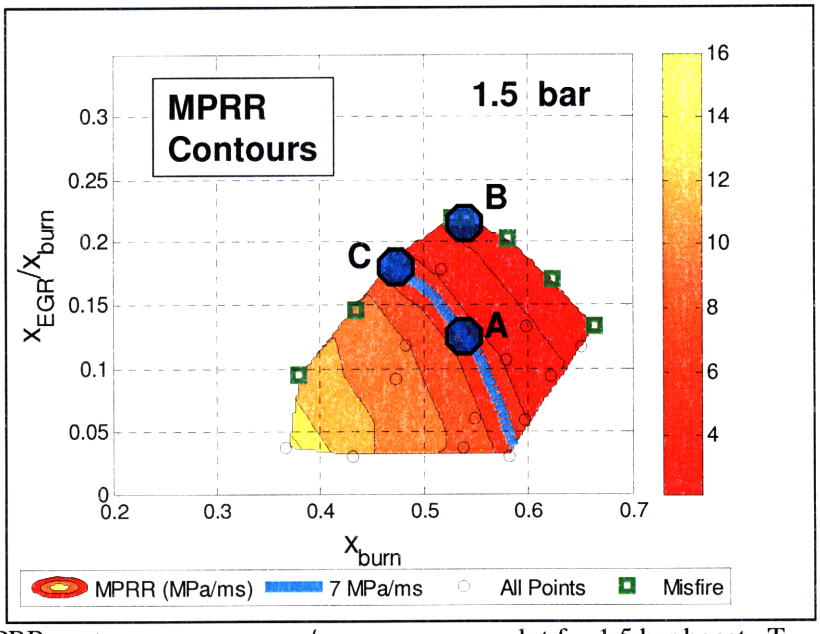

Figure 12.2: MPRR contour map on a x_{EGR}/x_{burn} versus x_{burn} plot for 1.5 bar boost. T_{intake} fixed at 120°C.

Figure 12.3 shows the fuel mass contours and the 7 MPa/ms MPRR contour for the four boost pressures considered. The fuel mass for a given burn fraction changes very little as the EGR rate is increased. However there does appear to be a slight increase in fuel mass as the EGR rate is increased. This is attributed to the reduced mixture temperature that occurs with increased EGR. This reduced mixture temperature allows a slight increase the total in-cylinder mass thus enabling a slight increase in fueling. However as the EGR rate increases, the volume of charge that must be drawn into the engine through valves increases because less burned gas is trapped in-cylinder. For the valve timings and engine speeds considered the effect of increased volume flow appears to lose out to the effect of reduced temperature and the fuel mass increases slightly for increases in EGR rate.

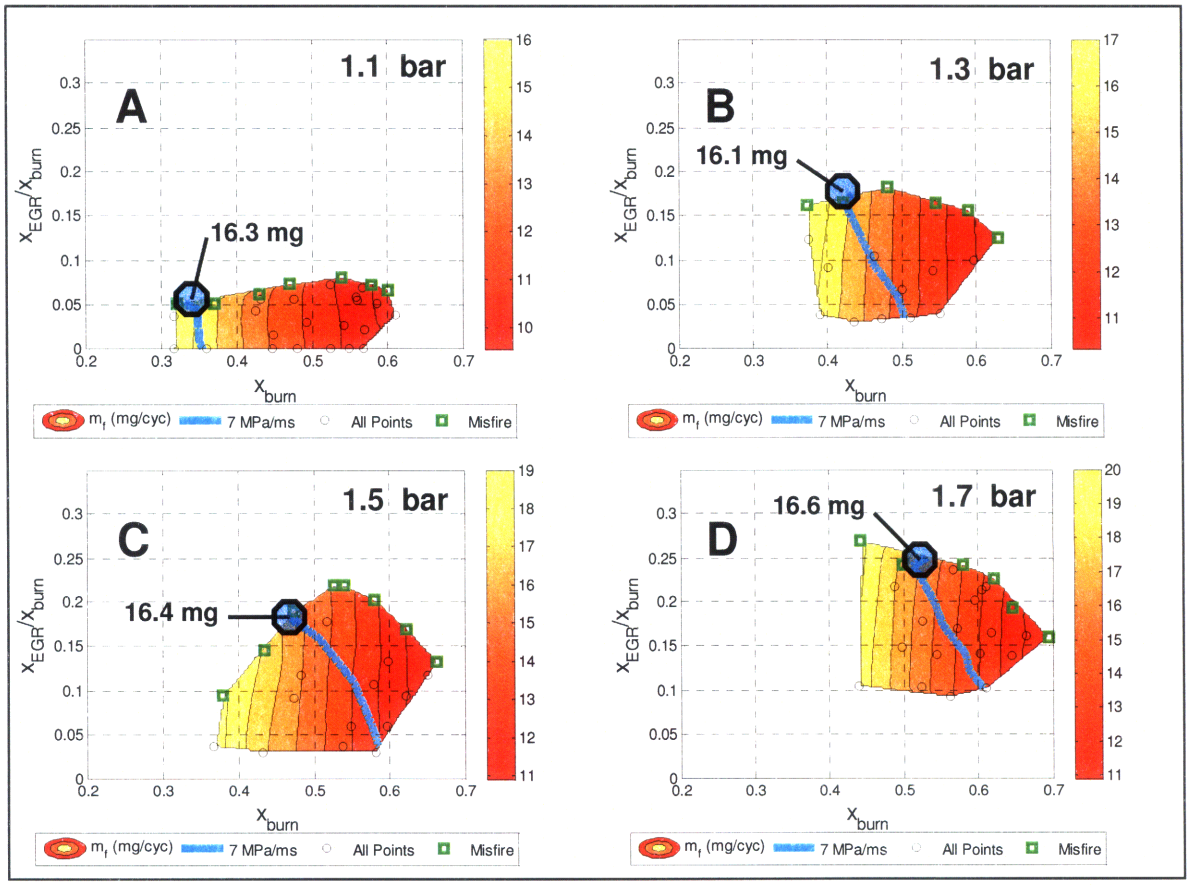

Figure 12.3: Fuel mass contour maps on a x_{EGR}/x_{burn} versus x_{burn} plot for boost pressures of (A) 1.1 bar, (B) 1.3 bar, (C) 1.5 bar and (D) 1.7 bar. Intake temperature fixed at 120°C.

There are several important observations to make from Figure 12.3. Consistent with Section 9, the high load limit always occurs at the misfire limit. The fueling levels at the misfire limit for

the 7 MPa/ms constraint are indicated for each pressure. As can be seen the maximum fueling does not substantially change with pressure. Thus utilizing higher EGR rates to allow operation at higher pressures does not produce any improvement in the high load limit. This is consistent with the data presented in Section 9 for 5% EGR. To demonstrate this, the interpolated values for x_{O2}, MAP and EGR rate at the 7 MPa/ms high load points are used to construct the sketch shown in Figure 12.4. As the figure shows, to maintain a MPRR of 7 MPa/ms, as the pressure is increased higher EGR rates are needed. With increasing EGR rates the oxygen fraction at which the engine misfires falls (meaning that more hot residual is needed for ignition) and the resulting high load limit does not increase.

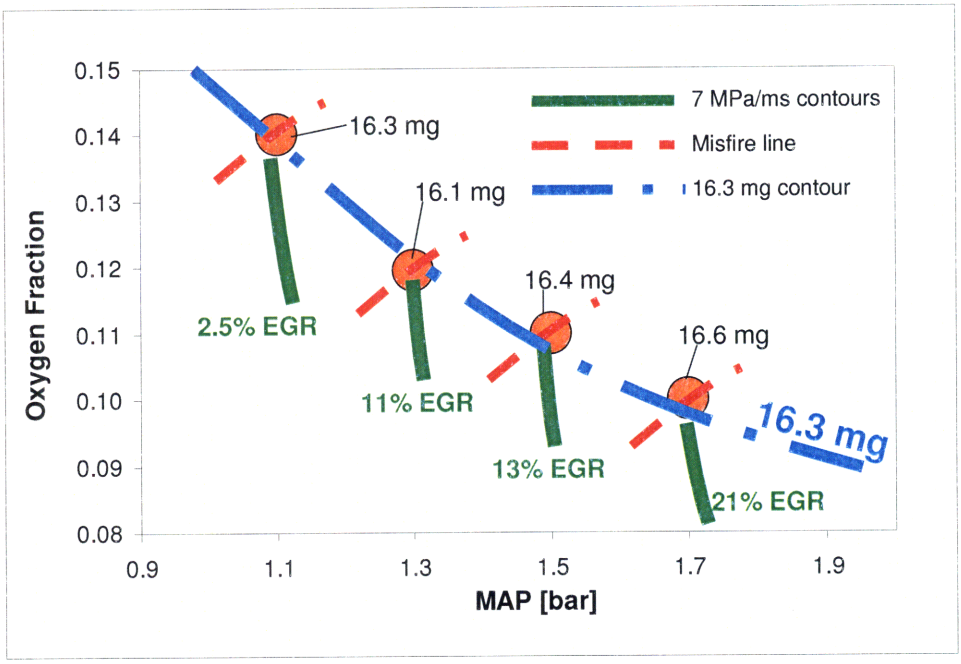

Figure 12.4: Sketch demonstrating the effect of EGR on high load limit. The figure was constructed using interpolated values for x_{O2}, MAP and EGR rate at the 7 MPa/ms high load points in Figure 12.3.

Note that the fuel mass was used here as it does not include the effects of efficiency. The efficiency depends on the combustion duration and phasing as well as the relative ratio of intake to exhaust pressure. Figure 12.5 shows the NIMEP contours for all four boost pressures. The efficiency differs between the different high load fueling points and thus the NIMEP changes slightly between the different pressures.

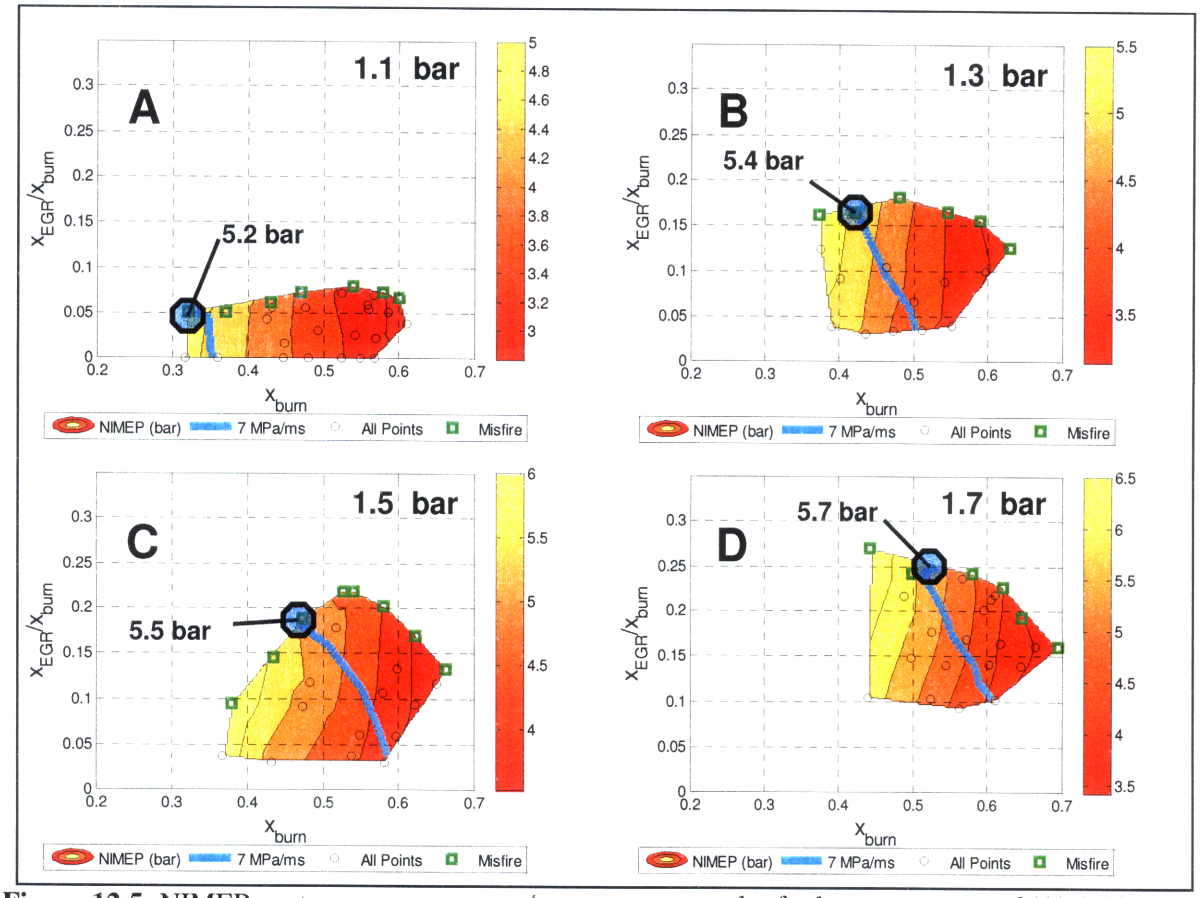

Figure 12.5: NIMEP contour maps on a x_{EGR}/x_{burn} versus x_{burn} plot for boost pressures of (A) 1.1 bar, (B) 1.3 bar, (C) 1.5 bar and (D) 1.7 bar. Intake temperature fixed at 120°C.

Figure 12.6 shows the contours for the estimated temperature at 15° BTC at all four boost pressures. The effect of EGR on temperature is not fully captured with the estimated value for T_{15BTC}. While the estimated T_{15BTC} values do generally decrease with increases in EGR, the temperature reduction is not very strong and for some x_{EGR}/x_{burn} ranges, increases in EGR lead to higher estimated T_{15BTC}. For example, going from point A to point B in Figure 12.7, hot residual is replaced with cool EGR but the estimated T_{15BTC} does not change. In the in the 1.1 and 1.3 bar contour maps the effect of EGR on temperature is very weak. The T_{15BTC} contours for 1.7 bar appear to be the most accurate. The weak temperature dependence in the correlation was a result of this estimation error. Furthermore, as discussed in Section 10, the large improvement in the correlation fit from adding the $1 - x_{EGR}$ term was because this term captured much of the temperature information that was missed by the T_{15BTC} estimate.

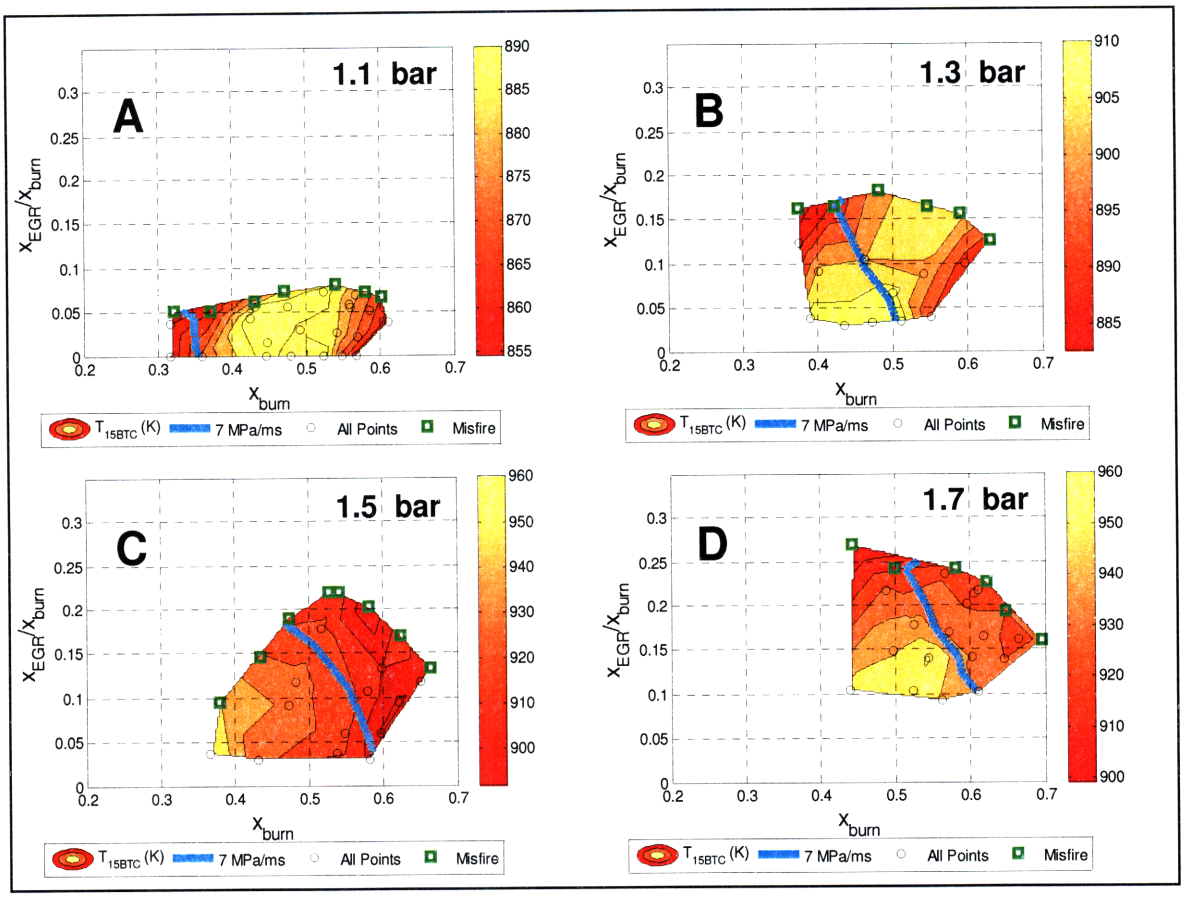

Figure 12.6: T_{15BTC} contour maps on a x_{EGR}/x_{burn} versus x_{burn} plot for boost pressures of (A) 1.1 bar, (B) 1.3 bar, (C) 1.5 bar and (D) 1.7 bar. Intake temperature fixed at 120°C.

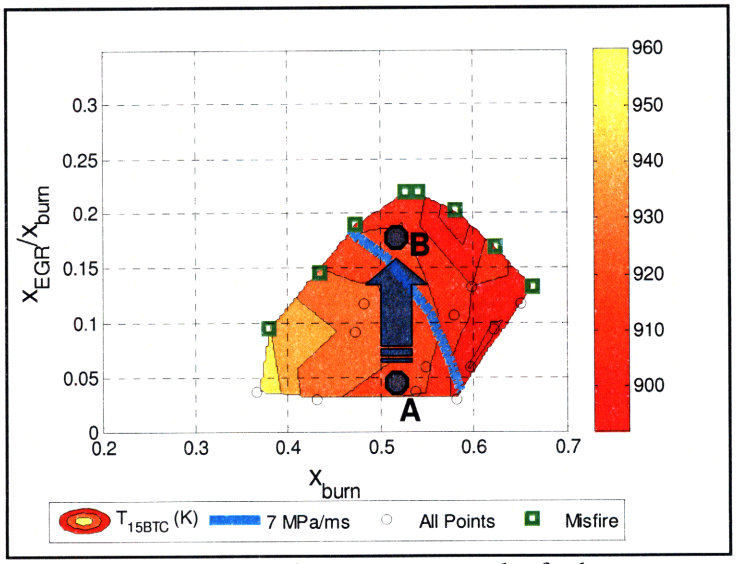

Figure 12.7: T_{15BTC} contour maps on a x_{EGR}/x_{burn} versus x_{burn} plot for boost pressure of 1.5 bar. Intake temperature fixed at 120°C.

The effect of EGR on the CA10 combustion phasing can be used to confirm the error in the estimated T_{15BTC} values. Figure 12.8 shows the CA10 contours for all four boost pressures. For a given burn fraction increases in the EGR rate clearly retard the combustion phasing. As the composition is the same this combustion retard is the result of the reduced bulk temperature that occurs with increased EGR. While the stratification may also change with EGR, these changes will be relatively small and would not produce the strong trends observed. In the next section it is shown that for this engine the stratification changes very little as the EGR rate is increased for a given burn fraction.

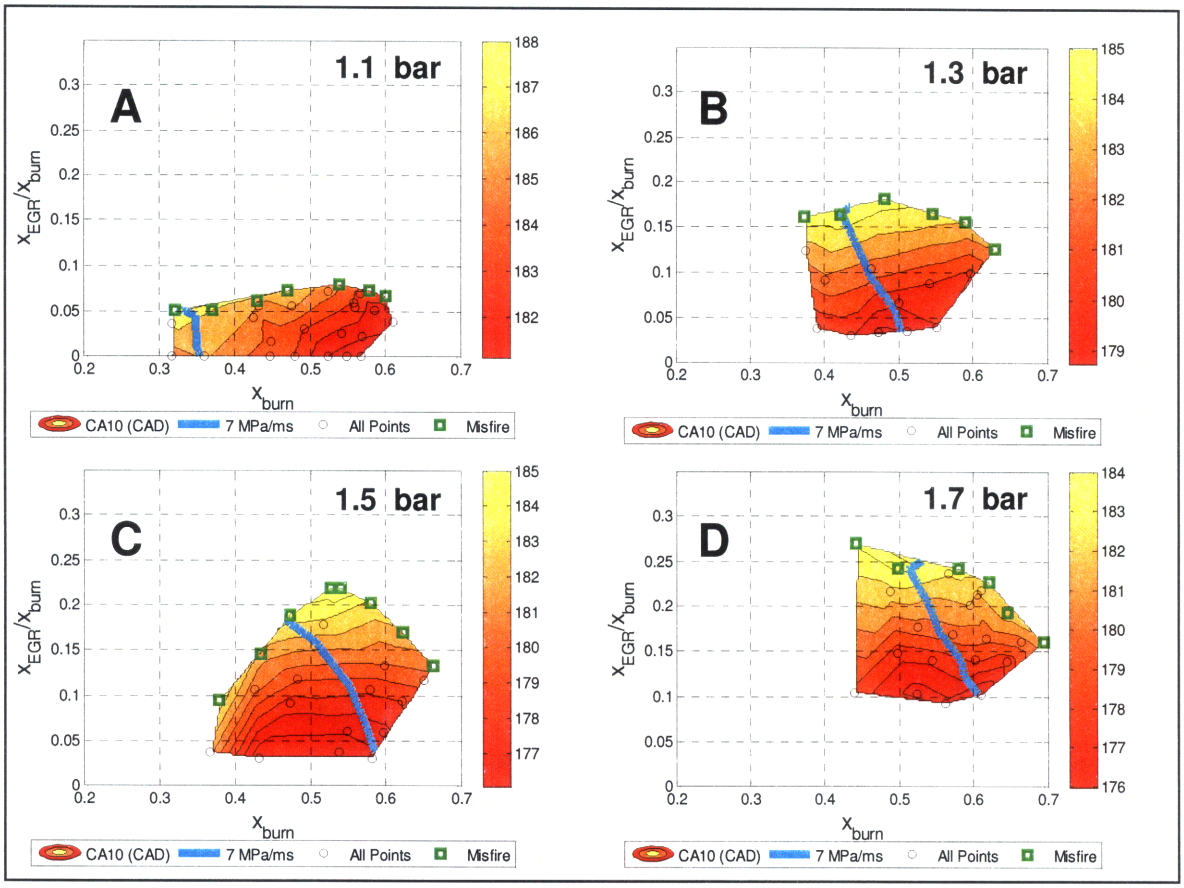

Figure 12.8: CA10 contour maps on a x_{EGR}/x_{burn} versus x_{burn} plot for boost pressures of (A) 1.1 bar, (B) 1.3 bar, (C) 1.5 bar and (D) 1.7 bar. Intake temperature fixed at 120°C.

Figure 12.9 shows the T_{IVO} contours for the four boost pressures. As shown in the contour maps, for a given burn fraction the residual temperature increases with the EGR rate. This is a because of the combustion retard that occurs with increased EGR.

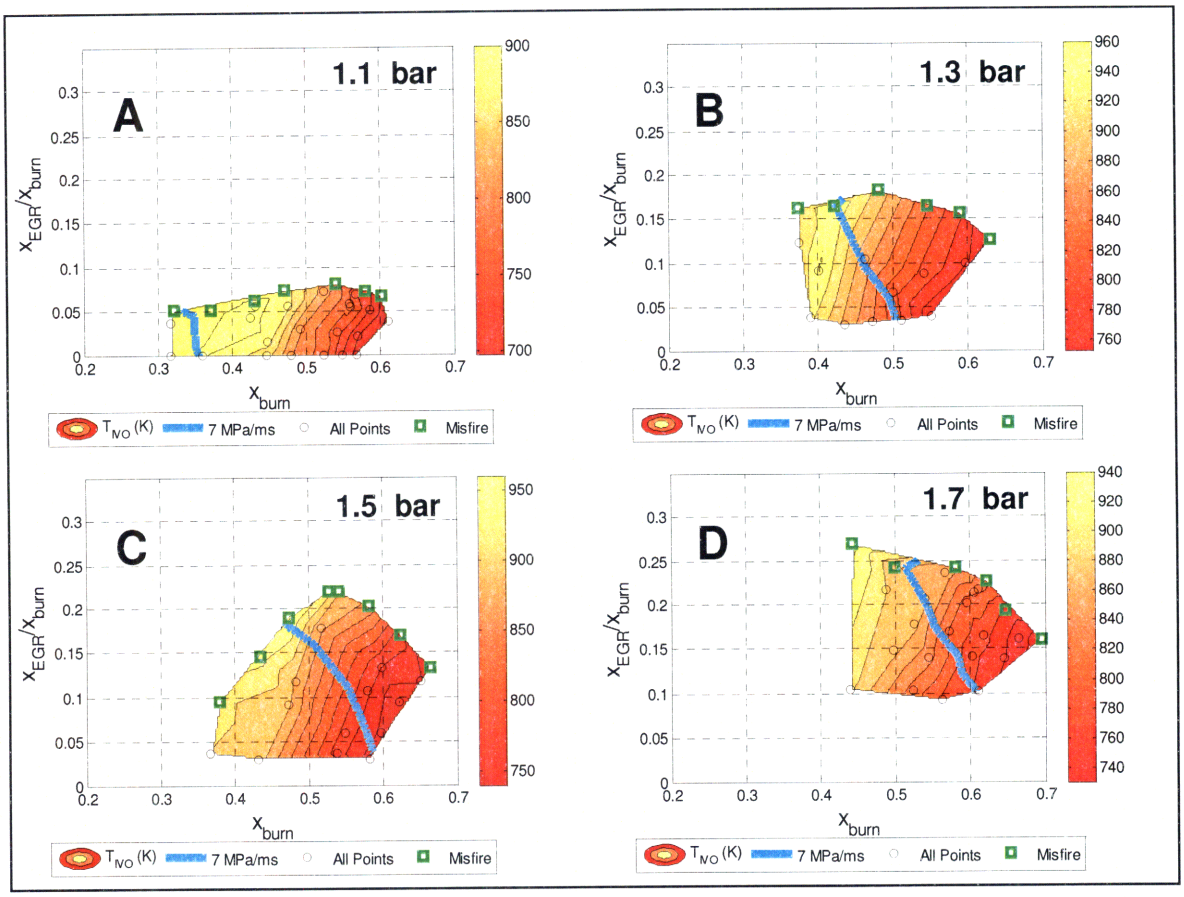

Figure 12.9: T_{IVO} contour maps on a x_{EGR}/x_{burn} versus x_{burn} plot for boost pressures of (A) 1.1 bar, (B) 1.3 bar, (C) 1.5 bar and (D) 1.7 bar. Intake temperature fixed at 120°C.

12.2 EGR sweeps at different intake temperatures

EGR sweeps were performed at intake temperatures of 60, 90, 120 and 150°C for a range of NVO timings with the boost pressure fixed at 1.5 bar. Note that the data presented for 120°C is the same as that presented in Section 12.1 and it is shown here to facilitate comparison with the other intake temperatures. The data is explained using the same type of contour maps used in Seciton 12.1 with the ratio of x_{EGR} to x_{burn} on the vertical axis and x_{burn} on the horizontal axis.

Figure 12.10 shows the MPRR contours at the four intake temperatures considered. The x_{EGR}/x_{burn} misfire profile is different for each intake temperature. The allowable ratio of EGR to burn gas increases with intake temperature.

The 7 MPa/ms contour is indicated for each intake temperature. Using this as the MPRR constraint, the available operating region for each intake temperature is to the right of this contour. Figure 12.11 shows the 7 MPa/ms contours for the four intake temperatures on the

same plot. Notice that slope of the MPRR curve increases as the intake temperature is increased. This is because as the EGR rate is increased for a given burn fraction, hot trapped residual is replaced with cooled EGR. If the intake charge temperature is increased, the temperature of the EGR replacing the trapped residual is increased and the resulting reduction in bulk mixture temperature is less which in turn provides a smaller reduction in MPRR. Thus the slope of the MPRR line becomes steeper as the intake temperature is increased. As a thought experiment consider the case of the intake temperature being higher than the residual temperature, in this scenario replacing trapped residual with EGR would lead to a higher bulk temperature and the MPRR would increase (the MPRR contour would slope upward to the right). For the case of the intake temperature being equal to the trapped residual temperature, ignoring the effect of stratification, the MPRR contour would be vertical such that substituting EGR for trapped residual would have no effect on the MPRR.

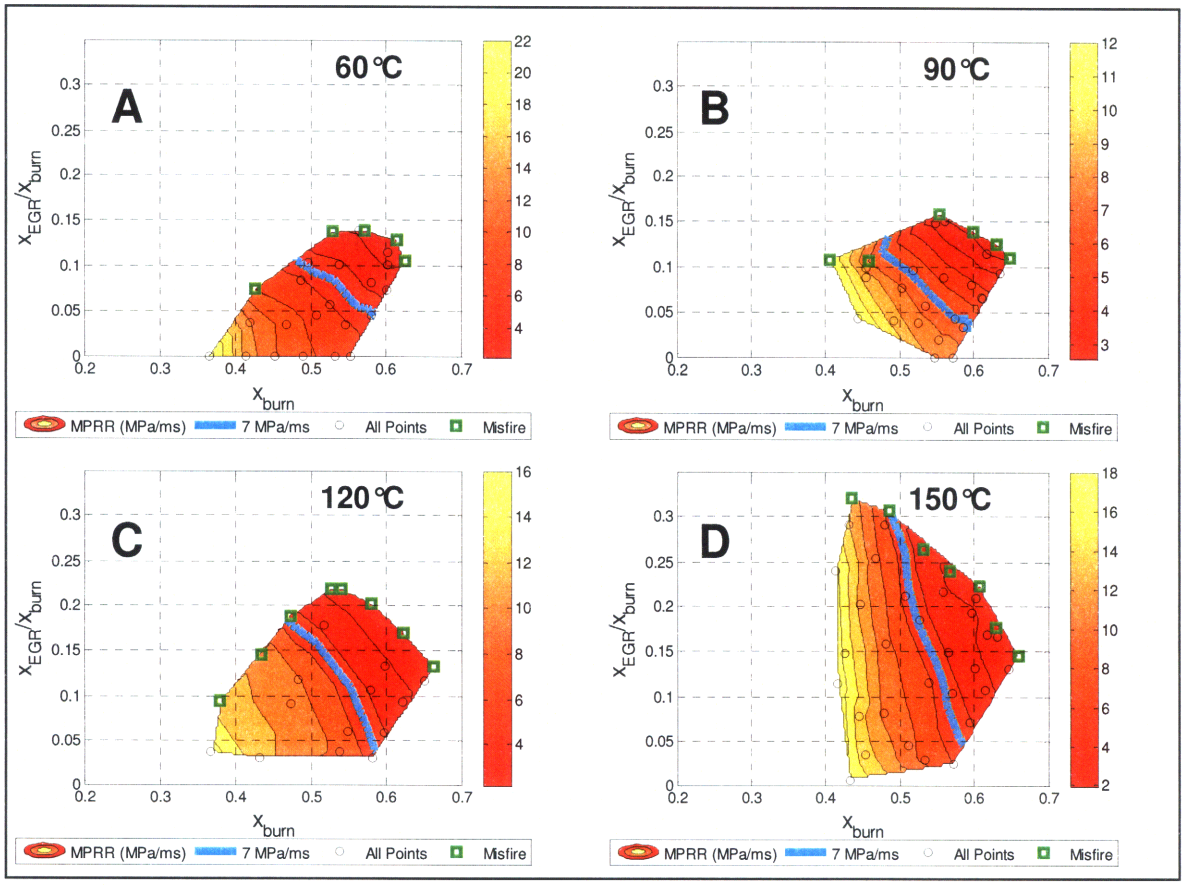

Figure 12.10: MPRR contour maps on a x_{EGR}/x_{burn} versus x_{burn} plot for intake temperatures of (A) 60°C, (B) 90°C, (C) 120°C and (D) 150°C. Boost pressure fixed at 1.5 bar.

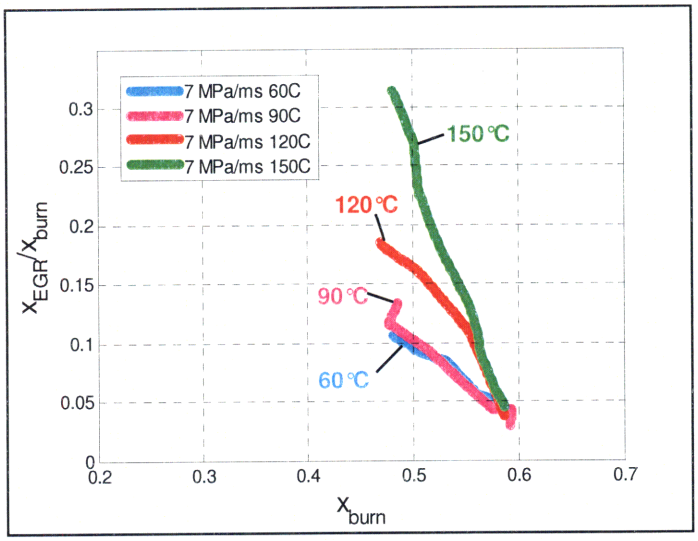

Figure 12.11: 7 MPa/ms contours for T_{intake} of 60, 90, 120 and 150°C. Boost pressure fixed at 1.5 bar.

Also notice from Figure 12.10 and Figure 12.11, that for a given burn fraction and EGR rate, increasing the intake temperature leads to a higher pressure rise rate. This is consistent with the temperature sweep data discussed in Section 8.2.

Figure 12.12 shows the fueling contours at the four intake temperatures considered. The high load limit for the 7 MPa/ms constraint occurs at the misfire limit and the value for each intake temperature is indicated on maps. As can be seen, the fueling at the high load limit is essentially the same for all four intake temperatures. Also note that the fueling at a given burn fraction does not change much with intake temperature, thus the burn fraction at high load misfire point is roughly the same for all four intake temperatures.

For a given burn fraction (oxygen fraction), the pressure prior to ignition at the misfire limit does not change significantly with intake temperature as shown by Figure 12.13. Thus ignoring any changes in stratification, for a given burn fraction (constant composition) the mixture temperature prior to ignition at the misfire limit should be the same for the different intake temperatures. That is for a given burn fraction and ignoring any effects from stratification, increases in intake temperature should allow the EGR rate to be increased such that the mixture temperature at the misfire limit is the same. Figure 12.14 shows estimated temperature 15° BTC as function of the burn fraction for the misfire points at all four intake temperatures. With the exception of the two circled points, for a given burn fraction, the estimated T_{15BTC} value at the misfire limit is roughly the same for the four different intake temperatures.

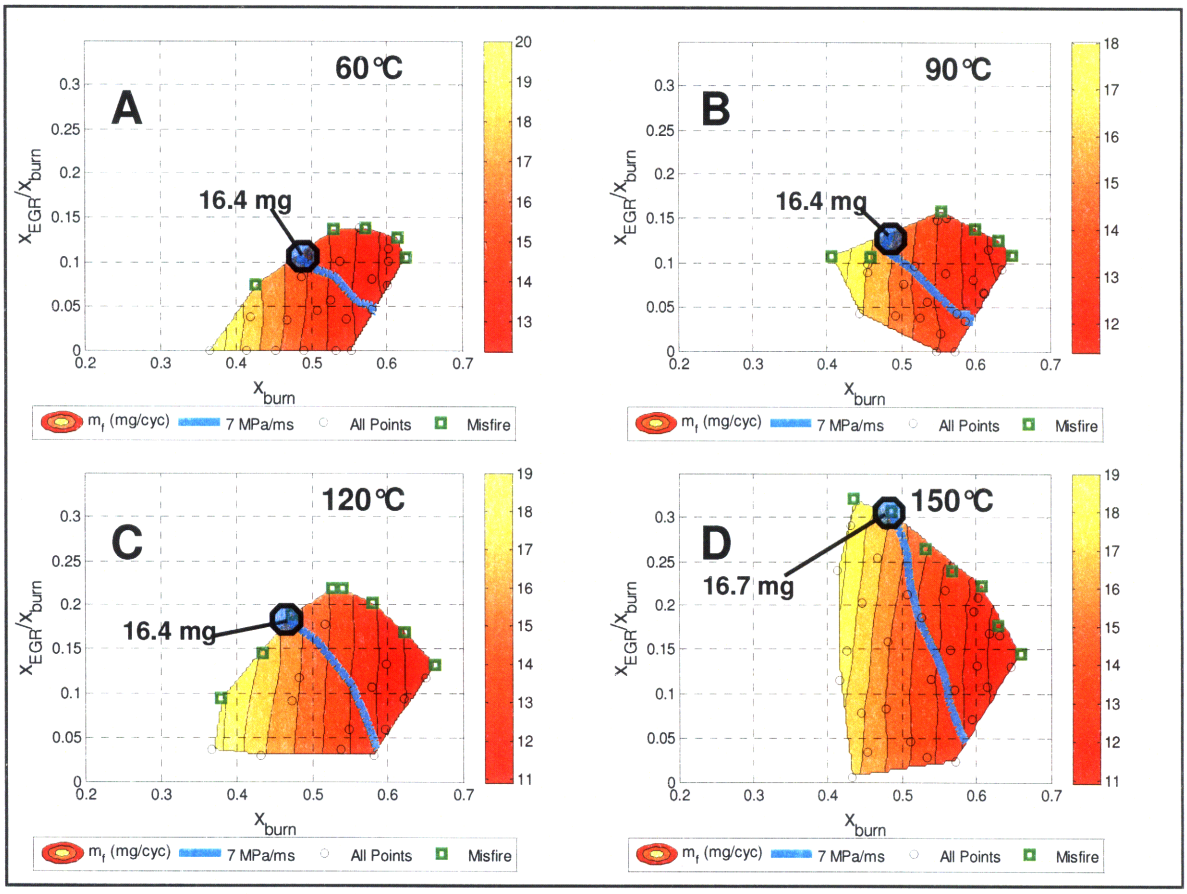

Figure 12.12: Fuel mass contour maps on a x_{EGR}/x_{burn} versus x_{burn} plot for intake temperatures of (A) 60°C, (B) 90°C, (C) 120°C and (D) 150°C. Boost pressure fixed at 1.5 bar.

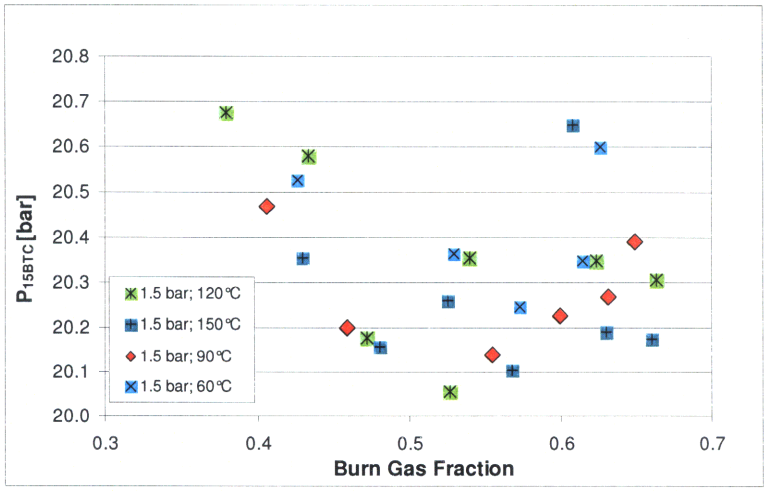

Figure 12.13: P_{15BTC} at the misfire limit versus Burn Fraction for T_{intake} of 60, 90, 120 and 150°C. Boost pressure fixed at 1.5 bar.

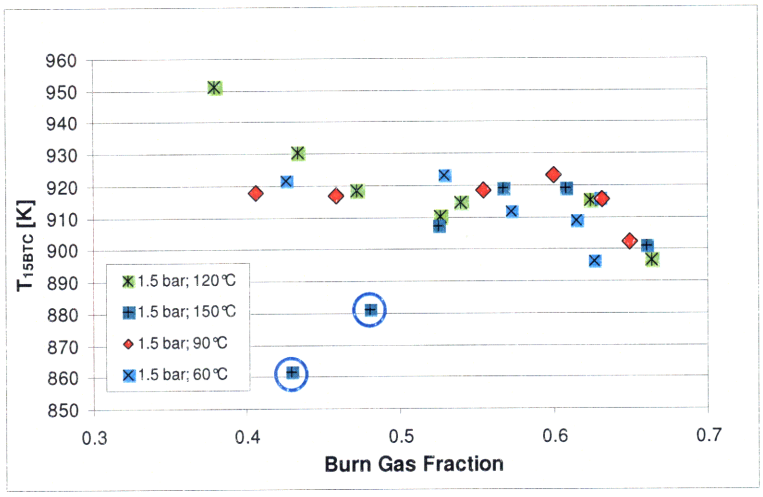

Figure 12.14: T_{15BTC} at the misfire limit versus Burn Fraction for T_{intake} of 60, 90, 120 and 150°C. Boost pressure fixed at 1.5 bar.

The two circled points in Figure 12.14 are shown to be the result of inaccuracies in the estimated T_{15BTC}. The CA10 combustion phasing can be used to explore the error in the estimated T_{15BTC} values. As shown by Figure 12.13, for a given burn fraction, the measured P_{15BTC} at the misfire limit does not change significantly with intake temperature. Thus for a given burn fraction and ignoring any stratification effects, any differences in the CA10 phasing must be driven by temperature. Figure 12.15 shows the CA10 timing for the misfire points as a function of the burn fraction. As can be seen for a given burn fraction the CA10 phasing is approximately equivalent for the four intake temperatures. This implies that the outlier T_{15BTC} points in Figure 12.14 were the result of inaccuracies in the temperature estimate.

It is important to realize that Figure 12.14 and Figure 12.15 collectively show that the effect of EGR is primarily to reduce the mixture temperature and this temperature effect dominates any changes in stratification. Thus for a given burn gas fraction and boost pressure, increases to the intake temperature allow the EGR rate to increased so that the mixture temperature at the misfire limit is the same. Thus for this engine, replacing hot residual with EGR primarily affects the bulk temperature and there are no significant effects from altered stratification.

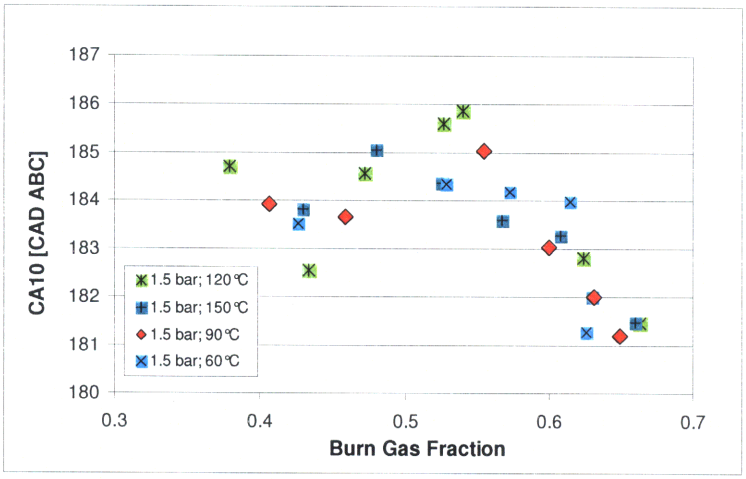

Figure 12.15: CA10 at the misfire limit versus Burn Fraction for T_{intake} of 60, 90, 120 and 150°C. Boost pressure fixed at 1.5 bar.

Figure 12.16 shows the NIMEP contours at all four intake temperatures. As the combustion phasing is the same at each misfire point, the efficiency does not change between the points and the NIMEP for all four pressures are roughly the same.

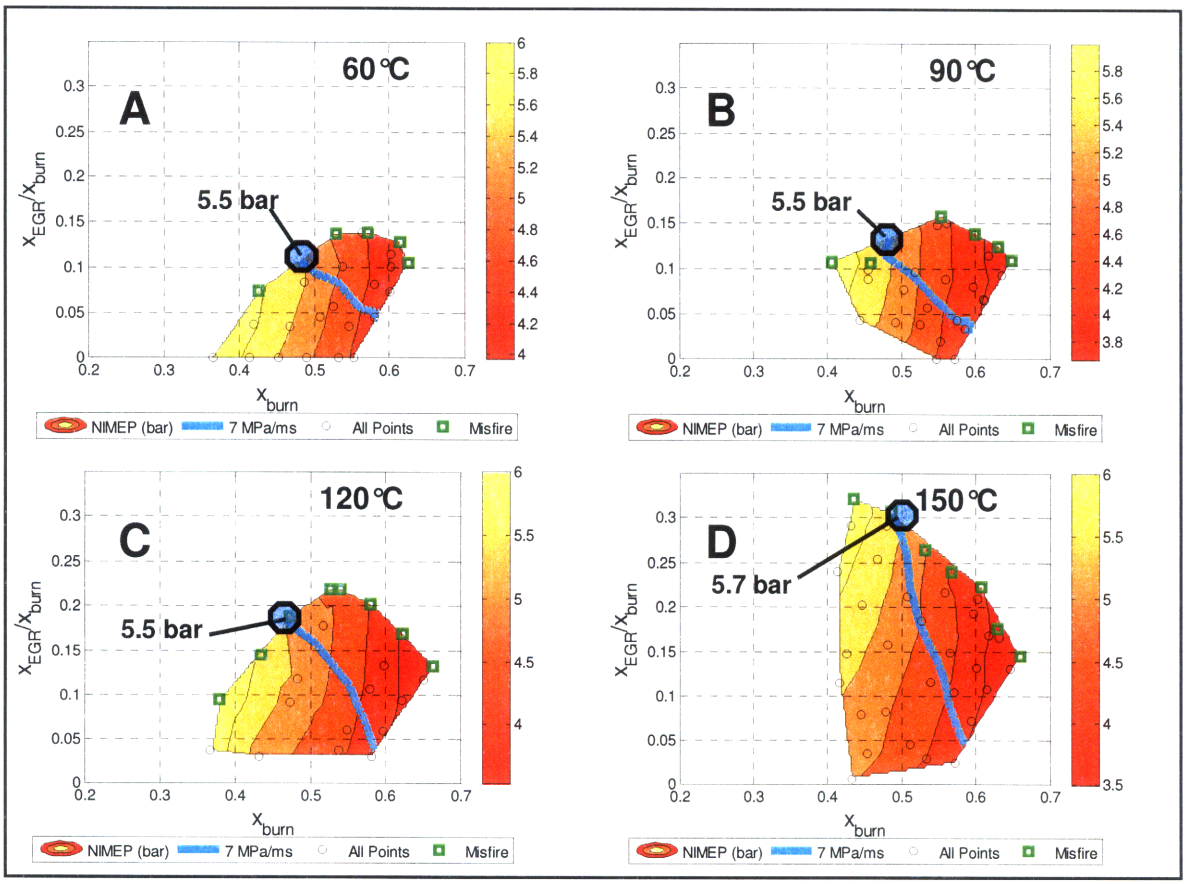

Figure 12.16: NIMEP contour maps on a x_{EGR}/x_{burn} versus x_{burn} plot for intake temperatures of (A) 60°C, (B) 90°C, (C) 120°C and (D) 150°C. Boost pressure fixed at 1.5 bar.

Figure 12.17 shows the T_{15BTC} contours on the x_{EGR}/x_{burn} versus x_{burn} plot. As discussed before the effect of EGR on temperature is not fully captured with the estimated value for T_{15BTC}. While the estimated T_{15BTC} values do generally decrease with increases in EGR, over some x_{EGR}/x_{burn} intervals T_{15BTC} increases with increasing EGR. This inaccuracy in the estimated T_{15BTC} is confirmed with the CA10 contours shown in Figure 12.18.

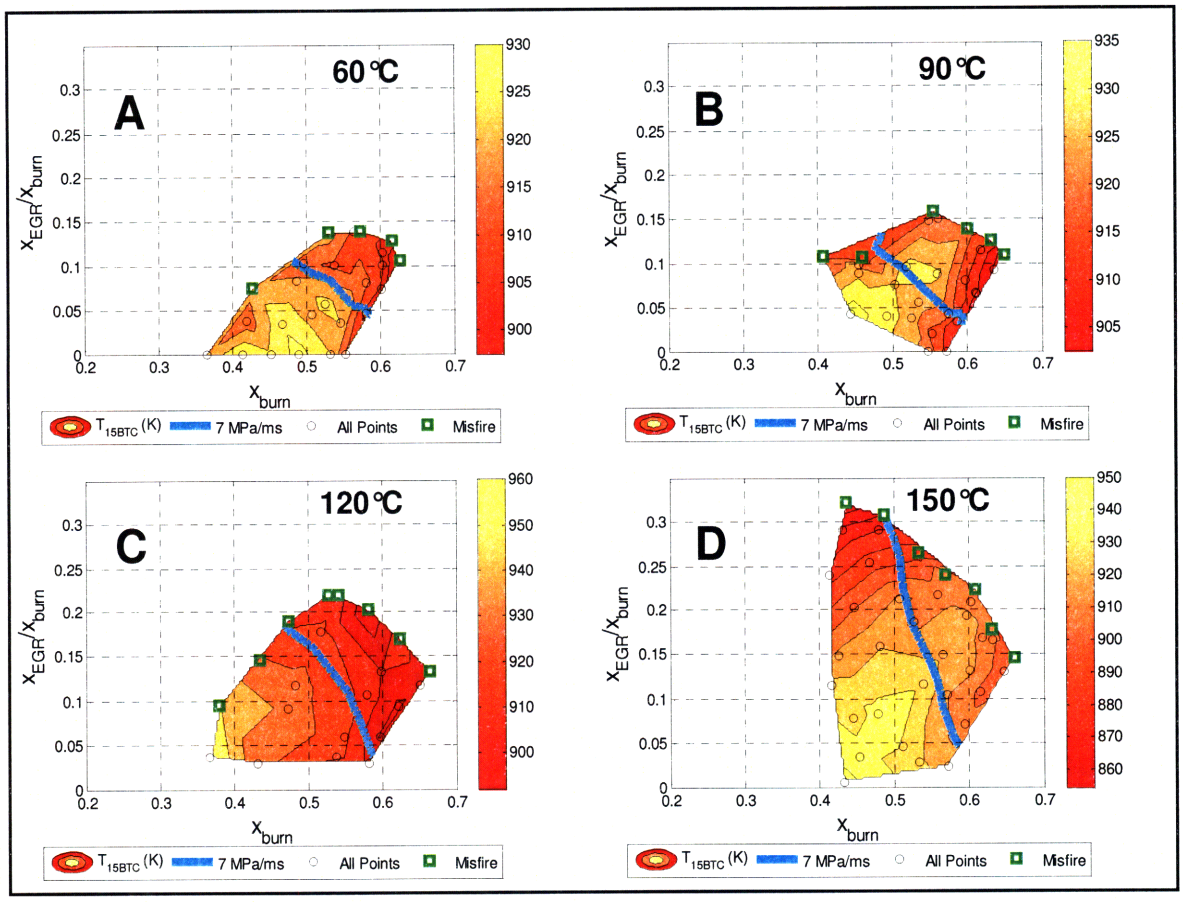

Figure 12.17: T_{15BTC} contour maps on a x_{EGR}/x_{burn} versus x_{burn} plot for intake temperatures of (A) 60°C, (B) 90°C, (C) 120°C and (D) 150°C. Boost pressure fixed at 1.5 bar.

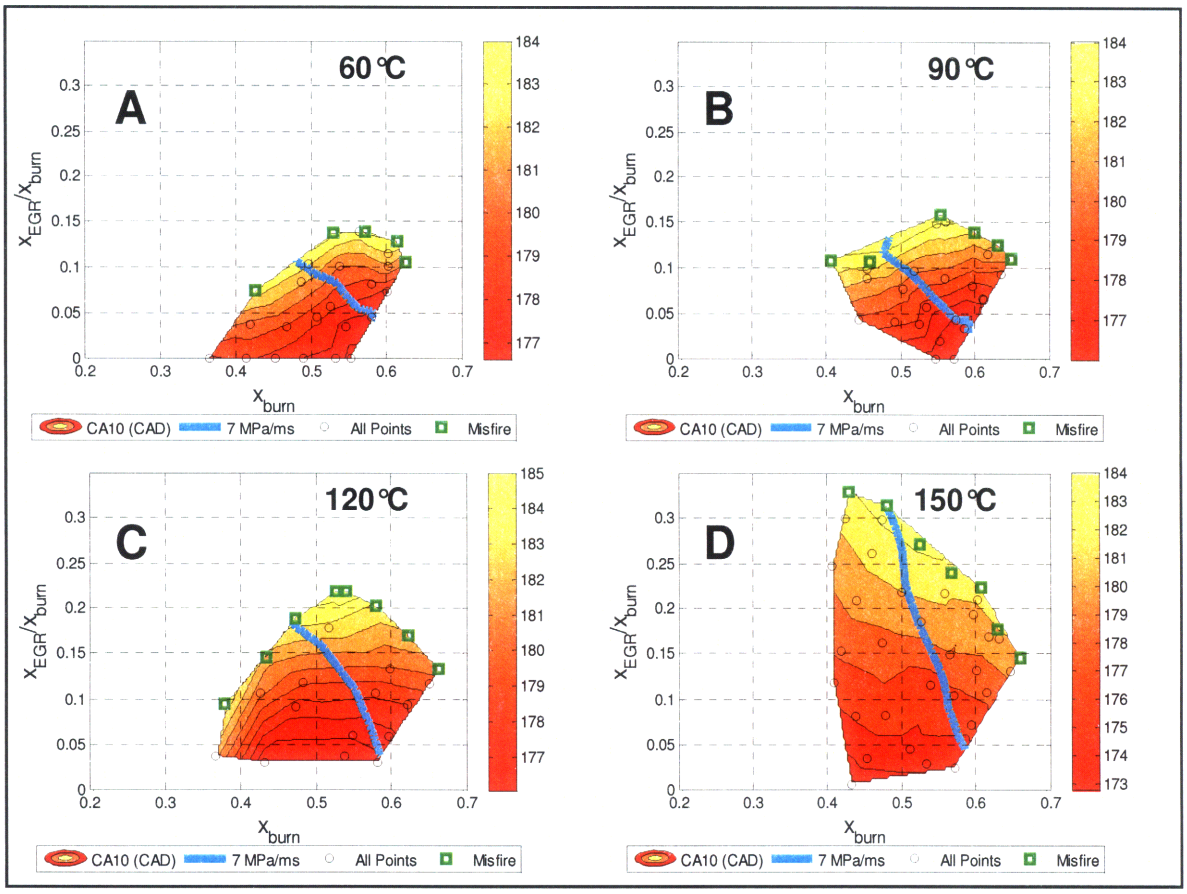

Figure 12.18: CA10 contour maps on a x_{EGR}/x_{burn} versus x_{burn} plot for intake temperatures of (A) 60°C, (B) 90°C, (C) 120°C and (D) 150°C. Boost pressure fixed at 1.5 bar.

12.3 Summary of EGR sweeps

The EGR sweeps again showed that the high load limit always occurs at the misfire limit. The EGR sweeps performed at four different pressure pressures showed that while increased EGR can be used to allow operation at higher pressures, the misfire limit also shifts and there is no net improvement in the high load limit.

The EGR sweeps performed at different intake temperatures demonstrated that the changes to the intake temperature simply changed the amount of allowable EGR at the misfire limit such that for a given burn fraction, the temperature at the misfire limit was the same for all intake temperatures. These results implied that for this test engine the effect of EGR on stratification was minimal.

Figure 12.19 plots the MPRR as a function of the fuel mass for all the misfire points obtained. As can be seen, for a given MPRR constraint, the maximum fueling is roughly the same for all pressures and intake temperatures. Figure 12.20 shows the MPRR as a function of the NIMEP for all the misfire points. The changing efficiency leads to slight differences between the different pressures.

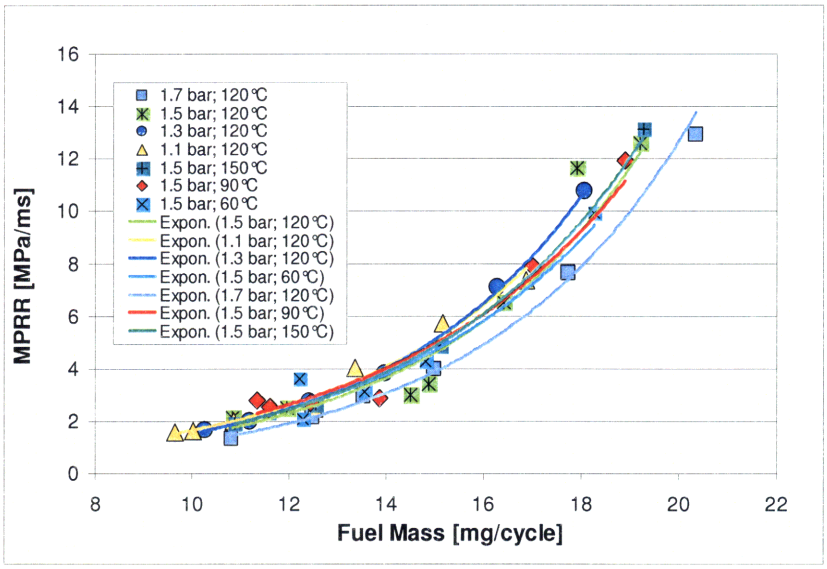

Figure 12.19: MPRR versus the Fuel Mass for all the misfire points obtained in the EGR sweeps.

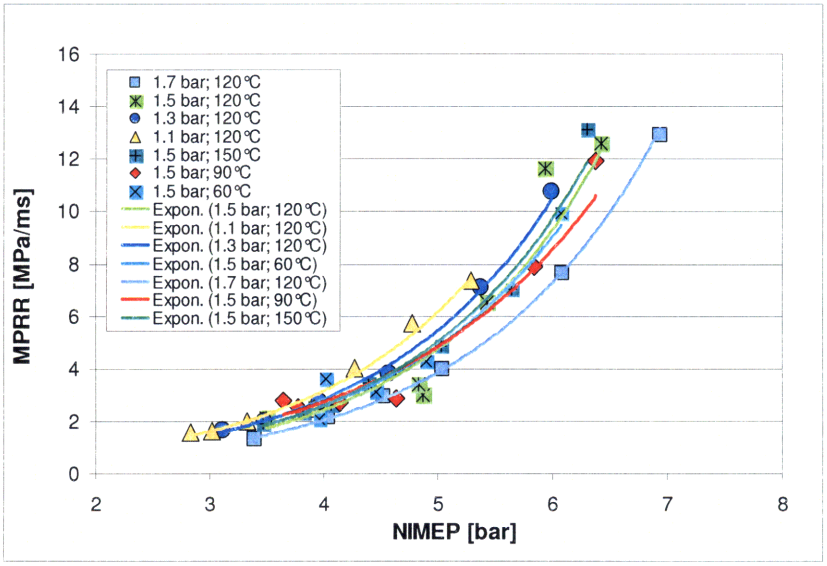

Figure 12.20: MPRR versus NIMEP for all the misfire points obtained in the EGR sweeps.

13 Conclusions

In this study a broad matrix of measured data was used to understand the HCCI high load limit. The data set included sweeps of trapped residual, external EGR, lambda, pressure and intake temperature. Additionally a 10-zone model was utilized to confirm the findings and examine the potential of thermal stratification.

The major contributions of this work are summarized:

1. A relationship for the maximum pressure rise rate was derived using the first law of thermodynamics. This relationship was confirmed across the entire data set. The relationship is given by:

$$MPRR = \frac{1}{\tau_{reaction}} \frac{(\gamma - 1) m_{fuel} LHV}{V(\theta_{MPRR})} \approx \frac{1}{BD_{10-90\%}} \frac{(\gamma - 1) m_{fuel} LHV}{V_{CA50}}$$

   This relationship shows that the metric to focus on for extending the high load limit is the burn duration. It was demonstrated that direct effect of V_{CA50} and γ changes are insignificant compared with the large changes possible for the burn duration.

2. EGR and excess air were examined as potential diluents to mitigate high MPRR. It was shown that for operation with a fixed intake temperature, increasing the EGR fraction for a given load provides reduced pressure rise rates. The benefit was due to the effect of EGR on the mixture temperature.

   Operation with excess air also provided reduced mixture temperature. However for excess air, the effect of reduced mixture temperature was overridden by the increased oxygen fraction. Thus for a given load, operating with excess air increased the pressure rise rate. This is an important result and indicates that dilution should be achieved with burned gas and not excess air. Also note that operation with excess air prevents the use of the 3-way catalyst.

3. The nature of the high load limit was determined. For MPRR constrained operation the high load limit always occurs at the misfire limit. Thus for a given NIMEP, the lowest MPRR is achieved at the lowest possible boost pressure that can be reached without misfiring.

4. A correlation was developed for $1/\tau_{reaction}$ using the P_{15BTC}, T_{15BTC}, x_{O2} and x_{fuel} with the form based loosely on the binary collision model. Using the entire data set, an R^2 of 0.73 was

achieved. The error was attributed primarily to stratification variations and scatter in the estimated value for T_{15BTC}. The scatter in the estimated T_{15BTC}, resulted in a weak dependence on temperature. Terms were then added to the model to better capture the stratification and mixture temperature and an R^2 of 0.89 was achieved.

5. The form of the $1/\tau_{reaction}$ correlation was confirmed using a 10-zone combustion simulation. A matrix of 10-zone simulations were performed at three different stratification settings. The $1/\tau_{reaction}$ temperature dependence was much stronger for the simulation based correlation.

6. A broad base of EGR sweeps were performed to examine the potential using EGR to allow operation at higher pressures. While increased EGR can be used to allow operation at higher boost, the misfire limit also shifts and there is no net improvement in the high load limit.

7. EGR sweeps were performed at different intake temperatures and used to demonstrated for a given boost pressure and burn fraction, the changes to the intake temperature simply changed the amount of allowable EGR at the misfire limit such that mixture temperature at the limit did not change with intake temperatures. Thus for a given burn fraction, the effect of increasing the intake temperature was to reduce the level of EGR at the misfire limit such that the mixture temperature at the limit did not change. These results showed that for this test engine the effect of EGR was primarily on the mixture temperature and any effects of EGR on stratification were minimal.

8. The $1/\tau_{reaction}$ correlations for the two different temperature stratifications were used to examine effect of thermal stratification on the high load limit. The estimated improvement was 30% however this improvement depends on the location of the misfire limit.

14 References

[1] Haraldsson, G., Tunestal, P., Johansson, B., Hyvonen, J., "HCCI closed-loop combustion control using fast thermal management", SAE paper 2004-01-0943, 2004.

[2] Christensen M., Hultqvist, A., Johansson, B., "Demonstrating the Multi-Fuel Capability of a Homogeneous Charge Compression Ignition Engine with Variable Compression Ratio", SAE paper 1999-01-3679, 1999.

[3] Zhao, H., Li, J., Ma, T., Ladommatos, N., "Performance and analysis of a 4-stroke multi-cylinder gasoline engine with CAI combustion", SAE paper 2002-01-0420, 2002.

[4] Santoso, H., et al., "Managing SI/HCCI Dual-Mode Engine Operation" SAE paper 2005-01-0162, 2005.

[5] Koopmans, L., Strom, H., Lundgren, S., Backlund, O., Denbratt, I., "Demonstrating a SI-HCCI-SI mode change on a Volvo 5- cylinder electronic valve control engine" SAE paper 2003-01-0753, 2003.

[6] Yasuhiro, U., et al., "A study of gasoline-fuelled HCCI engine equipped with an electromagnetic valve train" SAE paper 2004-01-1898, 2004.

[7] Yap, D., et al., "Applying boosting to gasoline HCCI operating with residual gas trapping" SAE paper 2005-01-2121, 2005.

[8] Bell, C., "Maximum Boost", Cambridge MA: Bentley Publishers, 1997.

[9] Chevron Phillips UTG-91 fuel specifications

[10] Crouse, W., et al. "Automotive Mechanics", New York: McGraw-Hill, 2002.

[11] Heywood, J.B., "Internal Combustion Engine Fundamentals", New York: McGraw-Hill, 1988.

[12] J. A. Eng, "Characterization of Pressure Wave Oscillation in HCCI Combustion," SAE Paper 2002-01-2859, 2002.

[13] Tanaka, S., et al., "Two-stage ignition in HCCI combustion and HCCI control by fuels and additives", Combustion and Flame, Volume 132 (219-239), 2003.

[14] Tanaka, S., et al., "A reduced chemical kinetic model for HCCI combustion of primary reference fuel in a rapid compression machine," Combustion and Flame, Volume 133 (467-481), 2003.

[15] Dec, J., et al., "An Investigation of Thermal Stratification in HCCI Engines Using Chemiluminescence Imaging", SAE paper 2006-01-1518, 2006.

[16] Hultqvist, A., et al., "The HCCI combustion process in a single cycle~High-Speed fuel tracer LIF and chemiluminescence imaging", SAE paper 2002-01-0424, 2002.

[17] He, X., et al., "An experimental and modeling study of iso-octane ignition delay times under homogeneous charge compression ignition", Combustion and Flame, Volume 142 (266-275), 2005.

[18] Sjoberg, M., et al., "Potential of Thermal Stratification and Combustion Retard for Reducing Pressure-Rise Rates in HCCI Engines, Based on Multi-zone Modeling and Experiments", SAE paper 2005-01-0113, 2005.

[19] Herold, R.E., et al., "Investigations into the Effects of Thermal and Compositional Stratification on HCCI Combustion - Part II: Optical Engine Results", SAE paper 2009-01-1106, 2009.

[20] Kakuho A., et al., "In-Cylinder Temperature Distribution Measurement and its Application to HCCI Combustion", SAE paper 2006-01-1202, 2006.

[21] Babajimopoulos, A., et al., "An approach for modelling the effects of gas exchange processes on HCCI combustion and its application in evaluating variable valve timing control strategies", SAE paper 2002-01-2829, 2002.

[22] Babajimopoulos, A., et al., "Modeling HCCI Combustion with High Levels of Residual Gas Fraction – A Comparison of Two VVA Strategies", SAE paper 2003-01-3220, 2003.

[23] "Fuel unmixedness effects in a gasoline homogeneous charge compression ignition engine" Vol 8 No 3 2007

[24] Cambustion NDIR 500 Fast CO/CO_2 Manual, Version 1.16, 2004.

Appendix A: Adiabatic mixing

As described in Section X, the effect of composition stratification was examined for one set of 10-zone simulations. This composition stratification was determined by assuming adiabatic mixing between the fresh charge and trapped residual. Thus for a given zone the temperature can be determined by:

$$T_i = T_{cool} \cdot \left(1 - x_{trap,i}\right) + T_{hot} \cdot x_{trap,i} \tag{A.1}$$

In this work the trapped gas was assumed to have a constant temperature (T_{hot}) of 700K. This simplified the calculation however it is important to note that the burned gas temperature will change with timing and load. Thus for a given zone temperature (T_i), the trapped fraction can be computed from the fresh charge temperature (T_{cool}) and the trapped gas temperature (T_{hot}):

$$x_{trap,i} = \frac{T_i - T_{cool}}{T_{hot} - T_{cool}} \tag{A.2}$$

The EGR fraction for zone *i* is given by:

$$x_{EGR,i} = EGR \cdot x_{cool,i} = EGR \cdot \left(1 - x_{trap,i}\right) \tag{A.3}$$

Thus the total burn gas fraction for zone *i* can be computed with:

$$x_{burn,i} = x_{trap,i} + x_{EGR,i} = \left(\frac{T_i - T_{cool}}{T_{hot} - T_{cool}}\right) \cdot \left(1 - EGR\right) + EGR \tag{A.4}$$

The residual gas was assumed to contain only the products of complete combustion. Thus all the fuel in each zone comes from the fraction of fresh charge in that zone. That is the higher temperature zones contain more hot residual and thus less fuel. The fresh charge was assumed to be well mixed and the fuel-air ratio of the fresh charge was constant. Note that for lean operation the trapped residual contains excess air thus lambda is not constant across the zones for lean operation.

Appendix B: Stoichiometric NVO sweeps at 60°C and 90°C

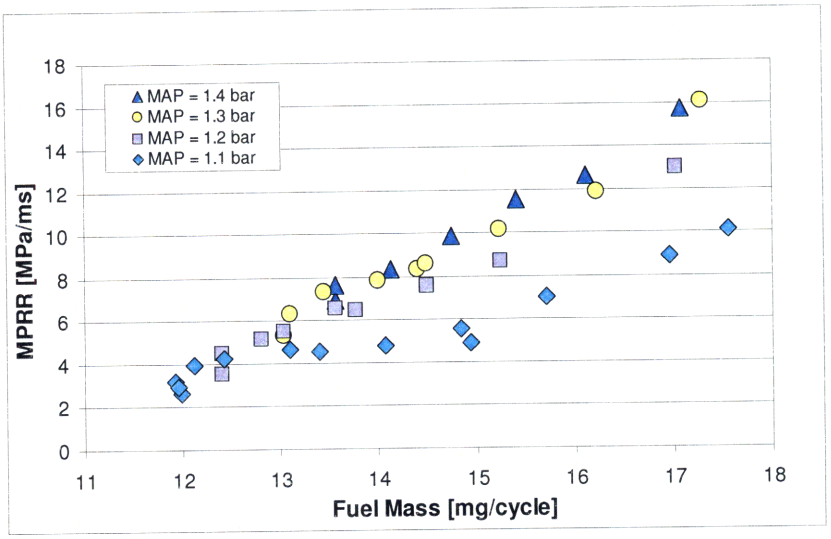

Figure B.1: MPRR versus the fuel mass for several boost levels. All points had stoichiometric fueling, no external EGR and an intake temperature of 90°C.

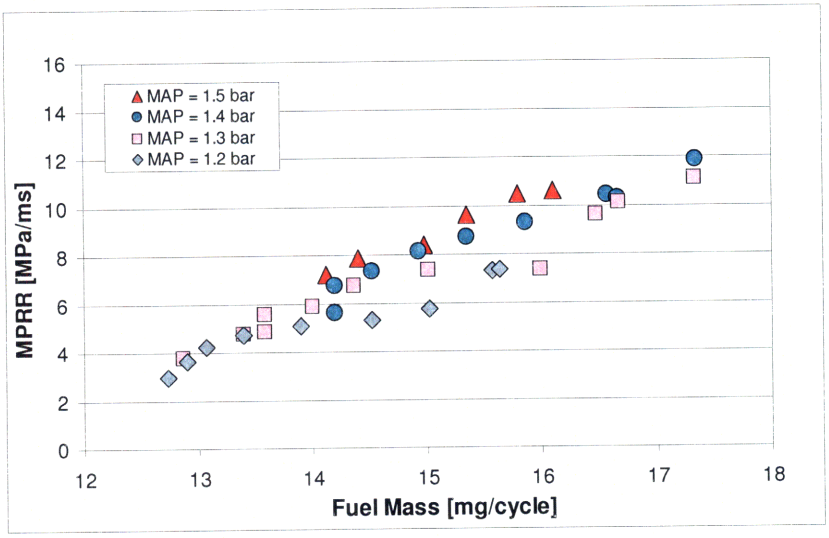

Figure B.2: MPRR versus the fuel mass for several boost levels. All points had stoichiometric fueling, no external EGR and an intake temperature of 60°C.

Appendix C: Dilution: 10% and 15% dilution at 1.5 bar

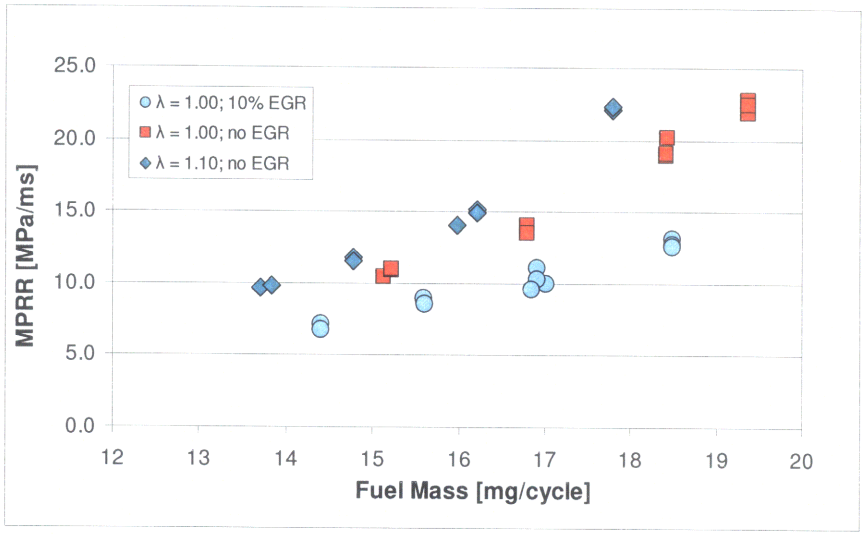

Figure C.1: MPRR versus the fuel mass for several boost levels. All points had stoichiometric fueling, no external EGR and an intake temperature of 120°C. 10% dilution with MAP = 1.5 bar.

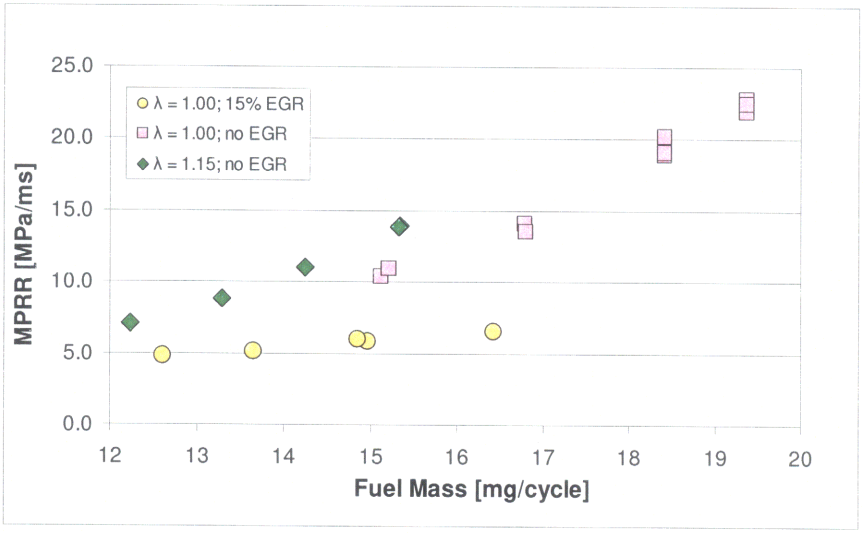

Figure C.2: MPRR versus the fuel mass for several boost levels. All points had stoichiometric fueling, no external EGR and an intake temperature of 120°C. 15% dilution with MAP = 1.5 bar.